ABSTRACT

STAR, ANA M. Numerical Simulation of Injection of Supercritical Ethylene/Methane into Nitrogen (Under the direction of Jack R. Edwards)

The present study investigates the physical mechanisms of supercritical fluid injection for pure ethylene and ethylene/methane mixtures, as well as onset of condensation upon fluid expansion. These mechanisms are considered a key enabling technology in the design of hydrocarbon-fueled scramjet engines. The numerical method combines a solution of the compressible Navier-Stokes equations for the supercritical fluid with two different approaches for condensate growth: one based on a homogeneous equilibrium assumption and the other on classical aerosol dynamics. The thermodynamic behavior of the supercritical fluid is described using the Peng-Robinson equation of state. Computational results are compared with shadowgraph and direct-lighting imaging data, mass flow measurements, mole fraction measurements and temperature measurements in the jet mixing zone, and pressure distributions within a three-dimensional injector geometry. Qualitative results involving jet structure, the appearance of a condensed phase, and the general effects of back pressure and injectant temperature are in good agreement with experimental results for pure ethylene injection. Quantitative results also display reasonable agreement with experimental results but do indicate the need for improving the model. Qualitative trends for ethylene/methane mixture injection are in moderate agreement with the experimental data, suggesting that the thermodynamic interaction between ethylene and methane as modeled by the chosen mixing rules are not sufficiently accurate.

For conditions where both are applicable, a finite-rate (nucleation/growth) phase-transition model presents essentially the same bulk fluid response as a homogeneous equilibrium model with additional predictions of number density and average droplet size.

NUMERICAL SIMULATION OF INJECTION OF SUPERCRITICAL ETHYLENE/METHANE INTO NITROGEN

by

ANA M. STAR

A thesis submitted to the Graduate Faculty of
North Carolina State University
in partial fulfillment of the
requirements for the Degree of
Master of Science

AEROSPACE ENGINEERING

Raleigh, NC

2005

APPROVED BY:

Dr. H. A. Hassan	Dr. R. D. Gould

Dr. J. R. Edwards, Jr. – Chairman

dedicated to: *my husband, Jason Star**,** whose love, joy, and friendship have made me a radiant Star shining brighter everyday. Thank you for sharing your life with me!*

BIOGRAPHY

Ana Maria Star was born in Belo Horizonte, Minas Gerais, Brazil on the 2nd of November 1979 to João Bosco Gamaliel Pinto and Jaimar Da Costa Linares. She grew up in Brazil where she completed Middle School and then moved to the United States with her mom and sister in 1995. While attending Miami Springs Senior High School, Ana joined the math, computer and engineering clubs where she had the opportunity to participate in student competitions and met highly motivated students and teachers who inspired her desire to learn science and engineering. After graduating from high school in 1999, Ana joined North Carolina State University's Engineering program and earned a Bachelor of Science in Aerospace Engineering in 2003. She is currently pursuing a Master of Science Degree in Aerospace Engineering from the same institution, under the direction of Dr. Jack R. Edwards. During her graduate studies, Ana met and married her soul mate Jason Blue Star. After graduation they will be working as engineers in the Naval Surface Warfare Center, Indian Head Division in Maryland.

ACKNOWLEDGEMENTS

It is impossible to accomplish anything alone. There are always a large number of great people who help us achieve our goals. I would like to acknowledge a few of them.

First and foremost, I would like to thank my husband, Jason Star, for all his assistance, incentive, and love which sustained me throughout this journey.

I would like to express my gratitude to my advisor, Dr. Edwards whose guidance, support, intelligence and infinite patience made this all possible. I would also like to thank Dr. H. A. Hassan and Dr. R. D. Gould for serving on my advisory committee, and all my professors at NC State who helped me become a better student.

I am also grateful to my mother who has always sacrificed so much in order to help me make my dreams come true. She instilled in me the importance of education at an early age, and set very high standards for me. *Obrigado Mãezinha do fundo do meu coração.*

Thanks must be given to my dad Julio Linares whose love, hard work and uplifting spirit helped me become who I am today.

I would like to acknowledge Taitech, Inc. and the U.S. Air Force Research Laboratory, propulsion directorate at Wright-Patterson AFB for sponsoring this research (contract number T002-34-01) under a subcontract from Taitech's base contract F33615-02-C-2234 with the U.S Air Force. I appreciate all the help and support of Steven Lin, and Susan Cox-Stouffer from Taitech Inc. I would also like to acknowledge North Carolina State University High Performance Computing Center for supporting my

research by granting access to their computer resources.

Special thanks need to be given to all of my co-workers at the CFD lab who kept me motivated and helped me grow with several arguments and discussions. Ming Tian, and Adam Amar deserve special recognition.

As for my good friend Hussein S. Harb, thanks for your friendship and encouragement during good and tough times in school.

I am also very grateful for momma Star for always holding the light on Jason and me, for helping us so much, and for believing in our success.

Finally, I would like to thank my grandmother Maria Francisca, my sister Marianinha and my beautiful niece Jamie for teaching me so many things and for making life more beautiful.

TABLE OF CONTENTS

LIST OF TABLES

LIST OF FIGURES

LIST OF SYMBOLS

Roman Symbols:

$C^{\pm}$	split Mach number
$C_{p,k}$	specific heat at constant pressure for species k
$D^{\pm}$	pressure splitting function
$\mathbf{E}$, $\mathbf{F}$, $\mathbf{G}$	inviscid flux vector in ξ, η, ζ directions
$\mathbf{E}_{\mathbf{v}}$, $\mathbf{F}_{\mathbf{v}}$, $\mathbf{G}_{\mathbf{v}}$	viscous flux vector in ξ, η, ζ directions
F	condensation rate
F_k	condensation rate for species k
H	total mixture enthalpy per mass
H_k^I	total mixture enthalpy of phase I for species per mass
I	identity matrix, nucleation rate, phase description
I_k	nucleation rate for species k
J	Jacobian of a coordinate transformation
Kn	Knudson number
M	Mach number
M_w	mixture molecular weight
$M_{w,k}$	mixture molecular weight of species k
N	particle number density
N_A	Avogadro's number
NL	number of components in liquid phase
NS	total number of species
NV	number of components in vapor phase
$P_{L,R}^{\pm}$	subsonic pressure splitting function
Pr	laminar Prandtl number
Pr_t	turbulent Prandtl number
$[P_k]$	Parachor of species k
R	universal gas constant

$\mathbf{R}$	residual vector
S	supersaturation ratio
$\mathbf{S}$	source term vector
Sc	Schmidt number
Sc_t	turbulent Schmidt number
T	temperature
T_c	critical temperature
T_r	reduced temperature
$\mathbf{U}$	vector of conserved variables
U_c, V_c, W_c	contravariant velocities components
$U^I_{d,k}, V^I_{d,k}, W^I_{d,k}$	diffusion velocities components of species k in the I phase
V	mixture volume
$\mathbf{V}$	vector of primitive variables
$\forall$	grid cell volume
V_I	volume of phase I
Y_I	volume fraction of phase I
Z	compressibility factor
Z_I	compressibility factor of phase I
a	speed of sound
d	average droplet diameter
f^I	pure component fugacity of phase I
f^I_k	fugacity for component k in the I
g^*	number of molecules in critical nucleus
h	mixture enthalpy per mass
h_I	enthalpy of phase I per mass
h^I_k	enthalpy of phase I for species k per mass
i, j, k	indices corresponding to ξ, η, ζ directions
k	species, turbulence kinetic energy
k_b	Boltzmann's constant
m	total mass
m_I	mass in phase I
m_k	mass of species k
m^I_k	mass of species k in phase I

n	total number of moles, particle size distribution
n_I	number of moles in phase I
n_k	number of moles of species k
n_k^I	number of moles of species k in phase I
p	static pressure
p_c	critical pressure
p_r	reduced pressure
t	time
t_{ij}	laminar viscous stress tensor
u, v, w	Cartesian velocities in the x, y, z directions
u_i	Cartesian coordinate in index notation
u_i^I	Cartesian coordinate in phase I in index notation
$u_{d,k}^I$, $v_{d,k}^I$, $w_{d,k}^I$	Cartesian molecular diffusion velocities for component k in phase I
y_k^I	mass fraction of species k in phase I
x, y, z	Cartesian coordinates
x_i	Cartesian coordinate in index notation
x_k^I	mole fraction of k in phase I

Greek Symbols:

Δ	difference operator
Ω	vorticity vector
α_I	volume fraction of phase I
δ_{ij}	Kronecker delta
ε	turbulent dissipation
λ_{ij}	binary interaction parameter
ν	laminar kinematic viscosity
ν_t	turbulent kinematic viscosity
μ	mixture laminar viscosity
μ_k^I	mixture laminar viscosity
ξ, η, ζ	generalized coordinates
ξ_i	generalized coordinates in index notation

ρ	total mixture density
ρ_I	density of phase I
σ	fluid surface tension coefficient
τ_{ij}	turbulent stress tensor in index notation
ω	specific dissipation rate
ω_k^I	source term for species k in phase I

Subscripts:

$\frac{1}{2}$	represents a numerical interface quantity
∞	represents a freestream quantity, infinity
I	represents fluid phase
l	represents a property in liquid phase
T	represents partial derivative with respect to T
c	represents critical property
o	represents initial condition
r	represents reduced thermodynamic variable
p	represents partial derivative with respect to p
t	represents turbulent property
v	represents a property in vapor phase

Superscripts:

$\pm$	represents positive/negative splitting
I	represents fluid phase
IG	represents property in ideal gas phase
L, R	represents left/right side of cell interface
c	represents convective Contribution
k	represents chemical species
l	represents a property in liquid phase
n	represents time level
v	represents a property in vapor phase

Accents:

‾	represents a Reynolds averaged mean component, represents a per mole quantity
'	represents a Reynolds fluctuation component
~	represents a Favre averaged mean component,
"	represents a Favre fluctuation component

Abbreviations:

BC	Boundary Condition
CFD	Computational Fluid Dynamics
CFL	Courant Friedrichs Levy number
GDE	General Dynamic Equation
ILU	Incomplete Lower Upper factorization method
LDFSS	Low Diffusion Flux Splitting Scheme
MPI	Message Passing Interface
TVD	Total Variation Diminishing
3D	Three-Dimensions
2D	Two-Dimensions

Others:

∇	del operator
∂	partial derivative

1 INTRODUCTION

Processes involving supercritical fluids have been explored for different applications such as fluid extraction and chromatography in the chemical industry and fuel injection in the aerospace industry. U.S Air Force high-speed propulsion systems cannot be cooled by conventional techniques due to the temperature limit of current aerospace materials. Regenerative fuel cooling of the airframe and the combustor components is an option that has been explored [5]. Endothermic fuels can be used for regenerative cooling, since they act as a heat sink, undergoing endothermic thermal cracking reactions at very high temperatures. These temperatures are usually much higher than the critical temperature of hydrocarbon fuels. The cooling system is thus responsible for the phase transition of endothermic fuels from a liquid phase to a supercritical-fluid phase.

A fluid is defined to be in a supercritical state if its temperature and pressure are above the critical value, where the boundary between liquid and vapor disappear (Figure 1.1). The physical properties of a supercritical fluid are counterintuitive for it exhibits characteristics resembling both liquids and gases in the sense that the fluid has a low viscosity and is highly compressible, like a gas, but is relatively dense and can dissolve a wide range of solid compounds, like a liquid.

It is important to understand the injection process involving supercritical fuels as subsequent mixing and chemical reaction will depend on the state of the fuel as it enters the combustor. The injection of fuels at supercritical conditions is thought to be

favorable for promoting rapid mixing and ignition, as it should be most similar to gas-phase injection. However, condensation (the formation of liquid-fuel droplets) due to fluid expansion may occur under certain injection conditions.

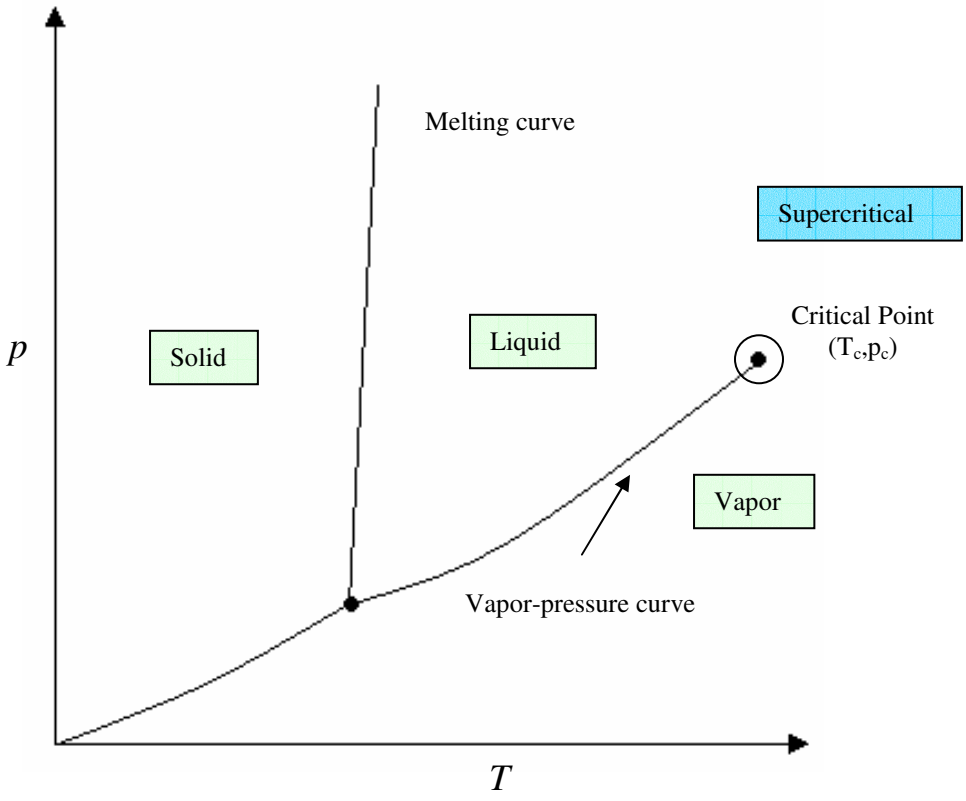

Figure 1.1: Pressure Temperature Phase Diagram

The potential impact of fuel condensation on scramjet combustion is uncertain, and the factors that promote condensate growth should be determined in order to predict its occurrence and to enable its control.

Detailed experimental data on the injection of supercritical ethylene into nitrogen through round-hole (axisymmetric) nozzles were obtained from studies conducted by Wu, et al. [40, 41]. The Wu, et al. database considers parametric variations of the

injectant temperature, chamber temperature, and chamber pressure and presents the effects of these variations on the ethylene jet structure. Under certain conditions, the presence of condensed ethylene liquid phase on the jet structure was indicated by shadowgraph imaging. The onset of this event, most probably driven by homogeneous or heterogeneous nucleation, could not be determined due to difficulties in imaging the internal structure of the round-hole injector used.

Later, Lin, et al. [18] used a transparent, three-dimensional injector configuration with a square exit cross-section to image the onset of condensation. Their numerical model, used to substantiate the experimental results, consists of perfect-gas Navier-Stokes calculations to provide a baseline flowfield for calculating supersaturation and nucleation rates. Onset locations, indicated by a large increase in nucleation rate, were predicted to a reasonable degree, even though supercritical fluid effects were neglected. However, such an approach cannot account for the effects of condensate growth on the flowfield, nor can it give an indication of the amount of condensate present (in terms of a volume or mass fraction).

Lin, et al also considered methane/ethylene mixtures as a more realistic surrogate for cracked JP – class fuels, essentially repeating the Wu, et al. database in the scope of their data collection. More recently, additional data involving pure ethylene injection through round-hole (axisymmetric) nozzles at lower injectant temperatures has been obtained, as have pressure measurements within some of the transparent, three-dimensional nozzles.

The objective of this investigation is to provide insight into the physical

mechanisms of supercritical fluid injection for pure ethylene and ethylene/methane mixtures, as well as the onset of condensation upon fluid expansion.

As an initial step, pure ethylene injection into nitrogen through round-hole axisymmetric-nozzles is investigated using the homogeneous equilibrium assumption. Then, pure ethylene injection through a three-dimensional rectangular nozzle is considered using both the homogeneous equilibrium assumption as well as nucleation/growth theory. Finally, binary mixture (ethylene/methane) injection is investigated using nucleation/growth theory.

In order to solve the different cases outlined above, four different computer codes were used for the computational analysis. The first code, used for the axisymmetric simulations, consists of an implicit method based on incomplete LU decomposition to advance the solution and incorporates the homogeneous equilibrium model as well as gas-phase mixing rules for ethylene injection into nitrogen. The second code solves three-dimensional flows and is a direct extension of the axisymmetric code with the exception that Menter's two-equation turbulence model is used in place of Menter's one-equation model. This code uses a planar relaxation method to advance the solution and is parallelized using MPI for execution on NCSU's Linux Cluster. The third code, used for the three-dimensional calculations with the aerosol transport model, is similar to the second code, but incorporates a "mixture" model of two-phase flow [19]. The Peng-Robinson equation provides both the liquid- and gas-phase state description. Other modifications include a different set of working thermodynamic variables as well as a different two-phase flow model which includes homogeneous/nucleation growth theory.

The fourth code, which solves for the injection of a binary mixture of ethylene and methane, is an extension of the third code applied to a multi-component system.

The present study develops an improved model for the injection process by combining a solution of the Navier-Stokes equations for the supercritical fluid with two different approaches for condensate growth: one based on a homogeneous equilibrium assumption and the other on classical aerosol dynamics extended to supercritical fluids [11, 17]. The following discussion describes the computational model and its solution procedure, presents details of experimental measurements conducted in support of this investigation, and concludes with the model's application in simulating the supercritical ethylene/methane injection experiments of Wu, et al. [40, 41] and Lin, et al. [18].

2 GOVERNING EQUATIONS

2.1 MULTI-COMPONENT-MULTI-PHASE DESCRIPTION

All of the cases considered in this study involve two-phase flows which include vapor and liquid phases. When dealing with two-phase flows it is important to introduce new flow parameters, as well as mixing rules which establish relationships between phasic values and bulk values.

Several cases involving the injection of supercritical multi-component mixture have been investigated in this research. In order to implement a multi-component mixture formulation additional terms and relations must be included. In the following sections, mixing rules and physical relations are introduced for multi-phase, multi-component mixtures.

2.1.1 Volume Fraction

The volume fraction is defined as the volume occupied by a particular phase, referenced to the system's total volume. The vapor volume fraction is given as

$$\alpha_v = \frac{V_v}{V_v + V_l} = \frac{V_v}{V} \tag{2.1.1}$$

where V_v is the volume of the gas phase, V_l is the volume of the liquid phase, and V is the total volume of the system. Similarly, the liquid volume fraction can be written as

$$\alpha_l = \frac{V_l}{V} = \frac{V - V_v}{V} = 1 - \alpha_v \tag{2.1.2}$$

2.1.2 Phasic Mass Fraction and Mole Fraction

The vapor mass fraction, Y_v is the ratio of the mass of the vapor phase to the total mass of the system, given as follows

$$Y_v = \frac{m_v}{m} = \frac{\rho_v V_v}{\rho V} = \frac{\rho_v \alpha_v}{\rho_v \alpha_v + \rho_l \alpha_l} \tag{2.1.3}$$

where m_v is the mass of the vapor phase, and m is the total mass of the system. In the same manner, the mass fraction of the liquid phase can be written as

$$Y_l = \frac{m_l}{m} = \frac{\rho_l V_l}{\rho V} = \frac{\rho_l \alpha_l}{\rho_v \alpha_v + \rho_l \alpha_l} = 1 - Y_v \tag{2.1.4}$$

where m_l is the mass of the liquid phase.

2.1.3 Phasic Mixture Properties

The bulk density of the two-phase mixture is defined using Amagat's law:

$$\frac{1}{\rho} = \frac{Y_v}{\rho_v(p,T)} + \frac{1 - Y_v}{\rho_l(p,T)} \tag{2.1.5}$$

where Y_v is the vapor mass fraction and ρ_v and ρ_l are the vapor phase and liquid phase densities, respectively.

The mixture enthalpy is defined as a mass-fraction weighted average of the vapor phase enthalpy and the liquid phase enthalpy:

$$\rho h = \rho_v \alpha_v h_v(p,T) + \rho_l \alpha_l h_l(p,T) \tag{2.1.6}$$

or

$$h = Y_v h_v(p,T) + Y_l h_l(p,T) \tag{2.1.7}$$

Similarly, the mixture velocity is given as

$$u_i = Y_v u_i^v + Y_l u_i^v \tag{2.1.8}$$

where u_i^v is the velocity of gas phase and u_i^l is the velocity of liquid phase in index notation. If $u_i^v = u_i^l = u_i$ then the system is in kinematic equilibrium. Kinematic equilibrium is assumed for all cases considered in this study.

2.1.4 Multi-Component Mass Fraction and Mole Fraction

The multi-component formulation requires the specification of a species mass fraction which is defined as

$$Y_k = \frac{m_k}{\sum_{k=1}^{NS} m_k} \tag{2.1.9}$$

where m_k is the species mass within the system. However, the computation of thermodynamic properties and derivatives are calculated on a phasic basis in which the species phasic mass and mole fractions are necessary. The mass fraction of species k relative to the total vapor mass m_v and the mole fraction of species k relative to the total number of moles within the vapor phase n_v are given correspondingly

$$y_k^v = \frac{m_k^v}{m_v}, \; x_k^v = \frac{n_k^v}{n_v} \tag{2.1.10}$$

Similarly the mass fraction of species k, relative to the total liquid mass m_l and the mole fraction of species k, relative to the total number of moles within the liquid phase n_l are expressed as

$$y_k^l = \frac{m_k^l}{m_l}, \; x_k^l = \frac{n_k^l}{n_l} \tag{2.1.11}$$

where m_k^I, and n_k^I are the species mass and number of moles for a given phase ($I = v$ or $I = l$) respectively.

Additional relations are obtained from the fact that all mass and mole fractions within a phase should add to unity

$$\sum_{k=1}^{NV} y_k^v = \sum_{k=1}^{NL} y_k^l = 1 \tag{2.1.12}$$

$$\sum_{k=1}^{NV} x_k^v = \sum_{k=1}^{NL} x_k^l = 1 \tag{2.1.13}$$

Therefore for a binary mixture the above constraints are reduced to

$$y_2^I = 1 - y_1^I \tag{2.1.14}$$

$$x_2^I = 1 - x_1^I \tag{2.1.15}$$

when applying mass conservation to the non-reacting, two-phase, multi-component system the following expression is obtained:

$$Y_v y_k^v + (1 - Y_v) y_k^l = Y_{k,o} \tag{2.1.16}$$

where Y_v is the ratio of the mass of the vapor phase to the total mass in the system.

2.2 NAVIER-STOKES EQUATIONS

The Navier-Stokes equations are assumed to govern the dynamics of compressible, multi-phase, multi-component fluids. This set of equations is based on the independent dynamical laws in continuum mechanics: continuity equation, the momentum equation and the energy equation. These three equations are the mathematical statements of three fundamental physical principles respectively:

1. Mass is conserved.
2. Momentum is conserved (Newton's second Law, $\mathbf{F} = m\mathbf{a}$).
3. Energy is conserved.

The non-chemically reacting, compressible Navier-Stokes equations, written in strong conservation law, vector form for Cartesian coordinates are:

$$\frac{\partial \mathbf{U}}{\partial t} + \frac{\partial (\mathbf{E} - \mathbf{E}_\mathbf{v})}{\partial x} + \frac{\partial (\mathbf{F} - \mathbf{F}_\mathbf{v})}{\partial y} + \frac{\partial (\mathbf{G} - \mathbf{G}_\mathbf{v})}{\partial z} = \mathbf{S} \tag{2.2.1}$$

where $\mathbf{U}$ is the vector of conservative variables, $\mathbf{E}$, $\mathbf{F}$ and $\mathbf{G}$ are the inviscid fluxes, $\mathbf{E}_\mathbf{v}$, $\mathbf{F}_\mathbf{v}$ and $\mathbf{G}_\mathbf{v}$ are the viscous fluxes, and $\mathbf{S}$ is the vector source terms, expressed separately as

$$\mathbf{U}=\begin{bmatrix}\rho Y_v y_1^v\\ \vdots\\ \rho Y_v y_{NV-1}^v\\ \rho Y_l y_1^l\\ \vdots\\ \rho Y_l y_{NL-1}^l\\ \rho Y_v\\ \rho\\ \rho u\\ \rho v\\ \rho w\\ \rho H-p\end{bmatrix},\ \mathbf{E}=\begin{bmatrix}\rho Y_v y_1^v u\\ \vdots\\ \rho Y_v y_{NV-1}^v u\\ \rho Y_l y_1^l u\\ \vdots\\ \rho Y_l y_{NL-1}^l u\\ \rho Y_v u\\ \rho u\\ \rho u^2+p\\ \rho vu\\ \rho wu\\ \rho Hu\end{bmatrix},\ \mathbf{F}=\begin{bmatrix}\rho Y_v y_1^v v\\ \vdots\\ \rho Y_v y_{NV-1}^v v\\ \rho Y_l y_1^l v\\ \vdots\\ \rho Y_l y_{NL-1}^l v\\ \rho Y_v v\\ \rho v\\ \rho uv\\ \rho v^2+p\\ \rho wv\\ \rho Hv\end{bmatrix},\ \mathbf{G}=\begin{bmatrix}\rho Y_v y_1^v w\\ \vdots\\ \rho Y_v y_{NV-1}^v w\\ \rho Y_l y_1^l w\\ \vdots\\ \rho Y_l y_{NL-1}^l w\\ \rho Y_v w\\ \rho w\\ \rho uw\\ \rho vw\\ \rho w^2+p\\ \rho Hw\end{bmatrix} \qquad \textbf{(2.2.2)}$$

$$\mathbf{E_v}=\begin{bmatrix}-\rho Y_v y_1^v u_{d,1}^v\\ \vdots\\ -\rho Y_v y_{NV-1}^v u_{d,NV-1}^v\\ -\rho Y_l y_1^l u_{d,1}^l\\ \vdots\\ -\rho Y_l y_{NL-1}^l u_{d,NL-1}^l\\ -\rho Y_v \sum_{k=1}^{NV} y_k^v u_{d,k}^v\\ 0\\ t_{xx}\\ t_{yx}\\ t_{zx}\\ -\rho\left(Y_v\sum_{k=1}^{NV} y_k^v H_k^v u_{d,k}^v + Y_l\sum_{k=1}^{NL} y_k^l H_k^l u_{d,k}^l\right)+u_i t_{ix}-q_x\end{bmatrix} \qquad \textbf{(2.2.3)}$$

$$\mathbf{F_v} = \begin{bmatrix} -\rho Y_v y_1^v v_{d,1}^v \\ \vdots \\ -\rho Y_v y_{NV-1}^v v_{d,NV-1}^v \\ -\rho Y_l y_1^l v_{d,1}^l \\ \vdots \\ -\rho Y_l y_{NL-1}^l v_{d,NL-1}^l \\ -\rho Y_v \sum_{k=1}^{NV} y_k^v v_{d,k}^v \\ 0 \\ t_{xy} \\ t_{yy} \\ t_{zy} \\ -\rho\left(Y_v \sum_{k=1}^{NV} y_k^v H_k^v v_{d,k}^v + Y_l \sum_{k=1}^{NL} y_k^l H_k^l v_{d,k}^l \right) + u_i t_{iy} - q_y \end{bmatrix} \tag{2.2.4}$$

$$\mathbf{G_v} = \begin{bmatrix} -\rho Y_v y_1^v w_{d,1}^v \\ \vdots \\ -\rho Y_v y_{NV-1}^v w_{d,NV-1}^v \\ -\rho Y_l y_1^l w_{d,1}^l \\ \vdots \\ -\rho Y_l y_{NL-1}^l w_{d,NL-1}^l \\ -\rho Y_v \sum_{k=1}^{NV} y_k^v w_{d,k}^v \\ 0 \\ t_{xz} \\ t_{yz} \\ t_{zz} \\ -\rho\left(Y_v \sum_{k=1}^{NV} y_k^v H_k^v w_{d,k}^v + Y_l \sum_{k=1}^{NL} y_k^l H_k^l w_{d,k}^l \right) + u_i t_{iz} - q_z \end{bmatrix}, \mathbf{S} = \begin{bmatrix} \omega_1^v \\ \vdots \\ \omega_{NV-1}^v \\ \omega_1^l \\ \vdots \\ \omega_{NL-1}^l \\ \sum_{k=1}^{NV} \omega_k^v \\ 0 \\ 0 \\ 0 \\ 0 \\ 0 \end{bmatrix} \tag{2.2.5}$$

where $u_{d,k}^{v,l}$, $v_{d,k}^{v,l}$, $w_{d,k}^{v,l}$ are diffusion velocities for the vapor or liquid phases of species k are derived in Appendix A. The number of species in the vapor phase and liquid phase are denoted by NV and NL respectively.

2.3 SYSTEM CLOSURE: EQUATIONS OF STATE

Closure of the Navier-Stokes equations is achieved by an equation of state defining the thermodynamic state description of the fluid having the form of $p = p\left(\rho, T, x_1^v, ..., x_{NV-1,}^v x_1^l, ..., x_{NL-1,}^l\right)$ and $h = h\left(\rho, T, y_1^v, ..., y_{NV-1,}^v y_1^l, ..., y_{NL-1,}^l\right)$. This investigation implements the ideal-gas equation of state as well as the Peng-Robinson equation of state.

2.3.1 Ideal Gas Relation

Some of the cases considered in this study involve the injection of ethylene, initially at supercritical conditions, into a chamber containing pure gaseous nitrogen. For such cases, the relation between pressure, temperature and density of nitrogen are obtained from the ideal gas state equation, given as follows:

$$p = \underline{\rho} RT \tag{2.3.1}$$

where $\underline{\rho}$ is the molar density ρ / M_w, M_w is the molecular weight, and R is the universal gas constant.

The ideal gas description for enthalpy and specific heat at constant pressure are given by the following polynomial curve-fit

$$h_{IG,k}(T) = \frac{R}{M_{w,k}}\left(a_{1,k}T + \frac{1}{2}a_{2,k}T^2 + \frac{1}{3}a_{3,k}T^3 + \frac{1}{4}a_{4,k}T^4 + \frac{1}{5}a_{5,k}T^5 + b_{1,k} \right) \quad \textbf{(2.3.2)}$$

$$C_{p,IG,k}(T) = \frac{R}{M_{w,k}}\left(a_{1,k} + a_{2,k}T + a_{3,k}T^2 + a_{4,k}T^3 + a_{5,k}T^4 \right) \quad \textbf{(2.3.3)}$$

where coefficients $a_{1,k},...,a_{5,k}$ and $b_{1,k}$, for species k, are obtained from McBride, et al. [23].

2.3.2 Peng-Robinson Equation of State

To account for the thermodynamic behavior of the supercritical fluid, it is necessary to utilize a generalized state equation, defined by the relations $p = p(\rho, T)$ and $h = h(\rho, T)$. In this study, the Peng-Robinson equation of state [27] is used for its simplicity and accuracy when predicting $p - \underline{\rho} - T$ behavior in both the vapor and liquid regions for hydrocarbons. This equation of state is one of the most commonly used cubic equations of state, having a similar formulation to the Van der Waals equation. The Peng-Robinson equation of state for a single-component fluid is given by

$$p = Z(\underline{\rho}, T)\underline{\rho}RT \quad \textbf{(2.3.4)}$$

$$Z(\underline{\rho}, T) = \frac{1}{1 - b\underline{\rho}} - \frac{a(T)}{RT}\frac{\underline{\rho}}{\left(1 + 2b\underline{\rho} - (b\underline{\rho})^2\right)} \quad \textbf{(2.3.5)}$$

where $\underline{\rho}$ is the molar density ρ / M_w, M_w is the molecular weight, and R is the universal gas constant. In this, the function $a(T)$ is defined as

$$a(T) = a(T_c)\alpha(T_r, \omega) \tag{2.3.6}$$

with

$$a(T_c) = 0.45724 \frac{R^2 T_c^2}{P_c} \tag{2.3.7}$$

$$\alpha^{1/2}(T_r, \omega) = 1 + \kappa\left(1 - T_r^{1/2}\right) \tag{2.3.8}$$

$$\kappa = 0.37464 + 1.54226\omega - 0.26992\omega^2 \tag{2.3.9}$$

$$T_r = \frac{T}{T_c} \tag{2.3.10}$$

The constant b is defined as

$$b = 0.07780 \frac{RT_c}{p_c} \tag{2.3.11}$$

and other functions used in subsequent developments are as follows:

$$A = \frac{a(T)p}{R^2 T^2} \tag{2.3.12}$$

$$B = \frac{bp}{RT} \tag{2.3.13}$$

These parameters are functions of the critical-point temperature T_c and pressure p_c of the fluid and its acentric factor ω. The following values are used for ethylene and methane:

Table 2.1: Ethylene and Methane Parameters

Species	T_c (K)	p_c (Mpa)	ω
ethylene (C_2H_4)	282.350	5.0418	0.077523
methane (CH_4)	190.564	4.5992	0.011420

The enthalpy of a real fluid can be written as the sum of an ideal gas enthalpy and a departure function as follows:

$$h(\rho,T) = h_{IG}(T) + \frac{1}{M_w}\left[RT(Z-1) + \int_{\infty}^{v}\left[T\left(\frac{\partial p}{\partial T}\right)_v - p \right] dv \right] \qquad \textbf{(2.3.14)}$$

For the Peng-Robinson EOS the following enthalpy equation is obtained,

$$h(\rho,T) = h_{IG}(T) + \frac{1}{M_w}\left[RT(Z-1) + \frac{T\dfrac{da(T)}{dT} - a(T)}{2\sqrt{2}b} \ln\left(\frac{Z + \left(1+\sqrt{2}\right)B}{Z + \left(1-\sqrt{2}\right)B} \right) \right] \qquad \textbf{(2.3.15)}$$

where $h_{IG}(T)$ is the ideal gas description discussed previously.

2.4 TWO-PHASE FLOWS

All of the cases considered in this study involve two-phase flows which include vapor and liquid phases. Even though the injectant fluid is initially at a supercritical state, gas-phase mixing rules are assumed to apply at this fluid phase. This assumption is adequate as the supercritical fluid expands to gaseous densities upon passing through the nozzle. The different phase regions of interest in this research are illustrated in Figure 2.1 where the pressure-density coexistence curve for pure ethylene defines the boundary

between single phase regions and the two-phase region.

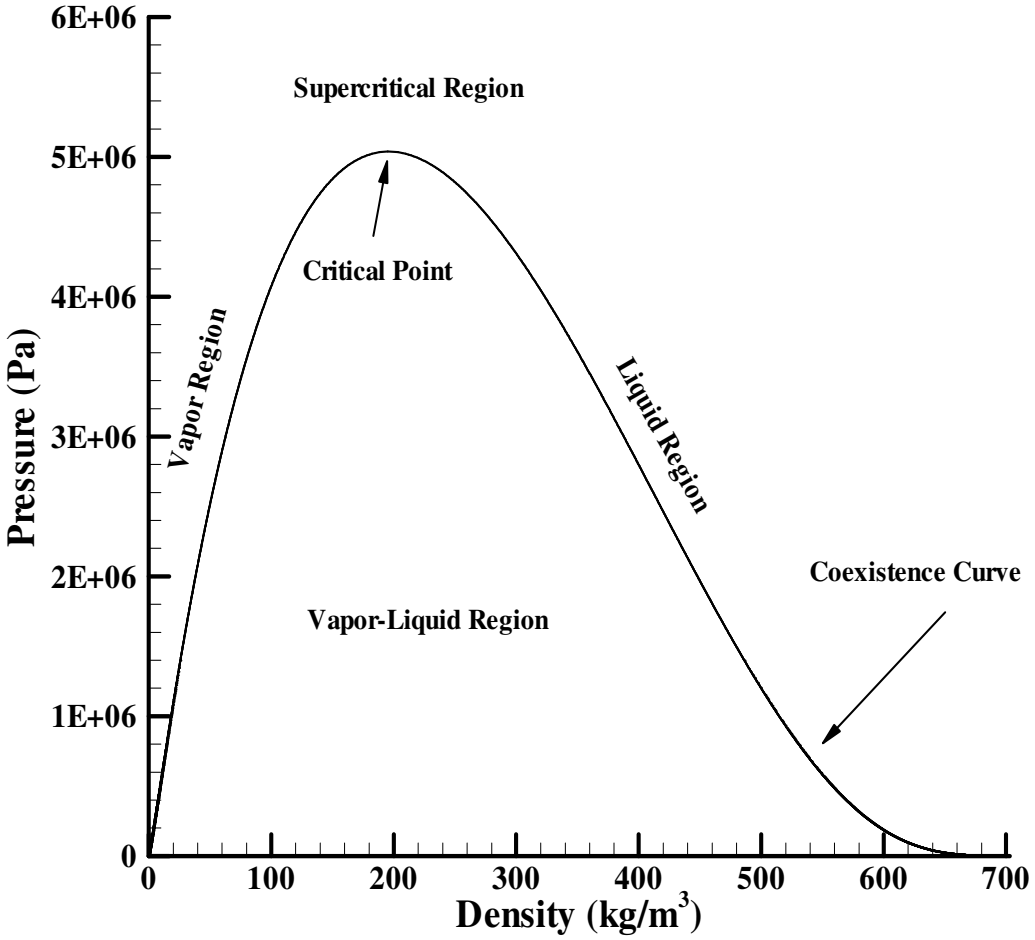

Figure 2.1: Ethylene Coexistence Curve

2.4.1 Phase Equilibria

To better understand phase transition it is important to explain how the state description of the fluid behaves for different thermodynamic conditions. Figure 2.2 indicates the shape of various isotherms for a typical cubic equation of state (the Peng-Robinson equation of state is used for this illustration). The isotherm T_1 corresponds to

the supercritical isotherm, where the equation of state description is valid throughout its extent for it satisfies the criterion for fluid stability which requires that $\left(\partial p / \partial \underline{\rho}\right) > 0$. The isotherm T_2, identified as the critical isotherm, has a single point for which $\left(\partial p / \partial \underline{\rho}\right) = 0$; and all other points satisfy the condition $\left(\partial p / \partial \underline{\rho}\right) > 0$. Therefore the critical isotherm is also valid at all locations. The subcritical isotherm T_3 is invalid for density values between spinodal densities located inside the coexistence region where $\left(\partial p / \partial \underline{\rho}\right) < 0$, but satisfies the stability condition everywhere else. The loci of these density values for temperatures between the triple and critical points define liquid and vapor spinodal curves, dividing the two-phase region into metastable vapor, unstable, and metastable liquid regions clearly illustrated in Figure 2.3.

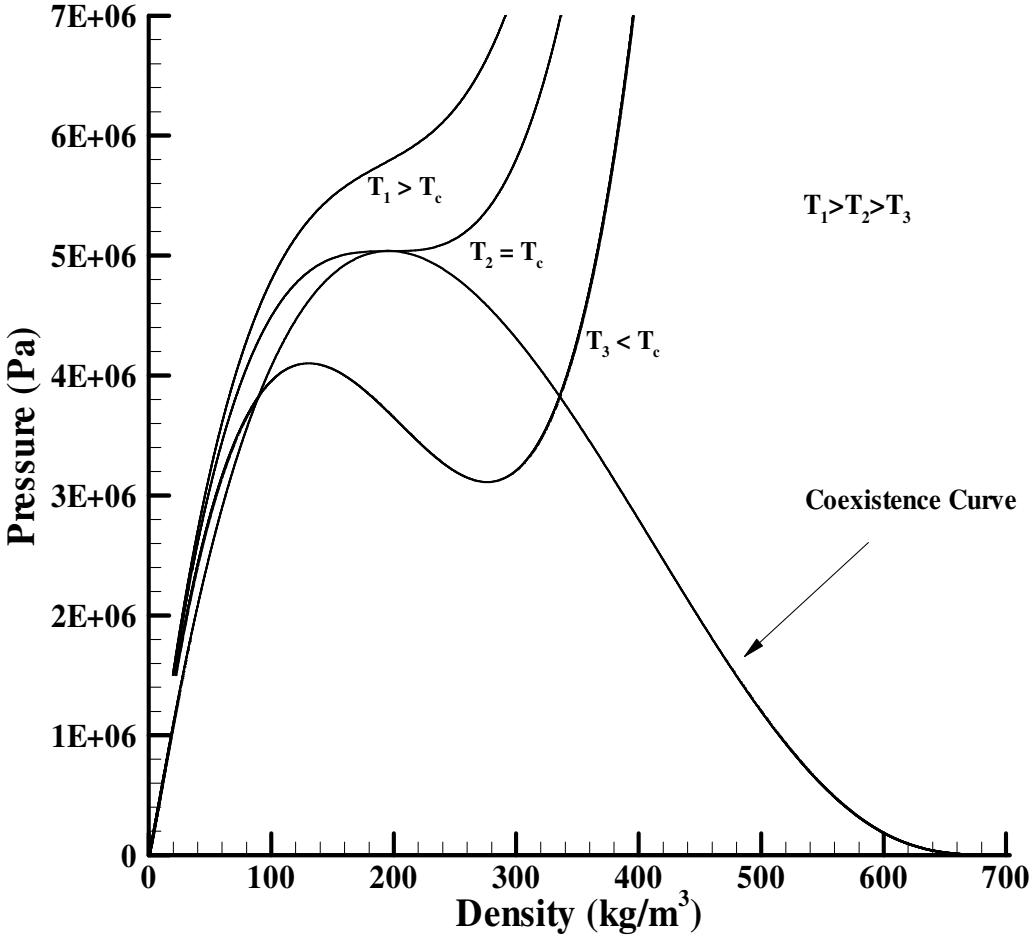

Figure 2.2: Ethylene Isotherms for Peng-Robinson EOS

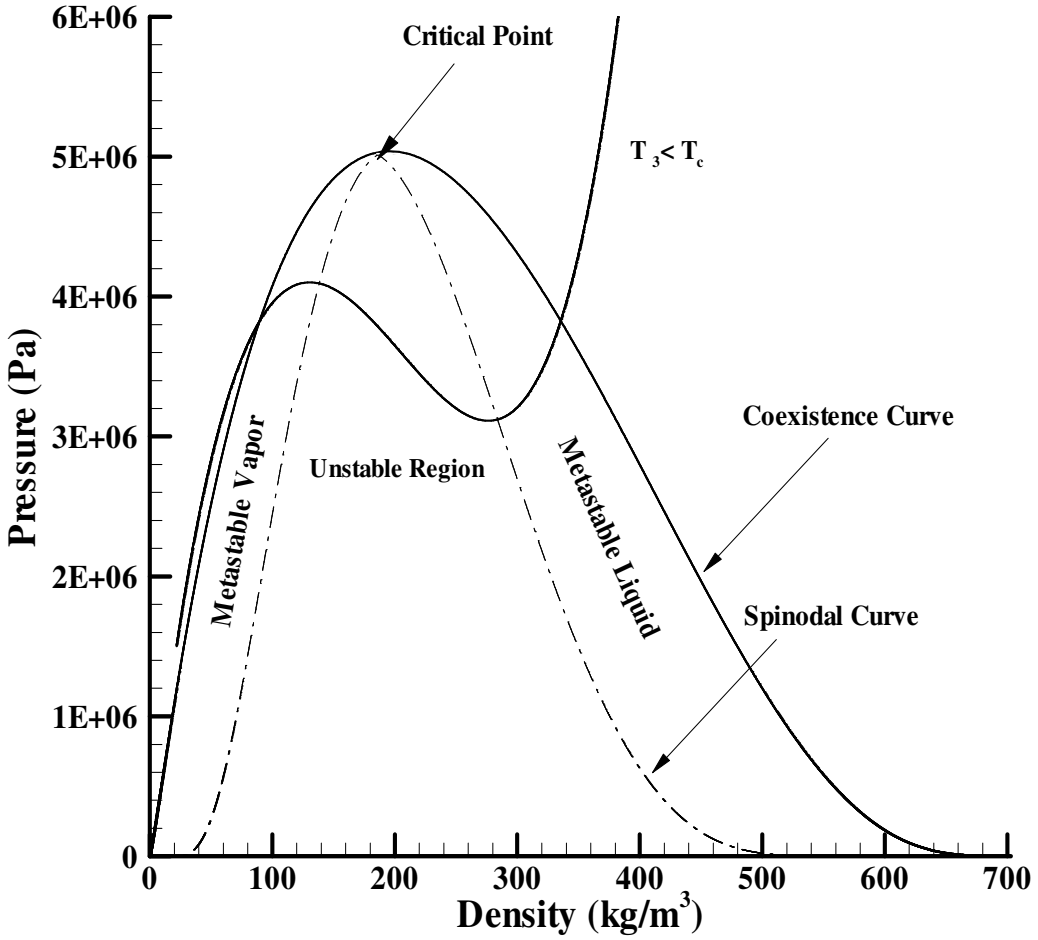

Figure 2.3: Subcritical Isotherm for Ethylene

Figure 2.4 displays a more detailed description of the subcritical isotherm T_3. Clearly indicated is the vapor regime, where pressure varies nearly linearly with density, and the liquid regime, where large pressure changes are required to induce a density change. For a given pressure and temperature, the solution to the Peng-Robinson equation of state returns one or three values of the compressibility factor *Z*, the former corresponding to the single-phase region (supercritical, liquid or vapor) and the latter corresponding to the two-phase region, where vapor and liquid may co-exist. The

corresponding densities for a pressure within the two-phase region are shown as points A-C. A and C represent saturated vapor and liquid states, while B is physically meaningless since it violates the criterion for fluid stability which requires that $(\partial p / \partial \underline{\rho}) > 0$. For a particular temperature, the "allowable" two-phase region is bounded by the pressure values at D and E, which are local extrema. At a particular pressure between the liquid and vapor spinodal points, the system is in equilibrium (for conditions $T_v = T_l$ and $p_v = p_l$), with the vapor and liquid Gibbs free energy values being equal $(\underline{G}_v = \underline{G}_l)$. This pressure is known as the vapor pressure p_{vap} and is calculated as a function of temperature by iteratively solving the equation

$$f_v(Z_v, T, p_{vap}) = f_l(Z_l, T, p_{vap}) \qquad \textbf{(2.4.1)}$$

where the fugacity f is a function of the Gibbs free energy ($\underline{G}_v = \underline{G}_l \Rightarrow f_v = f_l$)

$$\ln \frac{f}{p} = \frac{\underline{G}(T,p) - \underline{G}^{IG}(T,p)}{RT} = \frac{1}{RT} \int_0^p \left(\frac{1}{\underline{\rho}} - \frac{RT}{p} \right) dp \qquad \textbf{(2.4.2)}$$

Using the Peng-Robinson equation of state, the following fugacity relation is obtained

$$\ln \frac{f}{p} = Z - 1 - \ln(Z - B) - \frac{A}{2\sqrt{2}B} \ln \left(\frac{Z + (1+\sqrt{2})B}{Z + (1-\sqrt{2})B} \right) \qquad \textbf{(2.4.3)}$$

The spinodal pressure and density values (point D and E in Figure 2.4) can be obtained analytically by solving the quartic equation $\left. \frac{\partial p}{\partial \underline{\rho}} \right|_T = 0$, discarding two meaningless roots that occur outside the range of validity of the Peng-Robinson equation.

The spinodal pressure values bound the actual vapor pressure, and an appropriate linear combination can be used as an initial guess for the iteration described above.

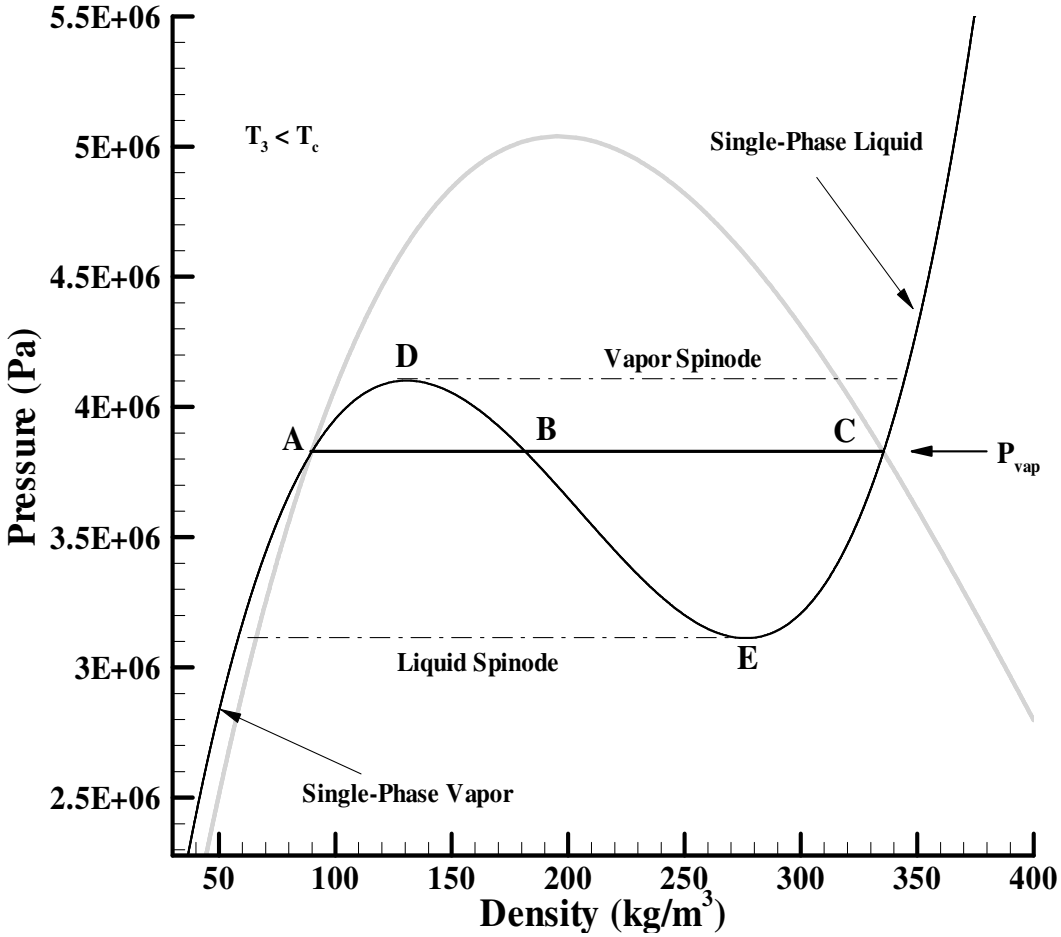

Figure 2.4: Detailed Subcritical Isotherm for Ethylene

2.4.2 Mixture properties

When dealing with two-phase flows it is important to introduce new mixing rules which enable the establishment of relationships between phasic values and bulk values.

In addition to mixing properties for density and enthalpy, other mixture properties

are of interest in this study such as mixture viscosity and thermal conductivity. The two-phase flow mixture viscosity and thermal conductivity are respectively defined as:

$$\mu = \alpha_v \mu_v + \alpha_l \mu_l \tag{2.4.4}$$

$$k = \alpha_v k_v + \alpha_l k_l \tag{2.4.5}$$

The gas mixture molecular viscosity is determined by Wilke's mixing rule [28], and the thermal conductivity is calculated using Wassijewa's equation with Mason and Saxena's modification [28] defined respectively as follows:

$$\mu_v = \sum_{k=1}^{NV} \frac{x_k^v \mu_k^v}{\sum_{l=1}^{NV} x_k^v \phi_{k,l}} \tag{2.4.6}$$

$$k_v = \sum_{k=1}^{NV} \frac{x_k^v k_k^v}{\sum_{j=1}^{NV} x_k^v 1.065 \phi_{k,l}} \tag{2.4.7}$$

where

$$\phi_{k,l} = \frac{\left[1 + \left(\frac{\mu_k^v}{\mu_l^v}\right)^{\frac{1}{2}} \left(\frac{M_{w,k}^v}{M_{w,l}^v}\right)^{\frac{1}{4}}\right]}{\sqrt{8}\left(1 + \frac{M_{w,k}^v}{M_{w,l}^v}\right)^{\frac{1}{2}}} \tag{2.4.8}$$

The liquid mixture molecular viscosity and thermal conductivity are assumed to be equal to pure ethylene values for simplicity. The species viscosities and thermal conductivities were calculated using different methods outlined in Table 2.2.

Table 2.2: Methods for Calculating Species Viscosities and Thermal Conductivities

Species	$\mu_k^v,\ \mu_k^l$	$k_k^v,\ k_k^l$
ethylene (C_2H_4)	Holland, et al.[16]	Holland, et al.[16]
methane (CH_4)	McBride, et al [23], N/A	McBride, et al [23], N/A
nitrogen (N_2)	Sutherland's Formula $\mu_{N_2}^v = 0.1663\left(\frac{T}{273.1}\right)^{\frac{2}{3}}\frac{273.1+106.7}{T+106.7}$, N/A	Prandtl Number $k_{N_2}^v = \frac{C_p^v \mu_{N_2}^v}{\mathrm{Pr}}$, N/A

The mixture sound speed, derived in Appendix B, is expressed as

$$a^2 = \frac{\rho h_T}{\rho\rho_p h_T - \rho\rho_T h_p + \rho_T} \tag{2.4.9}$$

where the thermodynamic derivatives of ρ_p, ρ_T, h_p, and h_T are obtained by differentiating Eqs. (2.6.8 and 2.6.10) with respect to p and T, and are given as

$$\rho_p = \rho^2\left(\frac{Y_v}{\rho_v^2}\frac{\partial\rho_v}{\partial p} + \frac{Y_l}{\rho_l^2}\frac{\partial\rho_l}{\partial p}\right) \tag{2.4.10}$$

$$\rho_T = \rho^2\left(\frac{Y_v}{\rho_v^2}\frac{\partial\rho_v}{\partial T} + \frac{Y_l}{\rho_l^2}\frac{\partial\rho_l}{\partial T}\right) \tag{2.4.11}$$

$$h_p = Y_v\frac{\partial h_v}{\partial p} + Y_l\frac{\partial h_l}{\partial p} \tag{2.4.12}$$

$$h_T = Y_v\frac{\partial h_v}{\partial T} + Y_l\frac{\partial h_l}{\partial T} \tag{2.4.13}$$

The partial derivatives, such as $\frac{\partial\rho_{v,l}}{\partial p}, \frac{\partial\rho_{v,l}}{\partial T}, \frac{\partial h_{v,l}}{\partial p}$ and $\frac{\partial h_{v,l}}{\partial T}$ are derived using the Peng-

Robinson equation of state.

The Peng-Robinson equation of state (like all cubic equations of state) gives no useful information in the unstable part of the two-phase region. For densities between spinodal values, it can be shown that the acoustic eigenvalues are complex, implying that the Euler system is not hyperbolic in time and that conventional time-marching procedures for integrating the equation are ill posed. In order to circumvent this problem two different approaches are used in this study: one is known as the homogeneous equilibrium two-phase model and the other is a model based on aerosol transport theory.

2.4.3 Phase Transition Models: Homogeneous Equilibrium Model

The homogeneous equilibrium two-phase model replaces the equation of state description of the two-phase flow by isobars (horizontal lines), ensuring that the equilibrium phases have the same temperature and pressure (Figure 2.4). The specific location of the isobars is determined by the assumption of thermodynamic equilibrium between the vapor and liquid phases where $\underline{G}_v = \underline{G}_l$.

Once density and temperature values are computed from the time-integration scheme, the following procedure is implemented:

1. For a given temperature, vapor pressure is either calculated by iteratively solving Eqn. (2.6.1) or obtained from a two-phase coexistence curve. The saturation densities $\rho_l(T)$ and $\rho_v(T)$ and the saturation enthalpies $h_l(T)$ and $h_v(T)$ are then determined directly from the equation of state Eqs. (2.6.8) and (2.6.10).

2. If the density is not between the saturation density values or if the temperature

is greater than the critical temperature, then the single-phase description given by the Peng-Robinson equation is used to calculate pressure and enthalpy.

3. If the fluid density is within the saturation limits and the temperature is below its critical value, the equation of state is replaced by the homogeneous equilibrium model given by

$$p = p_{sat}(T)$$

$$\Downarrow$$

$$\alpha_v(\rho,T) = \frac{\rho - \rho_l(T)}{\rho_v(T) - \rho_l(T)}$$

$$\Downarrow$$

$$\alpha_l(\rho,T) = 1 - \alpha_v(\rho,T)$$

$$\Downarrow$$

$$\rho h(\rho,T) = \rho_v(T)\alpha_v(\rho,T)h_v(\rho_v,T) + \rho_l(T)\alpha_l(\rho,T)h_l(\rho_l,T)$$

where the saturation-state enthalpies can be calculated directly from Eq. (2.5.14).

In this formulation, the saturation-state values are strict functions of temperature; density dependence is introduced through the volume fractions $\alpha_{v,l}$ and latent-heat effects arise through the change in departure enthalpy between the saturation states. The above description neglects velocity-slip effects, with the velocity actually solved for being a mass-weighted average velocity, and thermal equilibrium is assumed. This system is hyperbolic in character and is similar to the Euler system in structure but admits such multiphase features as cavitation zones and condensation shocks [6]. Since pressure and temperature are not independent variables in the equilibrium closure for the two-

phase region, density and temperature must be used as the "working" thermodynamic variables (i.e. the values solved for directly in the CFD code). This formulation applied to a single component, two-phase mixture allows a simplification of the Navier-Stokes equations where species and phasic mass conservation equations are eliminated from the system of equations. Therefore instead of solving $NV + NL + 4 = 7$ conservation equations, this method reduces the system to 5 conservation equations (mass=1, momentum=3, energy=1).

2.4.4 Phase Transition Models: Aerosol Transport Theory

The homogeneous equilibrium model is used due to its simplicity and accuracy in evaluating flow properties in the two-phase region. However, it does not provide quantities such as droplet (or bubble) number density, nucleation rate, and average droplet (or bubble) size. Aerosol transport modeling can be used when those additional parameters are of interest, due to its ability to simulate the physical mechanisms involved in a vapor-to-liquid phase transition.

Gas-phase processes, either physical or chemical, can produce a supersaturated state which then disintegrates by aerosol formation. Physical processes generating supersaturation include adiabatic expansion and mixing with cool air, among others.

Once condensable species has been formed in the gas phase, the system is in a nonequilibrium state. The system may attain equilibrium by generation of new particles (homogeneous nucleation) or by condensation on existing particles (droplets) [13]. Homogeneous nucleation is the process by which condensation nuclei are generated by the vapor, while heterogeneous condensation takes place on existing particles without

formation of new nuclei, when high concentrations of particles (droplets) are present at low supersaturation.

The mechanism of aerosol formation by gas-to-particle conversion and all processes influencing the distribution of aerosol properties (aerosol transport) with respect to particle size are assumed to be modeled by the general dynamic equation (GDE), which allows for the solution of a droplet size distribution function $n(\mathbf{v},\mathbf{r},t)$. The droplet size distribution function $n(\mathbf{v},\mathbf{r},t)$ consists of three spatial dimensions, one dimension representing the spectrum of droplet diameters and one temporal dimension.

$$\frac{\partial n}{\partial t} + \nabla \cdot (n\mathbf{v}) = \nabla \cdot D\nabla n + \left[\frac{\partial n}{\partial t}\right]_{growth} + \left[\frac{\partial n}{\partial t}\right]_{coag} - \nabla \cdot \mathbf{c}n \qquad \textbf{(2.4.14)}$$

The left-hand side of the GDE is comprised of terms modeling temporal and advective effects upon the droplet size distribution function. The right-hand side consists of terms representing diffusional growth, gas-to-particle conversion, coagulation, and sedimentation effects, respectively.

In order to simplify the formulation for the GDE, a locally monodisperse droplet size distribution (which yields an average droplet size, rather than a size distribution) is assumed and sedimentation effects are neglected. Two moments of the GDE are of interest in this study: the droplet number density and the vapor-phase mass fraction.

The total droplet number density for a single component is given as follows:

$$\frac{\partial N}{\partial t}+\frac{\partial\left(Nu_j\right)}{\partial x_j}=I+\left.\frac{\partial N}{\partial t}\right|_{coag} \tag{2.4.15}$$

The nucleation rate I is defined as [11, 17]:

$$I=\sqrt{\frac{2\sigma}{\pi}}\frac{pM_w}{RT}\frac{\rho_v\alpha_v}{\rho_l m_e^{3/2}}\exp\left(-\frac{16\pi}{3}\frac{\sigma^3\left(v_e^l\right)^2}{\left(k_bT\right)^3}\left(\frac{1}{\ln\left(S\right)}\right)^2\right) \tag{2.4.16}$$

where $m_e=\frac{M_w}{N_A}$ is the ethylene molecular mass and $v_e^l=\frac{m_e}{\rho_l}$ is the liquid ethylene molecular volume. The interfacial tension σ is curve-fitted for ethylene as follows [14]:

$$\sigma=\max\left(0.001,0.001\times 23.23\left(\frac{T_c-T}{T_c-133.2}\right)^{11/9}\right) \tag{2.4.17}$$

The limiting value of 0.001 is chosen to avoid extremely high nucleation rates near the critical point. The supersaturation S is usually defined as $S=p/p_{vap}$, however, since real-fluid effects are significant S is redefined in terms of the ratio of the vapor-phase fugacity f_v to the saturation value $f_{v,eq}$:

$$S=\frac{f_v}{f_{v,eq}} \tag{2.4.18}$$

The coagulation rate $\left.\frac{\partial N}{\partial t}\right|_{coag}$ may be affected by Brownian motion, mean shear, and Kolmogorov-scale turbulence, among other factors [12]. A comparative study of the relative effects of the different coagulation mechanisms for a similar problem involving rapid expansion of supercritical carbon dioxide solutions through a nozzle was conducted

in Ref. [11]. This study concluded that the largest contribution to the coagulation rate is due to Kolmogorov-scale turbulence, which increases the collision frequency of the droplets. The following coagulation rate model of Saffman and Turner [30] for a locally monodisperse collection of droplets is used in this study:

$$\left.\frac{\partial N}{\partial t}\right|_{coag} = \left.\frac{\partial N}{\partial t}\right|_{turb} = -\frac{16}{3}\frac{1}{\tau_K}\left(\frac{d}{2}\right)^3 n^2 \qquad \textbf{(2.4.19)}$$

where the Kolmogorov time scale (for a $k-\omega$ model) is

$$\frac{1}{\tau_K} = \sqrt{\frac{C_\mu k\omega}{\upsilon}} \qquad \textbf{(2.4.20)}$$

and C_μ $(=0.09)$ is a model constant, k is the turbulence kinetic energy, and ω is the turbulence frequency.

The vapor-phase mass fraction expressed in conservative form is written as

$$\frac{\partial(\rho Y_v)}{\partial t} + \frac{\partial(\rho Y_v u_j)}{\partial x_j} = -\frac{M_w}{N_A}\left(g^* I + NF\right) \qquad \textbf{(2.4.21)}$$

where the source term consists of a portion due to the formation of critically-sized nuclei and a portion due to molecular condensation onto existing nuclei. The number of molecules which must coalesce in order to form a stable nucleus is given as [17]

$$g^* = \frac{32\pi}{3}\left(\frac{\sigma\left(v_e^l\right)^{2/3}}{k_b T}\right)^3\left(\frac{1}{\ln(S)}\right)^3 \qquad \textbf{(2.4.22)}$$

The molecular condensation rate is determined as follows

$$F = 2\pi dD\frac{\alpha_v}{m_e}\left(\rho_v - \rho_{v,eq}\right)\frac{1+Kn}{1+1.71Kn+1.333Kn^2} \quad \textbf{(2.4.23)}$$

where the Knudsen number is defined as

$$Kn = \frac{2\mu}{\rho_v d}\sqrt{\frac{\pi m_e}{2k_b T}} \quad \textbf{(2.4.24)}$$

and the diffusion coefficient D is defined by assuming a constant Schmidt number:

$$D = \frac{\mu}{Sc\rho_v} \quad \textbf{(2.4.25)}$$

The average droplet diameter is determined by the equivalence

$$\alpha_l = n\frac{\pi}{6}d^3 \quad \textbf{(2.4.26)}$$

In contrast to the homogeneous equilibrium model, the finite-rate formulation based on aerosol transport theory requires that the pressure and temperature solved be "working" thermodynamic variables, allowing the liquid and vapor densities ρ_v and ρ_l to be determined directly from the solution of the cubic equation of state. The finite-rate formulation assumes kinematic and thermal equilibrium between phases and is strictly valid in the metastable regions of the vapor dome.

2.5 MULTI-COMPONENT MIXTURES

Several cases involving the injection of supercritical ethylene/methane mixtures have been investigated in this research, since ethylene/methane mixtures are a more realistic surrogate for cracked JP-class fuels. The implementation of a binary mixture

requires additional terms and relations. In the following sections, multi-component mixture equilibrium criteria, mixing rules, and physical relations are introduced, and modifications to equations previously discussed are presented.

2.5.1 Multi-Component Mixture Phase Equilibria

At a given pressure, a pure fluid has a single boiling and condensation temperature as shown in Figure 2.5. However, boiling and condensation phenomena are more complex in multi-component mixtures, where at a given pressure and composition, the boiling and condensation temperatures have different values.

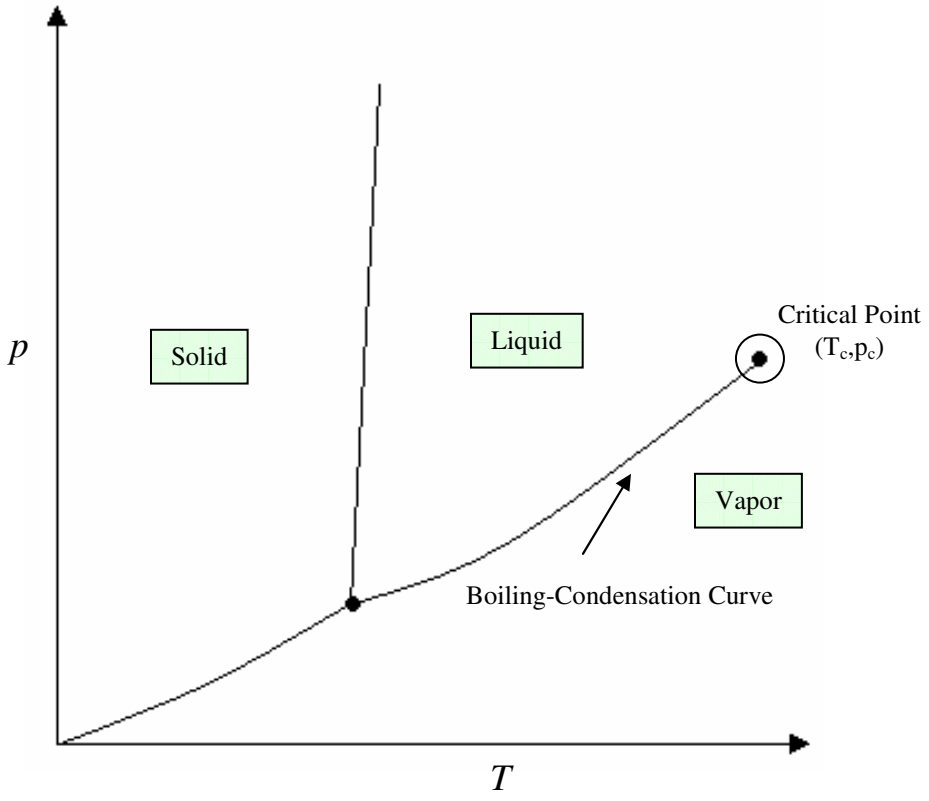

Figure 2.5: Boiling-Condensation Curve for a Pure Fluid

Consider the vaporization of a binary mixture, for simplicity, composed of 0.5 moles of component 1 $\left(x_1^l\right)$ and 0.5 moles of component 2 $\left(x_2^l\right)$, where $T_{c1} > T_{c2}$.

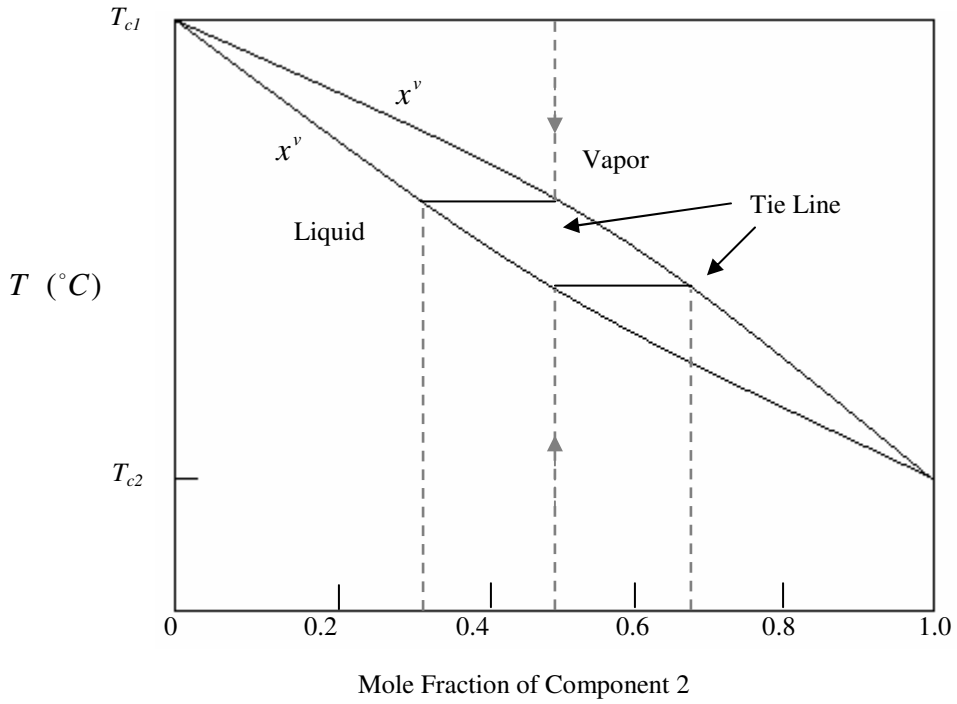

Figure 2.6: Bubble-Point and Dew-Point Curves for a Binary Mixture

At a given pressure, as the binary liquid is heated, it reaches a temperature at which the first bubble of vapor is formed, as shown in Figure 2.6. This temperature is known as the bubble-point temperature of the liquid. The composition of the liquid is essentially unchanged by its partial vaporization to form one small bubble and is used to determine the vapor composition of the small bubble (i.e. $x_2^v = 0.67$). The compositions of the two coexisting phases at a given pressure are given by the intersection of a horizontal line (i.e. line of constant temperature) with vapor and liquid curves. This line, which connects the equilibrium composition in two coexisting phases, is referred to as the tie line. Since the

vapor is richer in component 2 than the liquid mixture, as boiling proceeds the liquid mixture will be depleted of component 2. Consequently, as the mixture continues to vaporize, the liquid will become increasing more dilute in component 2 and its boiling point will increase.

In the same manner, consider the condensation of the same binary mixture consisting of 0.5 moles of component 1 $\left(x_1^v\right)$ and 0.5 moles of component 2 $\left(x_2^v\right)$. As the vapor temperature decreases at a fixed pressure, it reaches a temperature at which the first droplet of vapor condenses (Figure 2.6). This temperature is known as the dew-point temperature of the vapor. The composition of the vapor when forming a single small drop of liquid is essentially unchanged and is used to determine the liquid composition of the small droplet (i.e. $x_2^l = 0.31$). Clearly, as the condensation process continues, the vapor will become increasingly richer in component 2, and the equilibrium condensation temperature will decrease.

Therefore, the dew point and the bubble point are the equilibrium state of the mixture at a given pressure and composition (or temperature and composition), similar to the vaporization pressure in a single component mixture at a given temperature.

In this study the dew point curve is of interest since the conditions investigated for the ethylene/methane mixture involve phase transitions due to the condensation of the vapor mixture. The dew point (as well as the equilibrium liquid composition within the droplet) is calculated as a function of temperature and vapor composition by iteratively solving the equation

$$f_k^v\left(T,p,x_k^v\right)=f_k^l\left(T,p,x_k^l\right) \tag{2.5.1}$$

which satisfies the equilibrium criterion $\underline{G}_k^v=\underline{G}_k^l$ for a multi-component, two-phase mixture, where the fugacity $f_k^{v,l}$ is a function of the Gibbs free energy ($\underline{G}_k^v=\underline{G}_k^l \Rightarrow f_k^v=f_k^l$), as explained previously for a single component fluid.

2.5.2 Mixing Rules

The single-component parameters for the Peng-Robinson equation of state can be applied to a multi-component mixture via the following mixing rules:

$$a=\sum_i^{NS}\sum_j^{NS}x_i^I x_j^I a_{ij} \tag{2.5.2}$$

$$b=\sum_i^{NS}x_i^I b_i \tag{2.5.3}$$

where a_{ii} and b_i are the parameters for pure component i and

$$a_{ij}=\lambda_{ij}\sqrt{a_{ii}a_{jj}}=a_{ji} \tag{2.5.4}$$

In the above equation λ_{ij} is an empirically determined binary interaction coefficient characterizing the binary mixture formed by component i and component j. The ethylene/methane binary interaction parameter $\lambda_{ij}=0.977$ used in this work was computed by Nishiumi and Arai [26].

2.5.3 Mixture Fugacity

The definition of fugacity includes an entropy term; therefore, for a multi-component mixture the fugacity equation is different than for a single component due to the entropy of mixing. Therefore, the fugacity obtained by the Peng-Robinson equation of state for a multi-component mixture is given as follows:

$$\ln\frac{f_k^I}{x_k^I p}=\frac{B_k}{B}(Z-1)-\ln(Z-B)-\frac{A}{2\sqrt{2}B}\left[\frac{2\sum_l^{NS}x_l^I A_{kl}}{A}-\frac{B_k}{B}\right]\ln\left(\frac{Z+\left(1+\sqrt{2}\right)B}{Z+\left(1-\sqrt{2}\right)B}\right) \qquad \textbf{(2.5.5)}$$

where $A=\dfrac{a(T,x_k,...,x_{NS-1})p}{R^2T^2}$ and $B=\dfrac{b(x_k,...,x_{NS-1})p}{RT}$ as defined previously for a single component system.

2.5.4 Aerosol Transport

The extension of the homogeneous nucleation model to ethylene/methane mixtures assumes that the ethylene component is the only nucleating component in the mixture and that the equilibrium liquid composition within the droplet (given by dew point equilibrium calculations) may be achieved by the condensation of ethylene and methane molecules into the droplet. This assumption is substantiated by the fact that ethylene has a higher critical temperature than methane, which consequently leads to a higher pure component supersaturation value (higher nucleating potential) relative to the mixture temperature and pressure. In order to solve the two-phase, multi-component system, two additional moments of the GDE are introduced while the droplet number

density and vapor-mass fraction expressions are adapted for the binary system.

The total droplet number density is given as follows:

$$\frac{\partial N}{\partial t}+\frac{\partial\left(Nu_j\right)}{\partial x_j}=I_{C_2H_4}+\left.\frac{\partial N}{\partial t}\right|_{coag} \tag{2.5.6}$$

The nucleation rate $I_{C_2H_4}$ for ethylene is defined as:

$$I_{C_2H_4}=\sqrt{\frac{2\sigma}{\pi}}\left(\frac{x^v_{C_2H_4}pM_w}{RT}\right)\frac{\rho^v_{C_2H_4}\alpha_v}{\rho^l_{C_2H_4}m^{3/2}_{C_2H_4}}\exp\left(-\frac{16\pi}{3}\frac{\sigma^3_m\left(v^l_{C_2H_4}\right)^2}{\left(k_bT\right)^3}\left(\frac{1}{\ln\left(S_{C_2H_4}\right)}\right)^2\right) \tag{2.5.7}$$

where $m_{C_2H_4}=\frac{M_{w,C_2H_4}}{N_A}$ is the ethylene molecular mass and $v^l_{C_2H_4}=\frac{m_{C_2H_4}}{\rho^l_{C_2H_4}}$ is the liquid ethylene molecular volume.. The supersaturation S is defined as the ratio of the ethylene fugacity in the vapor phase and the equilibrium vapor ethylene fugacity $S_{C_2H_4}=\frac{f^v_{C_2H_4}}{f^v_{eq,C_2H_4}}$.

The interfacial tension σ_m of a liquid mixture is not a trivial function of the surface tension of the pure components because, in a mixture, the composition of the surface is not the same as the bulk. The Macleod-Sudgen correlation (known as the Parachor method) is modified for multi-component mixtures in the following manner [28]:

$$\sigma_m=\left[\left[P_{Lm}\right]\rho_l-\left[P_{Vm}\right]\rho_v\right]^{3.6} \tag{2.5.8}$$

where $\left[P_{Lm}\right]$ and $\left[P_{Vm}\right]$ are the parachors of the liquid and vapor mixture, respectively, and ρ_l and ρ_v are the liquid and vapor mixture densities. The parachor parameter for a

pure component can be estimated from the structure of the molecule or by experimental data. In this study the experimental data obtained by Quayle [29] was used, giving $[P_{C_2H_4}] = 100.3$ .and $[P_{CH_4}] = 72.6$.

The mixture parachor can be defined as follows:

$$[P_{Lm}] = \sum_{i}^{NS} \sum_{j}^{NS} x_i^l x_j^l [P_{ij}] \qquad \textbf{(2.5.9)}$$

$$[P_{Vm}] = \sum_{i}^{NS} \sum_{j}^{NS} x_i^v x_j^v [P_{ij}] \qquad \textbf{(2.5.10)}$$

The expression $\lfloor P_{ij} \rfloor$ can be written as

$$\lfloor P_{ij} \rfloor = \lambda_{ij} \frac{[P_i] + \lfloor P_j \rfloor}{2} \qquad \textbf{(2.5.11)}$$

where $[P_i]$ is the parachor of pure component *i*, and λ_{ij} is a binary interaction coefficient determined from experimental data. In the absence of experimental data, λ_{ij} may be set equal to one. For a binary mixture, the interfacial tension becomes:

$$\sigma_m^{1/3.6} = \left((x_1^l)^2 [P_1] + (x_2^l)^2 [P_2] + 2x_1^l x_2^l [P_{12}] \right) \rho_l + \left((x_1^v)^2 [P_1] + (x_2^v)^2 [P_2] + 2x_1^v x_2^v [P_{12}] \right) \rho_v \qquad \textbf{(2.5.12)}$$

The coagulation rate $\left.\frac{\partial N}{\partial t}\right|_{coag}$ definition remains unchanged for the binary system

$$\left.\frac{\partial N}{\partial t}\right|_{coag} = \left.\frac{\partial N}{\partial t}\right|_{turb} = -\frac{16}{3}\sqrt{\frac{C_\mu k \omega}{\upsilon}} \left(\frac{d}{2}\right)^3 n^2 \qquad \textbf{(2.5.13)}$$

where C_μ $(= 0.09)$ is a model constant, *k* is the turbulence kinetic energy, and ω is the

turbulence frequency.

The vapor-phase mass fraction expressed in conservative form is written as

$$\frac{\partial(\rho Y_v)}{\partial t}+\frac{\partial(\rho Y_v u_j)}{\partial x_j}=-\frac{M_{w,C_2H_4}}{N_A}\left(g^*_{C_2H_4} I_{C_2H_4}+NF_{C_2H_4}\right)-\frac{M_{w,CH_4}}{N_A}\left(NF_{CH_4}\right) \qquad \textbf{(2.5.14)}$$

where the source term consists of a nucleation and condensation term for ethylene as well as a condensation term for methane. The number of molecules in a critical nucleus is given as

$$g^* = \frac{32\pi}{3}\left(\frac{\sigma\left(v^l_{C_2H_4}\right)^{2/3}}{k_b T}\right)^3\left(\frac{1}{\ln\left(S_{C_2H_4}\right)}\right)^3 \qquad \textbf{(2.5.15)}$$

The molecular condensation rate for ethylene and methane are given respectively as

$$F_{C_2H_4} = 2\pi d D_{AB}\frac{\alpha_v}{m_{C_2H_4}}\left(\rho^v_{C_2H_4}-\rho^{v,eq}_{C_2H_4}\right)\frac{1+Kn}{1+1.71Kn+1.333Kn^2} \qquad \textbf{(2.5.16)}$$

$$F_{CH_4} = 2\pi d D_{AB}\frac{\alpha_v}{m_{CH_4}}\left(\rho^v_{CH_4}-\rho^{v,eq}_{CH_4}\right)\frac{1+Kn}{1+1.71Kn+1.333Kn^2} \qquad \textbf{(2.5.17)}$$

where the Knudsen number is defined as

$$Kn=\frac{2\mu}{\rho_v d}\sqrt{\frac{\pi m_m}{2k_b T}} \qquad \textbf{(2.5.18)}$$

with the average droplet diameter having the same definition as for the pure component. The vapor mixture molecular volume m_m is defined as

$$m_m = \frac{x^l_{C_2H_4} M_{w,C_2H_4} + x^l_{CH_4} M_{w,CH_4}}{N_A} \tag{2.5.19}$$

The binary diffusion coefficient D_{AB} at low to moderate pressures was developed by Chapman and Enskog by expanding the Boltzmann equation as a series expansion [28]. The working equation is given as:

$$D_{AB} = \frac{0.00266T^{3/2}}{pM_{AB}^{1/2}\sigma_{AB}^2\Omega_D} \tag{2.5.20}$$

where $M_{AB} = 2\left(\frac{1}{M_{w,C_2H_4}} + \frac{1}{M_{w,CH_4}}\right)^{-1}$ and the binary characteristic length of intermolecular forces is $\sigma_{AB} = \frac{\sigma_A + \sigma_B}{2}$. The collision integral Ω_D as a function of temperature is given as

$$\Omega_D = \frac{A}{\left(T^*\right)^B} + \frac{C}{\exp\left(DT^*\right)} + \frac{E}{\exp\left(FT^*\right)} + \frac{G}{\exp\left(HT^*\right)} \tag{2.5.21}$$

with $T^* = kT/\varepsilon_{AB}$ and $A = 1.06036$, $B = 0.15610$, $C = 0.19300$, $D = 0.47635$, $E = 1.03587$, $F = 1.52996$, $G = 1.76474$, $H = 3.89411$, and $\varepsilon_{AB} = \left(\varepsilon_A \varepsilon_B\right)^{1/2}$. The characteristic Lennard-Jones energy and length (ε and σ, respectively) are given for ethylene and methane as follows:

$$\varepsilon_{C_2H_4}/k = 224.7 \text{ K}$$

$$\varepsilon_{CH_4}/k = 148.6 \text{ K}$$

$$\sigma_{C_2H_4} = 4.163 \text{ Å}$$

$$\sigma_{CH_4} = 3.758 \text{ Å}$$

At low to moderate pressures, binary diffusion coefficients vary inversely with pressure or density. At high pressures, the product of Dp or $D\rho$ is no longer constant but decreases with an increase in either p or ρ. Also, at low pressures the binary diffusion coefficient is essentially independent of composition, while at high pressures, where the gas phase may deviate significantly from an ideal gas, small, but finite effects of composition have been noted. Since high pressures are encountered in this research, a corresponding states method is been implemented to account for real fluid effects and composition effects. The correlation is given as [28]

$$\frac{D_{AB}p}{(D_{AB}p)^{+}} = f(T_r, p_r) \tag{2.5.22}$$

where $(D_{AB}p)^{+}$ corresponds to the low pressure value calculated from Eq. (2.7.27) and function $f(T_r, p_r)$ is given by experimental data which has been approximated as follows:

$$f(T_r, p_r) \approx \begin{cases} g(T_r) = const \text{ for } (2.0 \le p_r \le 5.0) \\ \left(\dfrac{1.0 - g(T_r)}{2.0}\right) p_r + 1.0 \text{ for } (p_r < 2.0) \end{cases} \tag{2.5.23}$$

where $T_r = \dfrac{T}{T_c}$ and $p_r = \dfrac{p}{p_c}$. The function $g(T_r)$ has been curve fitted as follows:

$$g(T_r) = 0.1381T_r^{\,5} - 1.678T_r^{\,4} + 8.0351T_r^{\,3} - 19.045T_r^{\,2} + 22.553T_r - 9.8206 \qquad \textbf{(2.5.24)}$$

The ethylene vapor- and liquid-phase mass fractions can be found by solving the following equations respectively

$$\frac{\partial\left(\rho Y_v y^v_{C_2H_4}\right)}{\partial t} + \frac{\partial\left(\rho Y_v y^v_{C_2H_4} u_j\right)}{\partial x_j} = -\frac{M_{w,C_2H_4}}{N_A}\left(g^*_{C_2H_4} I_{C_2H_4} + NF_{C_2H_4}\right) \qquad \textbf{(2.5.25)}$$

$$\frac{\partial\left(\rho Y_l y^l_{C_2H_4}\right)}{\partial t} + \frac{\partial\left(\rho Y_l y^l_{C_2H_4} u_j\right)}{\partial x_j} = \frac{M_{w,C_2H_4}}{N_A}\left(g^*_{C_2H_4} I_{C_2H_4} + NF_{C_2H_4}\right) \qquad \textbf{(2.5.26)}$$

The above equations are additional moments from the GDE, which are necessary for closure of the binary-mixture sytem.

2.6 REYNOLDS AND FAVRE-AVERAGING

Since the computational grid is not suitable for the resolution of turbulent fluctuations of the various flow properties, a statistical approach introduced by Reynolds is implemented.

Reynolds' approach (known as Reynolds averaging) takes into consideration the effects of turbulent motion on the mean fluid properties by expressing each quantity as the sum of mean and fluctuating parts, and then taking its average over the time interval of interest. Therefore, the instantaneous magnitude of a flow property $f(\mathbf{x},t)$ is expressed as

$$f(\mathbf{x},t) = \bar{f}(\mathbf{x}) + f'(\mathbf{x},t) \qquad \textbf{(2.6.1)}$$

where $\bar{f}(\mathbf{x})$ is the mean component and $f'(\mathbf{x},t)$ is the fluctuating component, with the

mean component being defined as

$$\bar{f}(\mathbf{x}) = \lim_{\Delta t \to \infty} \frac{1}{\Delta t} \int_{t}^{t+\Delta t} f(\mathbf{x}, t) dt \qquad \textbf{(2.6.2)}$$

where the time interval Δt is much longer than the time scale of turbulence fluctuations but is much smaller than the time scale of the slow variations in the flow. After substituting the appropriately redefined variables into the Navier-Stokes equations, the Reynolds Averaged Navier-Stokes (RANS) equations are obtained.

Reynolds-averaging the whole compressible equation set will result in additional terms that increase the complexity of establishing suitable closure models. Favre averaging is implemented in order to simplify the averaging procedure for compressible flows. Flow properties are redefined as the sum of mean and fluctuating parts

$$f(\mathbf{x}, t) = \tilde{f}(\mathbf{x}) + f''(\mathbf{x}, t) \qquad \textbf{(2.6.3)}$$

where the Favre average quantity $\tilde{f}(\mathbf{x})$ is defined as

$$\tilde{f}(\mathbf{x}) = \frac{1}{\bar{\rho}} \lim_{\Delta t \to \infty} \frac{1}{\Delta t} \int_{t}^{t+\Delta t} \rho(\mathbf{x}, t) f(\mathbf{x}, t) dt = \frac{\overline{\rho u_i}}{\bar{\rho}} \qquad \textbf{(2.6.4)}$$

In order to mass average the Navier-Stokes equations, flow properties are decomposed as follows:

$$\rho = \bar{\rho} + \rho' \qquad p = \bar{p} + p' \qquad Y_m = \tilde{Y}_m + Y_m''$$

$$q_i = \bar{q}_i + q_i'' \qquad t_{ij} = \bar{t}_{ij} + t_{ij}' \qquad u_i = \tilde{u}_i + u_i''$$

$$h = \tilde{h} + h'' \qquad T = \tilde{T} + T'' \qquad u_i^{(m)} = \tilde{u}_i^{(m)} + u_i^{(m)''}$$

Substituting the above definitions into the Navier-Stokes equations and performing mass-averaging operations, the Favre-averaged compressible Navier-Stokes equations (also referred as RANS equations) are obtained as follows:

$$\frac{\partial\left(\bar{\rho}\tilde{Y}_v\tilde{y}_k^v\right)}{\partial t} + \frac{\partial}{\partial x_i}\left(\bar{\rho}\tilde{Y}_v\tilde{y}_k^v\tilde{u}_i + \left(\bar{\rho}\tilde{Y}_v\tilde{y}_k^v\tilde{u}_{d,k,i}^v + \Gamma_{k,i}^v\right)\right) = \omega_k^v \qquad \textbf{(2.6.5)}$$

$$\frac{\partial\left(\bar{\rho}\tilde{Y}_l\tilde{y}_k^l\right)}{\partial t} + \frac{\partial}{\partial x_i}\left(\bar{\rho}\tilde{Y}_l\tilde{y}_k^l\tilde{u}_i + \left(\bar{\rho}\tilde{Y}_l\tilde{y}_k^l\tilde{u}_{d,k,i}^l + \Gamma_{k,i}^l\right)\right) = \omega_k^l \qquad \textbf{(2.6.6)}$$

$$\frac{\partial\left(\bar{\rho}\tilde{Y}_v\right)}{\partial t} + \frac{\partial}{\partial x_i}\left(\bar{\rho}\tilde{Y}_v\tilde{u}_i + \left(\bar{\rho}\tilde{Y}_v\tilde{Y}_l\tilde{u}_{s,i} + \overline{\rho Y_v''Y_l\ u_{s,i}''}\right)\right) = \sum_{k=1}^{NV}\omega_k^v \qquad \textbf{(2.6.7)}$$

$$\frac{\partial\bar{\rho}}{\partial t} + \frac{\partial}{\partial x_i}\left(\bar{\rho}\tilde{u}_i\right) = 0 \qquad \textbf{(2.6.8)}$$

$$\frac{\partial\left(\bar{\rho}\tilde{u}_i\right)}{\partial t} + \frac{\partial}{\partial x_i}\left(\bar{\rho}\tilde{u}_i\tilde{u}_j + \delta_{ij}\bar{p} - \left(\bar{t}_{ij} + \tau_{ij}\right)\right) = 0 \qquad \textbf{(2.6.9)}$$

$$\frac{\partial\left(\bar{\rho}\tilde{H} - \bar{p}\right)}{\partial t} + \frac{\partial}{\partial x_i}\left(\bar{\rho}\tilde{H}\tilde{u}_i + \Gamma_H - \tilde{u}_j\left(\bar{t}_{ij} + \tau_{ij}\right) + \left(\bar{q}_i + q_{t,i}\right)\right) = 0 \qquad \textbf{(2.6.10)}$$

where

$$\Gamma_{k,i}^{v} = \overline{\rho Y_v'' \left(y_k^v\right)'' \left(u_{d,k,i}^v\right)''} \tag{2.6.11}$$

$$\Gamma_{k,i}^{l} = \overline{\rho Y_l'' \left(y_k^l\right)'' \left(u_{d,k,i}^l\right)''} \tag{2.6.12}$$

$$\Gamma_{H,i} = \sum_{k=1}^{NV} \overline{\rho Y_v'' \left(y_k^v\right)'' \left(H_k^v\right)'' \left(u_{d,k,i}^v\right)''} + \sum_{k=1}^{NL} \overline{\rho Y_l'' \left(y_k^l\right)'' \left(H_k^l\right)'' \left(u_{d,k,i}^l\right)''} \tag{2.6.13}$$

$$\bar{t}_{ij} = \mu\left(\tilde{T}\right)\left(\frac{\partial \tilde{u}_i}{\partial x_j} + \frac{\partial \tilde{u}_j}{\partial x_i} - \frac{2}{3}\delta_{ij}\frac{\partial \tilde{u}_k}{\partial x_k}\right) \tag{2.6.14}$$

$$\tau_{ij} = -\overline{\rho u_i'' u_j''} \tag{2.6.15}$$

$$\bar{q}_i = -\lambda\left(\tilde{T}\right)\frac{\partial \tilde{T}}{\partial x_i} \tag{2.6.16}$$

$$q_{t,i} = \overline{\rho u_i'' h''} \tag{2.6.17}$$

The turbulent diffusion terms, $\Gamma_{k,i}^{v}$, $\Gamma_{k,i}^{l}$ and Γ_H are expressed as (Appendix A):

$$\Gamma_{k,i}^{v} = -\frac{\mu_t}{Sc_t}\frac{\partial \tilde{Y}_v \tilde{y}_k^v}{\partial x_i} \tag{2.6.18}$$

$$\Gamma_{k,i}^{l} = -\frac{\mu_t}{Sc_t}\frac{\partial \tilde{Y}_l \tilde{y}_k^l}{\partial x_i} \tag{2.6.19}$$

$$\Gamma_{H,i} = -\frac{\mu_t}{Sc_t}\left[\left(H_v - H_L\right)\frac{\partial \tilde{Y}_v}{\partial x_i} + \tilde{Y}_v \sum_{k=1}^{NV} \frac{\partial H_v}{\partial \tilde{y}_k^v}\frac{\partial \tilde{y}_k^v}{\partial x_i} + \tilde{Y}_l \sum_{k=1}^{NL} \frac{\partial H_l}{\partial \tilde{y}_k^l}\frac{\partial \tilde{y}_k^l}{\partial x_i}\right] \quad \textbf{(2.6.20)}$$

The eddy viscosity $v_t = \frac{\mu_t}{\rho}$ is derived from turbulence model equations described later and the turbulent Schmidt number Sc_t, is assumed to be 0.9 in the current study. The Reynolds-stress tensor, τ_{ij} is modeled using the Boussinesq approximation, while the turbulent heat-flux vector, $q_{t,i}$, is modeled using the gradient diffusion approximation, given respectively:

$$\tau_{ij} = \mu_t\left(\tilde{T}\right)\left(\frac{\partial \tilde{u}_i}{\partial x_j} + \frac{\partial \tilde{u}_j}{\partial x_i} - \frac{2}{3}\delta_{ij}\frac{\partial \tilde{u}_k}{\partial x_k}\right) \quad \textbf{(2.6.21)}$$

$$q_{t,i} = \frac{C_p \mu_t}{\mathrm{Pr}_t}\frac{\partial \tilde{T}}{\partial x_i} \quad \textbf{(2.6.22)}$$

with the turbulent Prandtl number, Pr_t, assumed to have a constant value of 0.9 in this research.

2.7 TURBULENCE MODELING

The Favre-averaging of the governing equations discussed previously introduced three additional terms: the Reynolds-stress tensor, τ_{ij}, the turbulent heat-flux vector, $q_{t,i}$, and the turbulent diffusion terms, $\Gamma_{k,i}^I$ and $\Gamma_{H,i}$. All these terms are dependent on the turbulent kinematic eddy viscosity, $v_t = \frac{\mu_t}{\rho}$. The eddy viscosity is calculated using two

different approaches: Menter's one-equation model [24] and Menter's hybrid $k-\omega/k-\varepsilon$ shear stress transport (SST) [25].

The transport equations for the one equation model based on the $k-\varepsilon$ two equation model [24] is given by

$$\frac{\partial(\rho\tilde{\nu}_t)}{\partial t}+\frac{\partial(\rho\tilde{\nu}_t u_j)}{\partial x_j}=\rho c_1 D_1\tilde{\nu}_t\Omega-\rho c_2 E_{1e}+\frac{\partial}{\partial x_j}\left[\rho\left(\nu+\frac{\tilde{\nu}_t}{\sigma}\right)\frac{\partial\tilde{\nu}_t}{\partial x_j}\right] \qquad \textbf{(2.7.1)}$$

where Ω is the magnitude of the vorticity vector, D_1 and D_2 are damping functions, used to ensure that the model is numerically stable and does not require excessive grid resolution near the surface. The damping functions are defined as:

$$D_1=\frac{\nu_t+\nu}{\tilde{\nu}_t+\nu} \qquad \textbf{(2.7.2)}$$

$$D_2=1-\exp\left(-\frac{\tilde{\nu}_t}{A^+\kappa\nu}\right) \qquad \textbf{(2.7.3)}$$

where the corrected eddy viscosity $\tilde{\nu}_t$ and the high Reynolds eddy viscosity ν_t are related by:

$$\nu_t=D_2\tilde{\nu}_t \qquad \textbf{(2.7.4)}$$

The E_{1e} parameter is defined as:

$$E_{1e}=c_3E_{BB}\tanh\left(\frac{E_{k-\varepsilon}}{c_3E_{BB}}\right) \qquad \textbf{(2.7.5)}$$

$$E_{BB} = \frac{\partial \tilde{\nu}_t}{\partial x_j} \cdot \frac{\partial \tilde{\nu}_t}{\partial x_j} \tag{2.7.6}$$

$$E_{k-\varepsilon} = \tilde{\nu}_t \left(\frac{1}{L_{vK}} \right)^2 \tag{2.7.7}$$

where L_{vK} is the von Karman length scale. The model constants have the following value:

$$c_1 = 0.144\,,\ c_2 = \frac{c_1}{\kappa^2} + \frac{1}{\sigma} = 1.86\,,\ c_3 = 7$$

$$\kappa = 0.41\,,\ A^+ = 13$$

The transport equations for the turbulence kinematic energy, *k*, and the specific dissipation rate, ω for Menter's hybrid $k-\omega/k-\varepsilon$ shear stress transport (SST) model [25] are given by

$$\frac{\partial(\rho k)}{\partial t} + \frac{\partial(\rho k u_j)}{\partial x_j} = \mu_t \Omega^2 - \beta^* \rho \omega k + \frac{\partial}{\partial x_j}\left[(\mu + \sigma_k \mu_t) \frac{\partial k}{\partial x_j} \right] \tag{2.7.8}$$

$$\frac{\partial(\rho \omega)}{\partial t} + \frac{\partial(\rho \omega u_j)}{\partial x_j} = \gamma \rho \Omega^2 - \beta \rho \omega^2 + \frac{\partial}{\partial x_j}\left[(\mu + \sigma_\omega \mu_t) \frac{\partial \omega}{\partial x_j} \right] + 2(1 - F_1)\rho \sigma_{\omega 2} \frac{1}{\omega} \frac{\partial k}{\partial x_j} \frac{\partial \omega}{\partial x_j}$$

(2.7.9)

where Ω is the magnitude of the vorticity vector, and ϕ represents any constant in Menter's model $(\sigma_{k,} \sigma_\omega, ...)$, which is related by the blending function F_1

$$\phi = F_1\phi_1 + (1 - F_1)\phi_2 \tag{2.7.10}$$

where the ϕ_1 constants are from the $k-\omega$ equation:

$$\sigma_{k1} = 0.85,\ \sigma_{\omega 1} = 0.5,\ \beta_1 = 0.075$$

$$\beta^* = 0.09,\ \kappa = 0.41,\ \gamma_1 = \frac{\beta_1}{\beta^*} - \frac{\sigma_{\omega 1}\kappa^2}{\sqrt{\beta^*}}$$

and the ϕ_2 constants are from the standard $k-\varepsilon$ equation:

$$\sigma_{k2} = 1.0,\ \sigma_{\omega 2} = 0.856,\ \beta_2 = 0.0828$$

$$\beta^* = 0.09,\ \kappa = 0.41,\ \gamma_2 = \frac{\beta_2}{\beta^*} - \frac{\sigma_{\omega 2}\kappa^2}{\sqrt{\beta^*}}$$

The blending function F_1 is defined as

$$F_1 = \tanh\left(\arg_1^4\right),\ \arg_1 = \min\left[\max\left(\frac{\sqrt{k}}{0.09\omega y}, \frac{500\upsilon}{y^2\omega}\right), \frac{4\rho\sigma_{\omega 2}k}{CD_{kw}y^2}\right] \tag{2.7.11}$$

where y is the distance to the nearest wall, and CD_{kw} is the positive component of the cross-diffusion term in the above equation:

$$CD_{k\omega} = \max\left(2\rho\sigma_{\omega 2}\frac{1}{\omega}\frac{\partial k}{\partial x_j}\frac{\partial \omega}{\partial x_j}, 10^{-20}\right) \tag{2.7.12}$$

The eddy viscosity is defined as:

$$\upsilon_t = \frac{a_1 k}{\max(a_1\omega, \Omega F_2)} \tag{2.7.13}$$

where $a_1 = 0.31$ and F_2 is another blending function given by

$$F_2 = \tanh\left(\arg_2^2\right), \ \arg_2 = \max\left(2\frac{\sqrt{k}}{0.09\omega y}, \frac{500\upsilon}{y^2\omega}\right) \quad \textbf{(2.7.14)}$$

2.8 COORDINATE TRANSFORMATION

The Navier-Stokes equations may be written for a generalized coordinate system (ξ, η, ζ) according to the transformation of the independent variables in physical space (x, y, z) to a new set of independent variables in a uniform computational space (ξ, η, ζ). Using the chain rule of partial differentiation, the partial derivatives may be expressed as

$$\frac{\partial}{\partial x} = \xi_x \frac{\partial}{\partial \xi} + \eta_x \frac{\partial}{\partial \eta} + \zeta_x \frac{\partial}{\partial \zeta}$$

$$\frac{\partial}{\partial y} = \xi_y \frac{\partial}{\partial \xi} + \eta_y \frac{\partial}{\partial \eta} + \zeta_y \frac{\partial}{\partial \zeta}$$

$$\frac{\partial}{\partial z} = \xi_z \frac{\partial}{\partial \xi} + \eta_z \frac{\partial}{\partial \eta} + \zeta_z \frac{\partial}{\partial \zeta}$$

Given the above relation, the governing equations, written in strong conservation law, vector form for generalized coordinates can be written as

$$\frac{\partial \mathbf{U}}{\partial t} + \frac{\partial(\mathbf{E} - \mathbf{E}_\mathrm{v})}{\partial \xi} + \frac{\partial(\mathbf{F} - \mathbf{F}_\mathrm{v})}{\partial \eta} + \frac{\partial(\mathbf{G} - \mathbf{G}_\mathrm{v})}{\partial \zeta} = \mathbf{S} \quad \textbf{(2.8.1)}$$

where $\mathbf{U}$ is the vector of conservative variables, $\mathbf{E}$, $\mathbf{F}$ and $\mathbf{G}$ are the inviscid fluxes, $\mathbf{E}_\mathrm{v}$, $\mathbf{F}_\mathrm{v}$ and $\mathbf{G}_\mathrm{v}$ are the viscous fluxes, and $\mathbf{S}$ is the vector source terms, expressed separately as

$$\mathbf{U} = \frac{1}{J}\begin{bmatrix} \overline{\rho}\widetilde{Y}_v\widetilde{y}_1^v \\ \vdots \\ \overline{\rho}\widetilde{Y}_v\widetilde{y}_{NV-1}^v \\ \overline{\rho}\widetilde{Y}_l\widetilde{y}_1^l \\ \vdots \\ \overline{\rho}\widetilde{Y}_l\widetilde{y}_{NL-1}^l \\ \overline{\rho}\widetilde{Y}_v \\ \overline{\rho} \\ \overline{\rho}\widetilde{u} \\ \overline{\rho}\widetilde{v} \\ \overline{\rho}\widetilde{w} \\ \overline{\rho}\widetilde{H} - \overline{p} \end{bmatrix} \tag{2.8.2}$$

$$\mathbf{E} = \frac{1}{J}\begin{bmatrix} \overline{\rho}\widetilde{Y}_v\widetilde{y}_1^v U_C \\ \vdots \\ \overline{\rho}\widetilde{Y}_v\widetilde{y}_{NV-1}^v U_C \\ \overline{\rho}\widetilde{Y}_l\widetilde{y}_1^l U_C \\ \vdots \\ \overline{\rho}\widetilde{Y}_l\widetilde{y}_{NL-1}^l U_C \\ \overline{\rho}\widetilde{Y}_v U_C \\ \overline{\rho}U_C \\ \overline{\rho}\widetilde{u}U_C + \xi_x\overline{p} \\ \overline{\rho}\widetilde{v}U_C + \xi_y\overline{p} \\ \overline{\rho}\widetilde{w}U_C + \xi_z\overline{p} \\ \overline{\rho}\widetilde{H}U_C \end{bmatrix}, \quad \mathbf{F} = \frac{1}{J}\begin{bmatrix} \overline{\rho}\widetilde{Y}_v\widetilde{y}_1^v V_C \\ \vdots \\ \overline{\rho}\widetilde{Y}_v\widetilde{y}_{NV-1}^v V_C \\ \overline{\rho}\widetilde{Y}_l\widetilde{y}_1^l V_C \\ \vdots \\ \overline{\rho}\widetilde{Y}_l\widetilde{y}_{NL-1}^l V_C \\ \overline{\rho}\widetilde{Y}_v V_C \\ \overline{\rho}V_C \\ \overline{\rho}\widetilde{u}V_C + \eta_x\overline{p} \\ \overline{\rho}\widetilde{v}V_C + \eta_y\overline{p} \\ \overline{\rho}\widetilde{w}V_C + \eta_z\overline{p} \\ \overline{\rho}\widetilde{H}V_C \end{bmatrix}, \quad \mathbf{G} = \frac{1}{J}\begin{bmatrix} \overline{\rho}\widetilde{Y}_v\widetilde{y}_1^v W_C \\ \vdots \\ \overline{\rho}\widetilde{Y}_v\widetilde{y}_{NV-1}^v W_C \\ \overline{\rho}\widetilde{Y}_l\widetilde{y}_1^l W_C \\ \vdots \\ \overline{\rho}\widetilde{Y}_l\widetilde{y}_{NL-1}^l W_C \\ \overline{\rho}\widetilde{Y}_v W_C \\ \overline{\rho}W_C \\ \overline{\rho}\widetilde{u}W_C + \zeta_x\overline{p} \\ \overline{\rho}\widetilde{v}W_C + \zeta_y\overline{p} \\ \overline{\rho}\widetilde{w}W_C + \zeta_z\overline{p} \\ \overline{\rho}\widetilde{H}W_C \end{bmatrix} \tag{2.8.3}$$

$$\mathbf{E}_{\mathbf{v}} = \frac{1}{J}\begin{bmatrix} -\overline{\rho}\widetilde{Y}_v \tilde{y}_1^v U_{d,1}^v \\ \vdots \\ -\overline{\rho}\widetilde{Y}_v \tilde{y}_{NV-1}^v U_{d,NV-1}^v \\ -\overline{\rho}\widetilde{Y}_l \tilde{y}_1^l U_{d,1}^l \\ \vdots \\ -\overline{\rho}\widetilde{Y}_l \tilde{y}_{NL-1}^l U_{d,NL-1}^l \\ -\overline{\rho}\widetilde{Y}_v \sum_{k=1}^{NV} \tilde{y}_k^v U_{d,k}^v \\ 0 \\ \xi_{x_i}\left(\bar{t}_{ix} + \tau_{ix}\right) \\ \xi_{x_i}\left(\bar{t}_{iy} + \tau_{iy}\right) \\ \xi_{x_i}\left(\bar{t}_{iz} + \tau_{iz}\right) \\ -\overline{\rho}\left(\widetilde{Y}_v \sum_{k=1}^{NV} \tilde{y}_k^v \tilde{H}_k^v U_{d,k}^v + \widetilde{Y}_l \sum_{k=1}^{NL} \tilde{y}_k^l \tilde{H}_k^l U_{d,k}^l\right) + \xi_{x_i}\left[\tilde{u}_j\left(\bar{t}_{ij} + \tau_{ij}\right) - \left(\bar{q}_i + q_{t,i}\right)\right] \end{bmatrix} \qquad \textbf{(2.8.4)}$$

$$\mathbf{F}_{\mathbf{v}} = \frac{1}{J}\begin{bmatrix} -\overline{\rho}\widetilde{Y}_v \tilde{y}_1^v V_{d,1}^v \\ \vdots \\ -\overline{\rho}\widetilde{Y}_v \tilde{y}_{NV-1}^v V_{d,NV-1}^v \\ -\overline{\rho}\widetilde{Y}_l \tilde{y}_1^l V_{d,1}^l \\ \vdots \\ -\overline{\rho}\widetilde{Y}_l \tilde{y}_{NL-1}^l V_{d,NL-1}^l \\ -\overline{\rho}\widetilde{Y}_v \sum_{k=1}^{NV} \tilde{y}_k^v V_{d,k}^v \\ 0 \\ \eta_{x_i}\left(\bar{t}_{ix} + \tau_{ix}\right) \\ \eta_{x_i}\left(\bar{t}_{iy} + \tau_{iy}\right) \\ \eta_{x_i}\left(\bar{t}_{iz} + \tau_{iz}\right) \\ -\overline{\rho}\left(\widetilde{Y}_v \sum_{k=1}^{NV} \tilde{y}_k^v \tilde{H}_k^v V_{d,k}^v + \widetilde{Y}_l \sum_{k=1}^{NL} \tilde{y}_k^l \tilde{H}_k^l V_{d,k}^l\right) + \eta_{x_i}\left[\tilde{u}_j\left(\bar{t}_{ij} + \tau_{ij}\right) - \left(\bar{q}_i + q_{t,i}\right)\right] \end{bmatrix} \qquad \textbf{(2.8.5)}$$

$$\mathbf{G}_{\mathbf{v}} = \frac{1}{J}\begin{bmatrix} -\overline{\rho}\tilde{Y}_v \tilde{y}_1^{\,v} W_{d,1}^{v} \\ \vdots \\ -\overline{\rho}\tilde{Y}_v \tilde{y}_{NV-1}^{\,v} W_{d,NV-1}^{v} \\ -\overline{\rho}\tilde{Y}_l \tilde{y}_1^{\,l} W_{d,1}^{l} \\ \vdots \\ -\overline{\rho}\tilde{Y}_l \tilde{y}_{NL-1}^{\,l} W_{d,NL-1}^{l} \\ -\overline{\rho}\tilde{Y}_v \sum_{k=1}^{NV} \tilde{y}_k^{\,v} W_{d,k}^{v} \\ 0 \\ \zeta_{x_i}\left(\bar{t}_{ix} + \tau_{ix}\right) \\ \zeta_{x_i}\left(\bar{t}_{iy} + \tau_{iy}\right) \\ \zeta_{x_i}\left(\bar{t}_{iz} + \tau_{iz}\right) \\ -\overline{\rho}\left(\tilde{Y}_v \sum_{k=1}^{NV} \tilde{y}_k^{\,v} \tilde{H}_k^{\,v} W_{d,k}^{v} + \tilde{Y}_l \sum_{k=1}^{NL} \tilde{y}_k^{\,l} \tilde{H}_k^{\,l} W_{d,k}^{l}\right) + \zeta_{x_i}\left[\tilde{u}_j\left(\bar{t}_{ij} + \tau_{ij}\right) - \left(\overline{q}_i + q_{t,i}\right)\right] \end{bmatrix} \tag{2.8.6}$$

$$\mathbf{S} = \frac{1}{J}\begin{bmatrix} \omega_1^{v} \\ \vdots \\ \omega_{NV-1}^{v} \\ \omega_1^{l} \\ \vdots \\ \omega_{NL-1}^{l} \\ \sum_{k=1}^{NV} \omega_k^{v} \\ 0 \\ 0 \\ 0 \\ 0 \\ 0 \end{bmatrix} \tag{2.8.7}$$

In the above equations, U_c, V_c, and W_c are the contravariant velocity components and $U_{d,k}^{v,l}$, $V_{d,k}^{v,l}$, and $W_{d,k}^{v,l}$ are the contravariant diffusion velocities for component k in the vapor or liquid phase. The contravariant velocity components have the following form

$$U_c = \xi_{x_i}\tilde{u}_i = \xi_x\tilde{u} + \xi_y\tilde{v} + \xi_z\tilde{w}$$

$$V_c = \eta_{x_i}\tilde{u}_i = \eta_x\tilde{u} + \eta_y\tilde{v} + \eta_z\tilde{w} \qquad \textbf{(2.8.8)}$$

$$W_c = \zeta_{x_i}\tilde{u}_i = \zeta_x\tilde{u} + \zeta_y\tilde{v} + \zeta_z\tilde{w}$$

$$U^{v,l}_{d,k} = \xi_{x_i}\tilde{u}^{v,l}_{d,k,i} = \xi_x\tilde{u}^{v,l}_{d,k} + \xi_y\tilde{v}^{v,l}_{d,k} + \xi_z\tilde{w}^{v,l}_{d,k}$$

$$V^{v,l}_{d,k} = \eta_{x_i}\tilde{u}^{v,l}_{d,k,i} = \eta_x\tilde{u}^{v,l}_{d,k} + \eta_y\tilde{v}^{v,l}_{d,k} + \eta_z\tilde{w}^{v,l}_{d,k} \qquad \textbf{(2.8.9)}$$

$$W^{v,l}_{d,k} = \zeta_{x_i}\tilde{u}^{v,l}_{d,k,i} = \zeta_x\tilde{u}^{v,l}_{d,k} + \zeta_y\tilde{v}^{v,l}_{d,k} + \zeta_z\tilde{w}^{v,l}_{d,k}$$

and J is the Jacobian of coordinate transformation defined and evaluated as

$$J = 1/J^{-1} = 1/\frac{\partial(x,y,z)}{\partial(\xi,\eta,\zeta)} = 1/\begin{vmatrix} x_\xi & x_\eta & x_\zeta \\ y_\xi & y_\eta & y_\zeta \\ z_\xi & z_\eta & z_\zeta \end{vmatrix} \qquad \textbf{(2.8.10)}$$

where $x_\xi, x_\eta, x_\zeta, y_\xi, y_\eta, y_\zeta, z_\xi, z_\eta$ and z_ζ are the inverse metric derivatives and are evaluated by second-order finite differences.

3 NUMERICAL METHODS

The following discussion outlines the main algorithms required for the solution of the Navier-Stokes equations with the aerosol transport equations, and turbulence modelling incorporated. These methods include a time-derivative preconditioning method, a low-diffusion upwinding scheme, and time integration approaches to solve the non-linear system.

3.1 TIME-DERIVATIVE PRECONDITIONING

Two-phase flows (liquid/vapor) have a broad range of Mach numbers due to the discrepancy in the speed of sound from one phase to the other. The speed of sound of a fluid in the liquid phase can be much higher than the fluid in the vapor phase or in a two-phase mixture. As a result, the Mach number of the liquid is much smaller, $M \to 0$ than in the vapor or a two-phase mixture.

Conventional time marching algorithms encounter convergence difficulties at low Mach numbers due to the discrepancy in characteristic wave speeds. These waves speeds, which are the eigenvalues of the inviscid flux Jacobian (i.e., for one-dimensional system, u and $u \pm a$), dictate the rate at which errors present in the characteristic variables are convected out of the system. At low Mach numbers, the error convected at u and errors convected at $u \pm a$ propagate at widely varying time scales. This results in poor convergence rates since stability constraints typically require the selection of the time step associated with the fastest wave speed. Preconditioning methods introduce pseudo time-derivatives which alter the characteristic waves (i.e., $u \pm a$) so that they

propagate at speeds that are comparable in magnitude to the convective velocity. This approach makes the system well-conditioned by eliminating the wide disparity in the wave speeds as the Mach number is reduced.

The preconditioned Navier-Stokes equations used in this study, including turbulence models as well as the moments for the GDE, have the following form

$$\frac{1}{J}\left(\mathbf{P}\frac{\partial \mathbf{V}}{\partial t}\right)+\frac{\partial\left(\mathbf{E}-\mathbf{E}_{\mathrm{v}}\right)}{\partial \xi}+\frac{\partial\left(\mathbf{F}-\mathbf{F}_{\mathrm{v}}\right)}{\partial \eta}+\frac{\partial\left(\mathbf{G}-\mathbf{G}_{\mathrm{v}}\right)}{\partial \zeta}=\mathbf{S} \tag{3.1.1}$$

where $\mathbf{P}$ is a preconditioning matrix, $\mathbf{V}$ is the vector of primitive variables, $\mathbf{E}$, $\mathbf{F}$ and $\mathbf{G}$ are the inviscid fluxes, $\mathbf{E}_{\mathrm{v}}$, $\mathbf{F}_{\mathrm{v}}$ and $\mathbf{G}_{\mathrm{v}}$ are the viscous fluxes, and $\mathbf{S}$ is the vector source terms, expressed separately as

$$\mathbf{V}=\begin{bmatrix} N \\ y^{v}_{C_2H_4} \\ y^{l}_{C_2H_4} \\ Y_v \\ f \\ u \\ v \\ w \\ T \\ \phi_{\tilde{\nu}_t}\tilde{\nu}_t \\ \left(1-\phi_{\tilde{\nu}_t}\right)k \\ \left(1-\phi_{\tilde{\nu}_t}\right)\omega \end{bmatrix}, \mathbf{U}=\frac{1}{J}\begin{bmatrix} \overline{\rho}N \\ \overline{\rho}\tilde{Y}_v\tilde{y}^{v}_{C_2H_4} \\ \overline{\rho}\tilde{Y}_l\tilde{y}^{l}_{C_2H_4} \\ \overline{\rho}\tilde{Y}_v \\ \overline{\rho} \\ \overline{\rho}\tilde{u} \\ \overline{\rho}\tilde{v} \\ \overline{\rho}\tilde{w} \\ \overline{\rho}\tilde{H}-\overline{p} \\ \phi_{\tilde{\nu}_t}\overline{\rho}\tilde{\nu}_t \\ \left(1-\phi_{\tilde{\nu}_t}\right)\overline{\rho}k \\ \left(1-\phi_{\tilde{\nu}_t}\right)\overline{\rho}\omega \end{bmatrix} \tag{3.1.2}$$

$$\mathbf{E}=\frac{1}{J}\begin{bmatrix}\overline{\rho}NU_C\\ \overline{\rho}\widetilde{Y}_v\tilde{y}^v_{C_2H_4}U_C\\ \overline{\rho}\widetilde{Y}_l\tilde{y}^l_{C_2H_4}U_C\\ \overline{\rho}\widetilde{Y}_vU_C\\ \overline{\rho}U_C\\ \overline{\rho}\tilde{u}U_C+\xi_x\overline{p}\\ \overline{\rho}\tilde{v}U_C+\xi_y\overline{p}\\ \overline{\rho}\tilde{w}U_C+\xi_z\overline{p}\\ \overline{\rho}\widetilde{H}U_C\\ \phi_{\tilde{v}_t}\overline{\rho}\tilde{v}_tU_C\\ \left(1-\phi_{\tilde{v}_t}\right)\overline{\rho}kU_C\\ \left(1-\phi_{\tilde{v}_t}\right)\overline{\rho}\omega U_C\end{bmatrix},\ \mathbf{F}=\frac{1}{J}\begin{bmatrix}\overline{\rho}NV_C\\ \overline{\rho}\widetilde{Y}_v\tilde{y}^v_{C_2H_4}V_C\\ \overline{\rho}\widetilde{Y}_l\tilde{y}^l_{C_2H_4}V_C\\ \overline{\rho}\widetilde{Y}_vV_C\\ \overline{\rho}V_C\\ \overline{\rho}\tilde{u}V_C+\eta_x\overline{p}\\ \overline{\rho}\tilde{v}V_C+\eta_y\overline{p}\\ \overline{\rho}\tilde{w}V_C+\eta_z\overline{p}\\ \overline{\rho}\widetilde{H}V_C\\ \phi_{\tilde{v}_t}\overline{\rho}\tilde{v}_tV_C\\ \left(1-\phi_{\tilde{v}_t}\right)\overline{\rho}kV_C\\ \left(1-\phi_{\tilde{v}_t}\right)\overline{\rho}\omega V_C\end{bmatrix},\ \mathbf{G}=\frac{1}{J}\begin{bmatrix}\overline{\rho}NW_C\\ \overline{\rho}\widetilde{Y}_v\tilde{y}^v_{C_2H_4}W_C\\ \overline{\rho}\widetilde{Y}_l\tilde{y}^l_{C_2H_4}W_C\\ \overline{\rho}\widetilde{Y}_vW_C\\ \overline{\rho}W_C\\ \overline{\rho}\tilde{u}W_C+\zeta_x\overline{p}\\ \overline{\rho}\tilde{v}W_C+\zeta_y\overline{p}\\ \overline{\rho}\tilde{w}W_C+\zeta_z\overline{p}\\ \overline{\rho}\widetilde{H}W_C\\ \phi_{\tilde{v}_t}\overline{\rho}\tilde{v}_tW_C\\ \left(1-\phi_{\tilde{v}_t}\right)\overline{\rho}kW_C\\ \left(1-\phi_{\tilde{v}_t}\right)\overline{\rho}\omega W_C\end{bmatrix} \qquad \textbf{(3.1.3)}$$

$$\mathbf{E}_{\mathbf{v}}=\frac{1}{J}\begin{bmatrix}\left(\mu+\mu_t\right)\dfrac{\partial N}{\partial x}\\ \lambda_{\tilde{y}^v_{C_2H_4},x}\\ \lambda_{\tilde{y}^l_{C_2H_4},x}\\ \lambda_{\tilde{Y}_v,x}\\ 0\\ \xi_{x_i}\left(\bar{t}_{ix}+\tau_{ix}\right)\\ \xi_{x_i}\left(\bar{t}_{iy}+\tau_{iy}\right)\\ \xi_{x_i}\left(\bar{t}_{iz}+\tau_{iz}\right)\\ \lambda_{\tilde{H},x}+\xi_{x_i}\left[\tilde{u}_j\left(\bar{t}_{ij}+\tau_{ij}\right)-\left(\bar{q}_i+q_{t,i}\right)\right]\\ \phi_{\tilde{v}_t}\xi_{x_i}\Theta_i^{\tilde{v}_t}\\ \left(1-\phi_{\tilde{v}_t}\right)\xi_{x_i}\Theta_i^{k}\\ \left(1-\phi_{\tilde{v}_t}\right)\xi_{x_i}\Theta_i^{\omega}\end{bmatrix} \qquad \textbf{(3.1.4)}$$

$$\mathbf{F_v} = \frac{1}{J}\begin{bmatrix} (\mu+\mu_t)\dfrac{\partial N}{\partial y} \\ \lambda_{\tilde{y}^v_{C_2H_4},y} \\ \lambda_{\tilde{y}^l_{C_2H_4},y} \\ \lambda_{\tilde{Y}_v,y} \\ 0 \\ \eta_{x_i}\left(\bar{t}_{ix}+\tau_{ix}\right) \\ \eta_{x_i}\left(\bar{t}_{iy}+\tau_{iy}\right) \\ \eta_{x_i}\left(\bar{t}_{iz}+\tau_{iz}\right) \\ \lambda_{\tilde{H},y}+\eta_{x_i}\left[\tilde{u}_j\left(\bar{t}_{ij}+\tau_{ij}\right)-\left(\bar{q}_i+q_{t,i}\right)\right] \\ \phi_{\tilde{v}_t}\eta_{x_i}\Theta_i^{\tilde{v}_t} \\ \left(1-\phi_{\tilde{v}_t}\right)\eta_{x_i}\Theta_i^{k} \\ \left(1-\phi_{\tilde{v}_t}\right)\eta_{x_i}\Theta_i^{\omega} \end{bmatrix} \tag{3.1.5}$$

$$\mathbf{G_v} = \frac{1}{J}\begin{bmatrix} (\mu+\mu_t)\dfrac{\partial N}{\partial z} \\ \lambda_{\tilde{y}^v_{C_2H_4},z} \\ \lambda_{\tilde{y}^l_{C_2H_4},z} \\ \lambda_{\tilde{Y}_v,z} \\ 0 \\ \zeta_{x_i}\left(\bar{t}_{ix}+\tau_{ix}\right) \\ \zeta_{x_i}\left(\bar{t}_{iy}+\tau_{iy}\right) \\ \zeta_{x_i}\left(\bar{t}_{iz}+\tau_{iz}\right) \\ \lambda_{\tilde{H},z}+\zeta_{x_i}\left[\tilde{u}_j\left(\bar{t}_{ij}+\tau_{ij}\right)-\left(\bar{q}_i+q_{t,i}\right)\right] \\ \phi_{\tilde{v}_t}\zeta_{x_i}\Theta_i^{\tilde{v}_t} \\ \left(1-\phi_{\tilde{v}_t}\right)\zeta_{x_i}\Theta_i^{k} \\ \left(1-\phi_{\tilde{v}_t}\right)\zeta_{x_i}\Theta_i^{\omega} \end{bmatrix} \tag{3.1.6}$$

$$\mathbf{S} = \begin{bmatrix} S_N \\ S^v_{C_2H_4} \\ -S^v_{C_2H_4} \\ S^v_{C_2H_4} + S^v_{CH_4} \\ 0 \\ 0 \\ 0 \\ 0 \\ 0 \\ \phi_{\tilde{v}_t} S_{\tilde{v}_t} \\ \left(1-\phi_{\tilde{v}_t}\right) S_k \\ \left(1-\phi_{\tilde{v}_t}\right) S_\omega \end{bmatrix} \tag{3.1.7}$$

where

$$\lambda_{\tilde{y}^v_{C_2H_4}, x_i} = \left(\frac{\mu}{Sc} + \frac{\mu_t}{Sc_t}\right) \frac{\partial \tilde{Y}_v \tilde{y}^v_{C_2H_4}}{\partial x_i} \tag{3.1.8}$$

$$\lambda_{\tilde{y}^l_{C_2H_4}, x_i} = \left(\frac{\mu}{Sc} + \frac{\mu_t}{Sc_t}\right) \frac{\partial \tilde{Y}_v \tilde{y}^l_{C_2H_4}}{\partial x_i} \tag{3.1.9}$$

$$\lambda_{\tilde{Y}_v, x_i} = \left(\frac{\mu}{Sc} + \frac{\mu_t}{Sc_t}\right) \frac{\partial \tilde{Y}_v}{\partial x_i} \tag{3.1.10}$$

$$\lambda_{H, x_i} = \left(\frac{\mu}{Sc} + \frac{\mu_t}{Sc_t}\right) \left[\left(H_v - H_L\right) \frac{\partial \tilde{Y}_v}{\partial x_i} + \tilde{Y}_v \sum_{k=1}^{NV} \frac{\partial H_v}{\partial \tilde{y}^v_k} \frac{\partial \tilde{y}^v_k}{\partial x_i} + \tilde{Y}_l \sum_{k=1}^{NL} \frac{\partial H_l}{\partial \tilde{y}^l_k} \frac{\partial \tilde{y}^l_k}{\partial x_i} \right] \tag{3.1.11}$$

$$S_N = \overline{\rho} \left(I_{C_2H_4} + \left.\frac{\partial N}{\partial t}\right|_{coag} \right) - \overline{\rho} N \left(\frac{\partial \tilde{u}}{\partial x} + \frac{\partial \tilde{v}}{\partial y} + \frac{\partial \tilde{w}}{\partial z} \right) \tag{3.1.12}$$

$$S^{v}_{C_2H_4} = -\frac{M_{w,C_2H_4}}{N_A}\left(g^{*}_{C_2H_4} I_{C_2H_4} + NF_{C_2H_4}\right) \tag{3.1.13}$$

$$S^{v}_{CH_4} = -\frac{M_{w,CH_4}}{N_A}\left(NF_{CH_4}\right) \tag{3.1.14}$$

$$S_{\tilde{\nu}_t} = \rho c_1 D_1 \tilde{\nu}_t \Omega - \rho c_2 E_{1e} \tag{3.1.15}$$

$$S_k = \mu_t \Omega^2 - \beta^* \rho \omega k \tag{3.1.16}$$

$$S_\omega = \gamma \rho \Omega^2 - \beta \rho \omega^2 + 2(1 - F_1)\rho \sigma_{\omega 2} \frac{1}{\omega}\left(\frac{\partial k}{\partial x}\frac{\partial \omega}{\partial x} + \frac{\partial k}{\partial y}\frac{\partial \omega}{\partial y} + \frac{\partial k}{\partial z}\frac{\partial \omega}{\partial z}\right) \tag{3.1.17}$$

In this study two different sets of primitive variables are used depending on the type of two-phase model. When using the homogeneous equilibrium model $f = \rho$, while for the aerosol transport model $f = p$. The flag parameter $\phi_{\tilde{\nu}_t}$ determines which turbulence model is used in the simulation and is a value of 1 if the model is being used or 0 if the model is not being used.

The preconditioning matrix used in this study is that of Weiss and Smith [37], a variant of the Turkel [36], and Choi-Merkle [4] preconditioners. This preconditioner may be expressed as a rank-one perturbation of the Jacobian matrix $\frac{\partial \mathbf{U}}{\partial \mathbf{V}}$:

$$\mathbf{P} = \frac{\partial \mathbf{U}}{\partial \mathbf{V}} + \Theta \vec{u} \vec{v}^{\,T} \tag{3.1.18}$$

where

$$\vec{u} = \begin{bmatrix} N \\ y^{v}_{C_2H_4} \\ y^{l}_{C_2H_4} \\ Y_v \\ 1 \\ u \\ v \\ w \\ H \\ \tilde{\nu}_t \\ k \\ \omega \end{bmatrix}, \ \vec{v} = \begin{bmatrix} \partial p/\partial N \\ \partial p/\partial y^{v}_{C_2H_4} \\ \partial p/\partial y^{l}_{C_2H_4} \\ \partial p/\partial Y_v \\ \partial p/\partial f \\ \partial p/\partial u \\ \partial p/\partial v \\ \partial p/\partial w \\ \partial p/\partial T \\ \partial p/\partial \tilde{\nu}_t \\ \partial p/\partial k \\ \partial p/\partial \omega \end{bmatrix} = \begin{bmatrix} 0 \\ 0 \\ 0 \\ 0 \\ 1 \\ 0 \\ 0 \\ 0 \\ 0 \\ 0 \\ 0 \\ 0 \end{bmatrix}, \ \Theta = \frac{1}{V_{ref}^2} - \frac{1}{a^2} \qquad \textbf{(3.1.19)}$$

and V_{ref}^2 is a suitably-defined reference velocity. The speed of sound a is defined in Appendix B. In the limit of an incompressible flow $\left(a^2 \to \infty\right)$, this preconditioner reduces to a variant of Chorin's artificial compressibility method, while $\dfrac{\partial \mathbf{U}}{\partial \mathbf{V}}$ is recovered as $V_{ref}^2 \to a^2$. The reference velocity is typically defined as

$$V_{ref}^2 = \min\left(a^2, \max\left(\left|\vec{V}^2\right|, V_\infty^2\right)\right) \qquad \textbf{(3.1.20)}$$

where $\left|\vec{V}^2\right|$ is the local fluid velocity magnitude, and V_∞ is the user-specified cutoff velocity designed to prevent singular behavior in stagnation regions.

The eigenvalues of the flux Jacobian in the ξ-direction , $\mathbf{P}^{-1}\dfrac{\partial \mathbf{E}}{\partial \mathbf{V}}$, derived in Appendix C, are U_c and $U_c^{'} \pm a^{'}$,

$$U_c^{'} \pm a^{'} = \frac{1+M_{ref}^2}{2}\left[U_c \pm a\frac{\sqrt{\left(1-M_{ref}^2\right)^2 M^2 + 4M_{ref}^2}}{1-M_{ref}^2}\right] \quad \textbf{(3.1.21)}$$

$$U_c = \bar{\xi}_x u + \bar{\xi}_y v + \bar{\xi}_z w \quad \textbf{(3.1.22)}$$

$$\bar{\xi}_x = \frac{\xi_x}{|\nabla\xi|},\ \bar{\xi}_y = \frac{\xi_y}{|\nabla\xi|},\ \bar{\xi}_z = \frac{\xi_z}{|\nabla\xi|} \quad \textbf{(3.1.23)}$$

where U is the normal component of the contravariant velocity in the ξ direction, M_{ref} and M are the reference Mach number and the Mach number respectively

$$M_{ref} = \frac{V_{ref,un}}{a},\ M = \frac{U_c}{a} \quad \textbf{(3.1.24)}$$

This reference Mach number enables the flux splitting scheme to revert to its original formulation for $M > 1$.

3.2 UPWINDING SCHEME

In the context of Euler equations, upwinding refers to a method of discretization that is consistent with the way that physical information propagates. Upwind schemes, therefore, introduce physical properties of the flow equation into the discretized formulation.

The inviscid fluxes in the Navier-Stokes equations are discretized using Low-Diffusion Flux-Splitting Scheme (LDFSS) [6], which belongs to the 'AUSM-family' of upwinding schemes [21, 22]. These schemes are hybrid upwinding methods formulated

to combine the accuracy of flux-difference splitting methods with the numerical efficiency and compactness of flux-vector splitting formulations. Details regarding the development of LDFSS may be found in Ref. [6].

The version of LDFSS used in this investigation is valid for multi-component, real fluids undergoing phase transitions [7]. The viscous and diffusive terms in the governing equations are discretized using central differences. The algorithm is formulated as an upwinding procedure in one direction which is then applied to each spatial dimension. To avoid repetition, the LDFSS formulation is described for the ξ-direction flux only. The superscripts denoting Favre- and Reynolds-averaged quantities are omitted for simplicity. The inviscid ξ-direction flux $\mathbf{E}$ is comprised of convective and pressure contributions:

$$\mathbf{E} = \mathbf{E}^c + \mathbf{E}^p \tag{3.2.1}$$

where

$$\mathbf{E}^c = \frac{|\nabla \xi|}{J}\left(\rho U_c \tilde{\mathbf{E}}^c\right) \tag{3.2.2}$$

$$\mathbf{E}^p = \frac{|\nabla \xi|}{J}\left(P \tilde{\mathbf{E}}^p\right) \tag{3.2.3}$$

and

$$\tilde{\mathbf{E}}^c = \begin{bmatrix} N \\ Y_v y^v_{C_2H_4} \\ Y_l y^l_{C_2H_4} \\ Y_v \\ 1 \\ u \\ v \\ w \\ H \\ \tilde{\nu}_t \\ k \\ \omega \end{bmatrix}, \tilde{\mathbf{E}}^p = \begin{bmatrix} 0 \\ 0 \\ 0 \\ 0 \\ 0 \\ \overline{\xi}_x \\ \overline{\xi}_y \\ \overline{\xi}_z \\ 0 \\ 0 \\ 0 \\ 0 \end{bmatrix} \tag{3.2.4}$$

The upwinding stencil used for the LDFSS scheme is given in Figure 3.1. The discretization scheme implemented stores information of the inviscid ξ-direction flux vector at the mesh line intersection (cell interfaces), using the properties at the left $(L)$and right (R) states. As a result the convective and pressure parts of the inviscid flux vector are expressed as the sum of left and right components:

$$\mathbf{E}_{i+1/2} = \mathbf{E}^c_{i+1/2} + \mathbf{E}^p_{i+1/2} \tag{3.2.5}$$

$$\mathbf{E}^c_{i+1/2} = \frac{|\nabla \xi|}{J}\left(\rho_L U^+ \tilde{\mathbf{E}}^c_L + \rho_R U^- \tilde{\mathbf{E}}^c_R\right) \tag{3.2.6}$$

$$\mathbf{E}^p_{i+1/2} = \frac{|\nabla \xi|}{J} P_{1/2} \tilde{\mathbf{E}}^p \tag{3.2.7}$$

The velocities $U \pm$ and the interface pressure $P_{1/2}$ are defined as

$$U^{+} = \tilde{a}_{1/2}\left[\mathrm{M}^{+} - \mathrm{M}_{1/2}\left(1 - \frac{p_L - p_R}{2\rho_L V_{ref,1/2}^2}\right)\right]$$
$$U^{-} = \tilde{a}_{1/2}\left[\mathrm{M}^{-} + \mathrm{M}_{1/2}\left(1 + \frac{p_L - p_R}{2\rho_R V_{ref,1/2}^2}\right)\right] \quad \textbf{(3.2.8)}$$

$$P_{1/2} = \frac{1}{2}(p_L + p_R) + \frac{1}{2}(P^{+} - P^{-})(p_L - p_R) + \rho_{1/2} V_{ref,1/2}^2 (P^{+} + P^{-} - 1) \quad \textbf{(3.2.9)}$$

where $\rho_{1/2} = \frac{1}{2}(\rho_L + \rho_R)$, and $V_{ref,1/2}$ is the interface reference velocity. The numerical speed of sound $\tilde{a}_{1/2}$ derived from the acoustic eigenvalues of the preconditioned system and evaluated at the cell interface is given as

$$\tilde{a}_{1/2} = \left[\frac{\sqrt{(1 - M_{ref}^2)^2 U_c^2 + 4V_{ref}^2}}{1 + M_{ref}^2}\right]_{1/2} \quad \textbf{(3.2.10)}$$

where the subscript $1/2$ depicts the evaluation using cell-averaged velocity and speed data, and M_{ref} is the reference Mach number. The split Mach numbers in the above equations are defined as:

$$\mathrm{M}^{+} = \alpha_L^{+}(1 + \beta_L) M_L - \beta_L M_{(2),L}^{+}$$
$$\mathrm{M}^{-} = \alpha_R^{-}(1 + \beta_R) M_R - \beta_R M_{(2),R}^{-} \quad \textbf{(3.2.11)}$$

$$\alpha_{L,R}^{\pm} = \frac{1}{2}\left[1.0 \pm \mathrm{sign}(1.0, M_{L,R})\right] \quad \textbf{(3.2.12)}$$

$$\beta_{L,R} = -\max\left[0.0, 1.0 - \text{int}\left(\left|M_{L,R}\right|\right)\right] \tag{3.2.13}$$

$$\mathrm{M}_{1/2} = \frac{1}{2}\left(\mathrm{M}^{+} - \alpha_L^{+} M_L - \mathrm{M}^{-} + \alpha_R^{-} M_R\right) \tag{3.2.14}$$

$$P^{\pm} = \alpha_{L,R}^{\pm}\left(1 + \beta_{L,R}\right) - \frac{\beta_{L,R}}{2}\left(1.0 \pm M_{L,R}\right) \tag{3.2.15}$$

where the Mach numbers at left and right states, and Van Leer/Liou polynomials in Mach number [22] are given respectively

$$M_{L,R} = \frac{U_{c,L,R}}{\tilde{a}_{1/2}} \tag{3.2.16}$$

$$M_{(1)}^{\pm} = \frac{1}{2}\left(M \pm |M|\right) \tag{3.2.17}$$

$$M_{(2)}^{\pm} = \begin{cases} \pm\dfrac{1}{4}\left(M \pm 1\right)^2, & |M| < 1, \\ M_{(1)}^{\pm}, & \text{otherwise} \end{cases} \tag{3.2.18}$$

It is important to note that arithmetic averaging was used for calculating cell interface values.

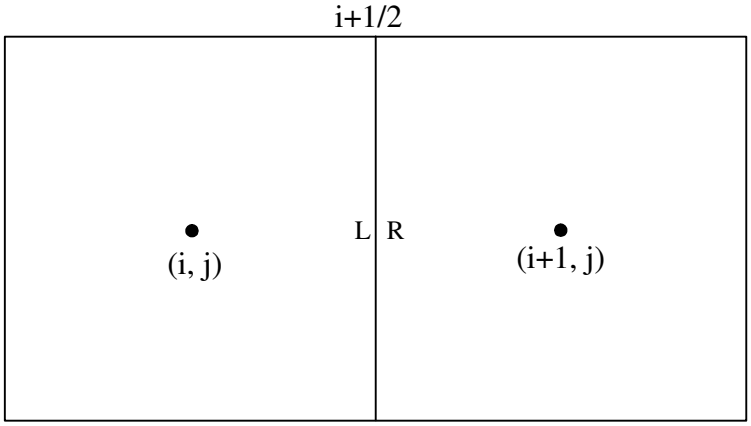

Figure 3.1: Upwinding Stencil Used for LDFSS Algorithm (ξ direction)

3.3 SECOND-ORDER EXTENSION

The second-order extension of the LDFSS is achieved by a total variation diminishing (TVD)-type limited interpolation [15] of the primitive variables to the cell interface.

The interpolation of an arbitrary property, f, to the left and right states can be expressed as:

$$f_L = f_i + \frac{1}{2} P_i^l \cdot \text{avg}\left(f_{i+1} - f_i, f_i - f_{i-1}\right)$$

$$f_R = f_{i+1} - \frac{1}{2} P_{i+1}^l \cdot \text{avg}\left(f_{i+2} - f_{i+1}, f_{i+1} - f_i\right) \quad \textbf{(3.3.1)}$$

where P^l is a pressure limiter introduced in [33] defined as:

$$P_i^l = 1.0 - \max\left[\frac{\left|(\Delta p)_i\right|}{\left|(\Delta p)_i\right| + \kappa_0 p_\infty}, \frac{\left|(\Delta \alpha_v)_i\right|}{\left|(\Delta \alpha_v)_i\right| + \kappa_0}\right] \tag{3.3.2}$$

$$(\Delta p)_i = p_{i+1} - p_{i-1}, \; (\Delta \alpha_v)_i = (\alpha_v)_{i+1} - (\alpha_v)_{i-1} \tag{3.3.3}$$

where κ_0 is a user-defined constant, α_v is the vapor volume fraction and p_∞ is the freestream pressure. The function $\text{avg}(a,b)$ is one of the TVD-type limiter. In this study the Minmod limiter is used in the computations involving the homogeneous equilibrium phase model while a Van Leer type limiter is used in all other computations.

$$\text{avg}(a,b) = \frac{1}{2}[\text{sign}(1.0,a) + \text{sign}(1.0,b)]\min(|a|,|b|) \tag{3.3.4}$$

The Van Leer type limiter used in this investigation has the following form:

$$\text{avg}(a,b) = \frac{1}{2}\left[\text{sign}\left(1.0, \frac{a+b}{2}\right) + \text{sign}(1.0, 2c)\right]\min\left(\frac{|a+b|}{2}, 2|c|\right) \tag{3.3.5}$$

where the parameter c is given as:

$$c = \frac{1}{2}[\text{sign}(1.0,a) + \text{sign}(1.0,b)]\min(|a|,|b|) \tag{3.3.6}$$

3.4 TIME INTEGRATION

The Navier-Stokes equations are solved using a cell-centered, generalized coordinate finite volume discretization. The discrete representation of the governing equations can be expressed as

$$\frac{\partial \mathbf{U}_{i,j,k}}{\partial t} = -\mathbf{R}_{i,j,k} \tag{3.4.1}$$

where $\mathbf{R}_{i,j,k}$ is the residual vector at grid point (i, j, k) expressed as:

$$\begin{aligned}\mathbf{R}_{i,j,k} = &\frac{(\mathbf{E}-\mathbf{E}_\mathbf{v})_{i+1/2,j,k} - (\mathbf{E}-\mathbf{E}_\mathbf{v})_{i-1/2,j,k}}{\Delta\xi} + \frac{(\mathbf{F}-\mathbf{F}_\mathbf{v})_{i,j+1/2,k} - (\mathbf{F}-\mathbf{F}_\mathbf{v})_{i,j-1/2,k}}{\Delta\eta} \\ &+ \frac{(\mathbf{G}-\mathbf{G}_\mathbf{v})_{i,j,k+1/2} - (\mathbf{G}-\mathbf{G}_\mathbf{v})_{i,j,k-1/2}}{\Delta\zeta} - \mathbf{S}_{i,j,k} = \mathbf{R}_{flux} - \mathbf{S}_{i,j,k}\end{aligned} \tag{3.4.2}$$

The governing equations are approximated using a backward Euler linearization in time, where the residual vector $\mathbf{R}_{i,j,k}$ is a function of the vector of primitive variables $\mathbf{V}_{i,j,k}$, yielding the following expression:

$$\begin{aligned}&\left[\frac{\mathbf{P}}{\Delta t} + A - \frac{\partial \mathbf{S}}{\partial \mathbf{V}}\right]^n_{i,j,k} \Delta\mathbf{V}^{n+1}_{i,j,k} + B^n_{i,j,k}\Delta\mathbf{V}^{n+1}_{i-1,j,k} + C^n_{i,j,k}\Delta\mathbf{V}^{n+1}_{i+1,j,k} \\ &+ D^n_{i,j,k}\Delta\mathbf{V}^{n+1}_{i,j-1,k} + E^n_{i,j,k}\Delta\mathbf{V}^{n+1}_{i,j+1,k} + F^n_{i,j,k}\Delta\mathbf{V}^{n+1}_{i,j,k-1} + G^n_{i,j,k}\Delta\mathbf{V}^{n+1}_{i,j,k+1} \\ &= -\mathbf{R}^n_{i,j,k}\end{aligned} \tag{3.4.3}$$

where $\Delta\mathbf{V}^{n+1} = \mathbf{V}^{n+1} - \mathbf{V}^n$ is the vector used to update the primitive variable vector $\mathbf{V}$, the matrices $A-G$ are functions of the inviscid and viscous flux Jacobians which are constructed as outlined in Ref. [10]. The above expression can also be written as:

$$\left[\frac{\mathbf{P}}{\Delta t} + \frac{\partial \mathbf{R}_{flux}}{\partial \mathbf{V}} - \frac{\partial \mathbf{S}}{\partial \mathbf{V}}\right]^n_{i,j,k} \Delta\mathbf{V}^{n+1}_{i,j,k} = -\mathbf{R}^n_{i,j,k} \tag{3.4.4}$$

Ordered over the mesh nodes, this equation can be rewritten in the following manner

$$\mathbf{Ax} = \mathbf{B} \tag{3.4.5}$$

where

$$\mathbf{A} = \left[\frac{\mathbf{P}}{\Delta t} + \frac{\partial \mathbf{R}_{flux}}{\partial \mathbf{V}} - \frac{\partial \mathbf{S}}{\partial \mathbf{V}} \right]^n \tag{3.4.6}$$

$$\mathbf{x} = \Delta \mathbf{V}^{n+1} \tag{3.4.7}$$

$$\mathbf{B} = -\mathbf{R}^n \tag{3.4.8}$$

In this study, the above equations are solved using two different approaches. One is the incomplete LU factorization and the other is known as the planar symmetric Gauss-Seidel. Both methods seek to replace the matrix $\mathbf{A}$ with an approximation $\hat{\mathbf{A}}$ which allows for a more efficient solution of the system.

The incomplete LU (ILU) factorization [38], is defined as:

$$\mathbf{A}\Delta\mathbf{V}^{n+1} = (\mathsf{L} + \mathsf{D} + \mathsf{U})\Delta\mathbf{V}^{n+1} = -\mathbf{R}^n \tag{3.4.9}$$

where $\mathbf{A}$ is the system Jacobian matrix L, D and U are the lower triangular, diagonal and upper triangular matrices given by:

$$\mathsf{L} = B + D + F \tag{3.4.10}$$

$$\mathsf{U} = C + E + G \tag{3.4.11}$$

The elements of D are defined recursively as:

$$\mathsf{D}_{i,j,k} = \hat{\mathbf{P}}_{i,j,k} - B_{i,j,k}\hat{\mathbf{P}}_{i+1,j,k}C_{i+1,j,k} - D_{i,j,k}\hat{\mathbf{P}}_{i,j+1,k}E_{i,j+1,k} - F_{i,j,k}\hat{\mathbf{P}}_{i,j,k+1}G_{i,j,k+1} \qquad \textbf{(3.4.12)}$$

where $\hat{\mathbf{P}}$ is defined as

$$\hat{\mathbf{P}} = \left[\frac{\mathbf{P}}{\Delta t} + A - \frac{\partial \mathbf{S}}{\partial \mathbf{V}}\right] \qquad \textbf{(3.4.13)}$$

The matrix $\mathbf{A}$ is approximated by the following matrix $\hat{\mathbf{A}}_{ILU}$:

$$\hat{\mathbf{A}}_{ILU} = (\mathsf{L} + \mathsf{D})\mathsf{D}^{-1}(\mathsf{D} + \mathsf{U}) \qquad \textbf{(3.4.14)}$$

In order to advance the solution in time, the nonlinear ILU method is implemented in two steps, a forward and a backward step in ξ-direction given respectively:

$$\Delta\mathbf{V}_i^{n+\frac{1}{2}} = (\mathsf{D}_i{}^n)^{-1}\left[-\mathbf{R}_i^n - \mathsf{U}_i{}^n\Delta\mathbf{V}_{i+1}^{n+\frac{1}{2}}\right] \qquad \textbf{(3.4.15)}$$

$$\Delta\mathbf{V}_i^{n+1} = \Delta\mathbf{V}_i^{n+\frac{1}{2}} - (\mathsf{D}_i{}^n)^{-1}\mathsf{L}_i{}^n\Delta\mathbf{V}_{i-1}^{n+1} \qquad \textbf{(3.4.16)}$$

The planar symmetric Gauss-Seidel solver approximates the matrix $\mathbf{A}$ in the following manner:

$$\hat{\mathbf{A}}_{PGS} = (\mathsf{L} + \mathsf{D})\mathsf{D}^{-1}(\mathsf{D} + \mathsf{U}) \qquad \textbf{(3.4.17)}$$

where L, D and U are the lower triangular, diagonal and upper triangular matrices defined as:

$$\mathsf{L} = B \tag{3.4.18}$$

$$\mathsf{U} = C \tag{3.4.19}$$

$$\mathsf{D} = \hat{\mathbf{P}} + D + E + F + G \tag{3.4.20}$$

where $\hat{\mathbf{P}}$ is defined as

$$\hat{\mathbf{P}} = \left[\frac{\mathbf{P}}{\Delta t} + A - \frac{\partial \mathbf{S}}{\partial \mathbf{V}} \right] \tag{3.4.21}$$

The linear system is solved in two steps, a forward and a backward step in the ξ-direction:

$$\Delta \mathbf{V}_i^{n+\frac{1}{2}} = \left(\mathsf{D}_i^{\,n}\right)^{-1} \left[-\mathbf{R}_i^n - \mathsf{L}_i^{\,n} \Delta \mathbf{V}_{i-1}^{n+\frac{1}{2}} \right] \tag{3.4.22}$$

$$\Delta \mathbf{V}_i^{n+1} = \Delta \mathbf{V}_i^{n+\frac{1}{2}} - \left(\mathsf{D}_i^{\,n}\right)^{-1} \mathsf{U}_i^{\,n} \Delta \mathbf{V}_{i+1}^{n+1} \tag{3.4.23}$$

The time step, Δt is defined as:

$$\frac{\mathsf{V}_{i,j,k}}{\Delta t} = \frac{\left[\frac{|\nabla \xi|}{J}\left(|U_c| + a\right) + \frac{|\nabla \eta|}{J}\left(|V_c| + a\right) + \frac{|\nabla \zeta|}{J}\left(|W_c| + a\right) \right]}{CFL} \tag{3.4.24}$$

where $\left(|U_c| + a,\ |V_c| + a,\ |W_c| + a\right)$ are the local eigenvalues of the system.

4 IMPLEMENTATION

4.1 EXPERIMENTAL PROCEDURE

All experimental data was obtained from experiments performed at Wright Patterson Air Force Labs over a period of years. Two groups were responsible for the experiments: Wu, et al. [40, 41], and Lin, et al. [18]. The experimental procedure followed by these groups is outlined in this section.

Pure ethylene or an ethylene/methane mixture was injected vertically downward into a high-pressure chamber filled with room-temperature nitrogen. The apparatus consists of a fuel tank, a heating/chilling unit, a heat exchanger, a solenoid valve, a nozzle, and the injection chamber. Initially temperature and pressure of the test fluid are pre-set inside the fuel tank, which has an internal volume of 15 liters. The test fluid is then introduced into the heat exchanger to gradually reach the selected temperature. A heating/chilling unit controls the temperature of the ethylene glycol which flows inside the annular passage of the heat exchanger and is used as the heat exchange medium to control the temperature of the test fluid.

Once the test fluid reaches the desired temperature and pressure, a solenoid valve with a response time of 150 ms is opened for about 5-10 s to charge the test fluid into the test chamber. Due to the transient behavior of the jet, no measurements were made during the first 2 seconds of injection. Before injection is begun, the test chamber is flushed with nitrogen twice to remove oxygen and then filled with nitrogen at a desired back pressure for injection. The chamber has an internal diameter of 0.2 m and a height

of 0.94 m, resulting in an internal volume of about 0.12 m^3. There are three rectangular quartz windows for optical access and one round port for instrumentation.

A round nozzle with an exit diameter of 1.0 mm (or 0.5 mm) was used in the present study. The nozzle passage begins with a 1.6 mm radius entry, which is rounded to avoid flow separation. The entry is followed by a 1-degree converging section to ensure that the choke point can only occur at the nozzle exit. The ratio of passage length to exit diameter was maintained at 4.

The experiments of Wu, et al. used long-exposure shadowgraphs to identify the thermodynamic phase of the injectant, as well as schlieren photographs to resolve shock patterns and jet boundaries. The shadowgraphs were captured by a 35-mm Nikon camera with a shutter speed of 1/30 s and an f-number of 4.5. The schlieren photographs were taken by a Speed Graphic camera, loaded with a Polaroid type black and white film with a shutter speed of 1/125 s. The fuel mass flow rate was measured using a Coriolis-type mass flow meter with an uncertainty of less than 1%. Fuel temperatures were measured with thermocouples and controlled by flowing ethylene glycol outside the fuel pipe with an uncertainty of less than 1 K. Pressure transducers were used for pressure measurements inside the high-pressure chamber and fuel tank.

The experiments of Lin, et al. study the structure of supercritical fluid inside an injector using a transparent injector with exchangeable internal blocks (fabricated for the present study). One internal configuration has a 6.4x1.0 mm flow passage, followed by a 10-degree converging section, and then by a 1.0-mm square passage with a length of 4.0 mm. Two quartz windows were fitted into the transparent injector to provide

visualization of the fluid structure inside the injector. For the measurement of pressure profiles inside the transparent injector, one quartz block was replaced by a metal block with pressure taps along the injector axis over the desired spatial distribution. Visualization of the flow structure was accomplished with shadowgraph and direct-lighting techniques, respectively. Pressure profiles inside the transparent injector were measured using high-speed pressure transducers. A 45-200 mm zoom lens and a CCD video camera were used to capture the images. The images were either stored inside a computer using a frame grabber or recorded on videotape for later analysis. A Coriolis-type mass flow meter with a measurement range of 2.0-37.8 g/s and an uncertainty of less than 1% was used in the present study to measure the mass flow rate. K-type thermocouples were used for temperature measurement in this study. They were calibrated with ice bath before each measurement and have an uncertainty of less than 0.5 K. Seven pressure transducers were used for pressure measurements inside the high-pressure chamber, fuel tank, and various locations of the fuel line. The pressure profile along the injector axis was measured using a pressure scanner (Scanivalve, Model 3207). All pressure transducers and the pressure scanner were calibrated using a digital pressure gauge (Mensor, Model 2107) and have an uncertainty of less than 0.5%.

4.2 COMPUTATIONAL GEOMETRY

In this study three different grid arrangements were generated. Two of these correspond with the axisymmetric configurations tested in Refs. [18], [40], and [41],

while the other was used for the three-dimensional and two-dimensional calculations inside the transparent injector.

Figure 4.1 shows the grid arrangement for the 1.0 mm nozzle diameter round-hole injector configuration used in Refs [18] and [41]. The grid is divided into 4 blocks: block 1 contains 41x65 mesh points; block 2 contains 65x33 mesh points, block 3 contains 109x65 mesh points, and block 4 contains 109x33 mesh points, giving a total number of interior grid cells of 14976. Grid-refinement studies were performed for selected calculations in a grid consisting of four times as many points in each block, resulting in a total number of 59904 interior grid cells.

Figure 4.2 shows X-Y and X-Z views of the three-dimensional grid used to simulate some of the transparent-injector experiments performed as part of this study. The transparent injector consists of a 10-degree contraction followed by a 4 mm straight nozzle with a 1 mm square exit cross section. Only the flow in one quarter of the geometry is actually simulated, as bi-lateral symmetry is assumed. A separate grid block was placed outside the domain to allow for the expansion of the exiting sonic flow, but no attempt was made to resolve the three-dimensional jet structure external to the nozzle. The 205x65x65 domain (835,584 interior grid cells) is divided into eight blocks (four blocks on either side of the X-Y plane). Each block is assigned to a different processor, and calculations are parallelized with Message-Passing Interface (MPI) [3, 32]. Grid-refinement studies were conducted in two dimensions using meshes containing 205x33, 205x65, and 409x129 points.

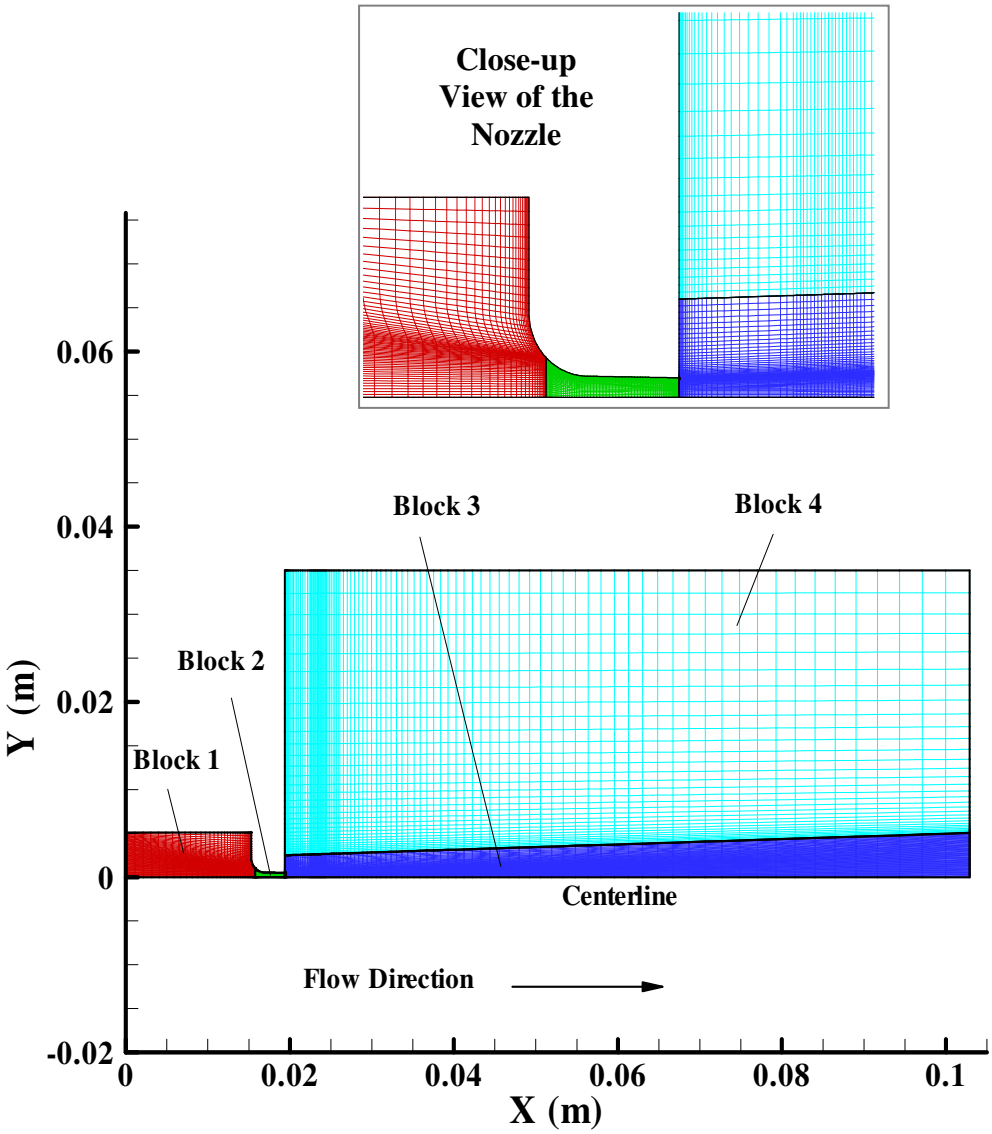

Figure 4.1: Grid for Axisymmetric Nozzle Simulations

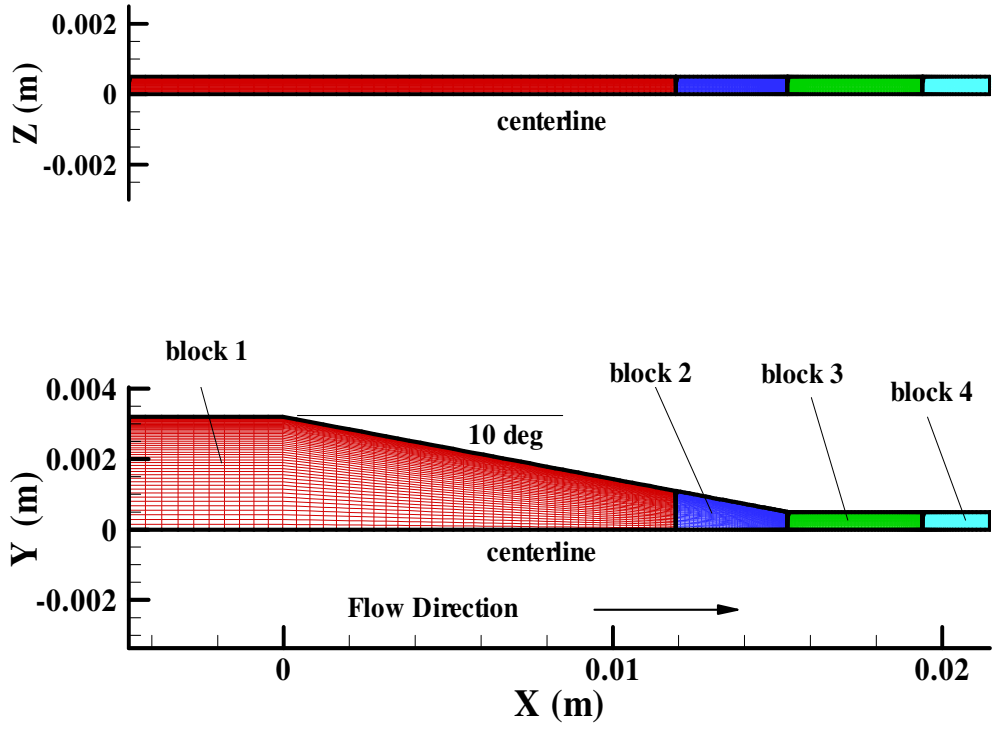

Figure 4.2: Grid for Three-dimensional Nozzle Simulations

4.3 BOUNDARY CONDITIONS

For the axisymmetric grid in Figure 4.1, the boundary condition at the inflow boundary of block 1 sets the total pressure and total enthalpy equal to their reservoir values and extrapolates the axial velocity from the interior. The outflow boundary condition for blocks 3 and 4 assigns the static pressure to the chamber value and extrapolates the remaining primitive variables. A simple extrapolation boundary condition is used for the top of block 4. Part of the inflow boundary of blocks 3 and 4 is specified as a solid surface corresponding to the end of the actual nozzle apparatus. No-slip, adiabatic wall conditions are enforced on this surface as well as on the upper

boundaries of blocks 1, 2, and 3. Symmetry about the centerline is also enforced. A co-flow velocity of 10 m/s is specified along the remaining part of the inflow boundary of block 4. This was found to be necessary to ensure a steady-state solution for most conditions. Turbulence inflow parameters correspond to an assumed turbulence intensity of 5%, referenced to an inflow velocity of 2 m/s. The radius of block 1 is used as a characteristic length for completing the specification of the eddy viscosity.

The boundary condition for the three-dimensional grid (Figure 4.2) at the inflow boundary of block 1 fixes the total pressure and total enthalpy to their reservoir values and extrapolates the axial velocity from the interior. The supersonic boundary condition, which extrapolates all primitive variables from the interior, is applied to the outflow boundary of block 4. No-slip, adiabatic wall conditions are enforced on all wall surfaces as well as on the upper boundaries of blocks 1, 2, and 3. A simple extrapolation boundary condition is imposed on the upper wall of block 4 to allow the expansion of the exiting supersonic flow. A symmetry boundary condition is imposed about the centerline and both sides of the geometry.

5 RESULTS AND DISCUSSION

The following sections present the results obtained from the computational model for different injection cases. This section is divided in two main parts, pure ethylene injection and ethylene/methane mixture injection.

5.1 PURE ETHYLENE INJECTION

The cases involving pure ethylene injection differ mainly by nozzle geometry, turbulence closure, and two-phase modeling. These cases are depicted in Table 5.1

Table 5.1: List of Cases for Pure Ethylene Injection

Case #	Geommetry	Two-Phase Model	Turbulence Closure	Database
1	axisymmetric	Homogeneous Equilibrium	1-equation	Wu, et al.
2	axisymmetric	Homogeneous Equilibrium	1-equation	Lin, et al.
3	3-D transparent	Homogeneous Equilibrium	2-equation	Lin, et al.
4	3-D transparent	Homogeneous Nucleation/growth	2-equation	Lin, et al.

5.1.1 Case 1

The following test cases involve injection of pure ethylene through round-hole nozzle configurations with exit diameters of 1.0 mm and 0.5 mm. The simulation model uses the homogeneous equilibrium representation of the two-phase flow and the one-equation turbulence model. These cases corresponds to experiments by Wu, et al. [40, 41], which focused on determining the effects of injectant temperature and chamber pressure on the injection process.

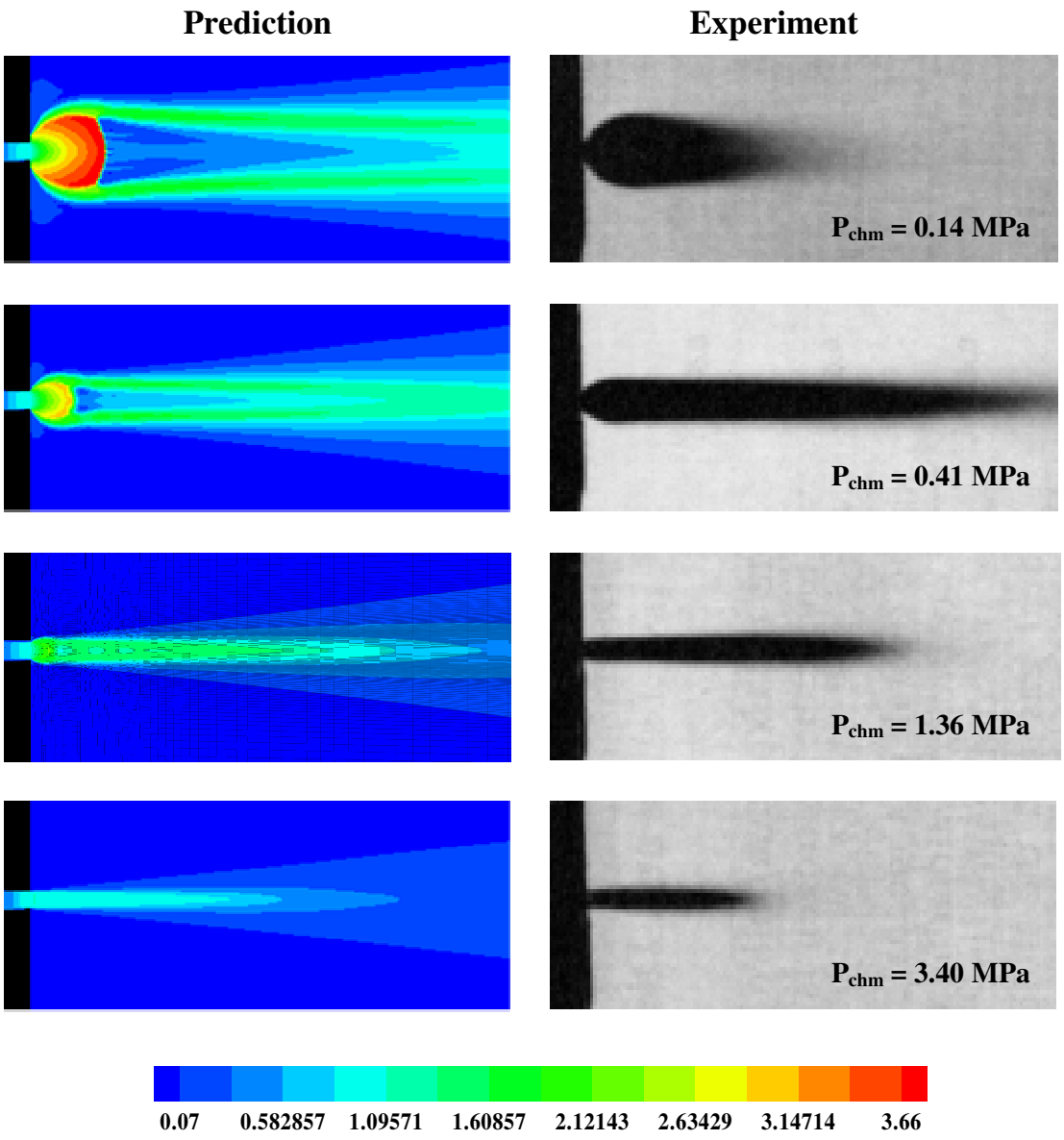

Figure 5.1: Effect of Chamber Pressure on Mach Number

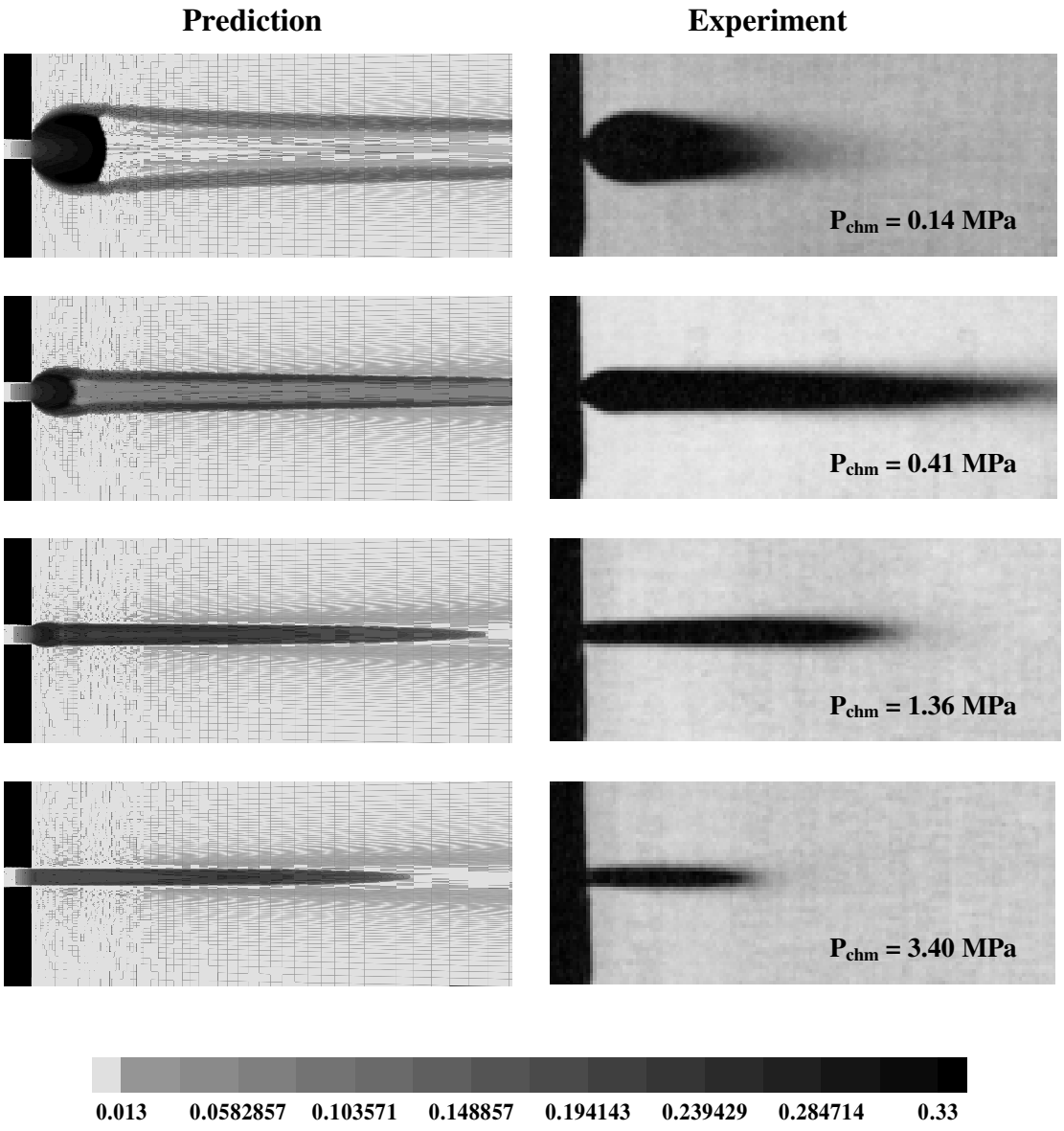

Figure 5.2: Effect of Chamber Pressure on Liquid Mass Fraction

Figure 5.1 and Figure 5.2 illustrate the effect of varying the chamber pressure on the jet structure. The reservoir temperature and pressure are set to 293 K and 5.8 MPa, respectively, and the 1 mm nozzle-diameter grid configuration is used. Figure 5.1 plots Mach number contours which indicate the general flow structure, while Figure 5.2 plots

liquid-phase volume fraction contours (ranging between 0 and 0.05) which illustrate the degree of condensation present. The jets are shown reflected about the centerline for clarity, and the figures are scaled to correspond with shadowgraph images from Ref. [40]. For these conditions, the opacity in the shadowgraph images corresponds to the combination of the presence of a condensed phase and general curvature effects in the bulk density field (especially at the higher chamber pressures). For the lowest chamber pressure of 0.14 MPa, the initial rapid expansion of the fluid causes an abrupt shift to mostly gaseous flow. The rapid expansion results in a dome-shaped jet boundary near the nozzle and is terminated by a Mach disk. Experimental results do not indicate the presence of the Mach disk due to the masking effects of fuel condensation. At this condition, the liquid content in the core of the jet is greatly reduced downstream of the Mach disk, resulting in the "feathered" appearance of the jet in Figure 5.2. For a slightly higher chamber pressure of 0.41 MPa a weaker Mach disk is present, whereas for a chamber pressure of 1.36 MPa, the Mach disk is replaced by a sequence of expansion fan/oblique shock-wave interactions. At the highest chamber pressure of 3.4 MPa, the nozzle flow expands very little external to the nozzle.

Table 5.2: Mass Flow Rates versus Chamber Pressure (1.0 mm Diameter Nozzle)

Chamber Pressure (Mpa)	Mass Flow Rate (g/s)	Liquid Mass Flow Rate (g/s)
3.4	12.91	2.239
1.36	13.02	2.379
0.41	13.05	2.353
0.14	13.03	2.334

The computed mass flow rate and condensed liquid mass flow rate are shown in Table 5.2 as a function of chamber pressure. At the exit of the nozzle, two-phase flow is predicted for all chamber pressures. The nearly constant mass flow rates at the lower chamber pressures of .14, 0.41, and 1.36 MPa indicate choked flow. These results are in conformity to the experimental data, with minor deviations observed for the liquid mass flow rate at the highest chamber pressure.

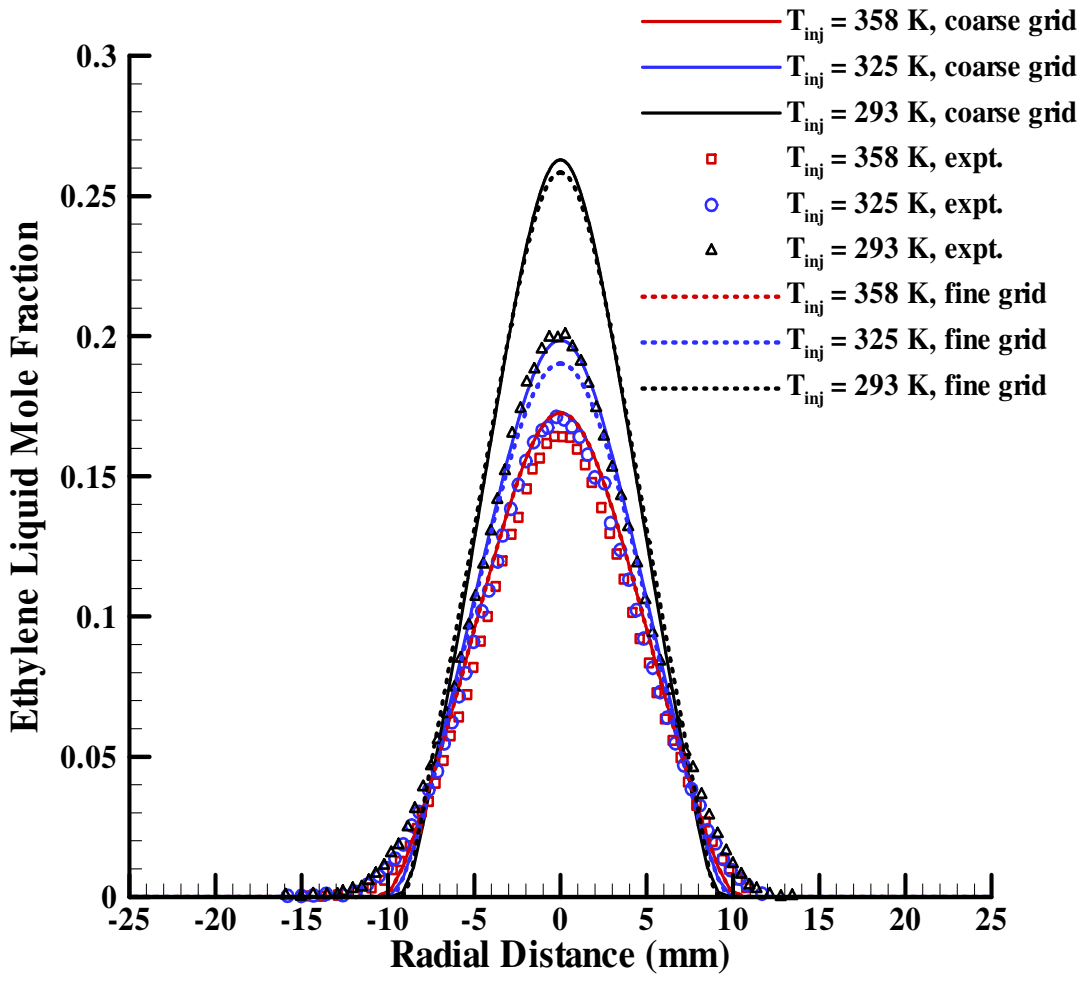

Figure 5.3: Ethylene Liquid Mole Fraction Distributions at X/D=112

It can be observed from the liquid volume fraction contours that the extent of condensed-phase penetration is generally larger than indicated in the experimental data. This behavior might be a possible consequence of the homogeneous equilibrium assumption. Otherwise, the predicted jet structure for each case is in good qualitative agreement with the shadowgraph images.

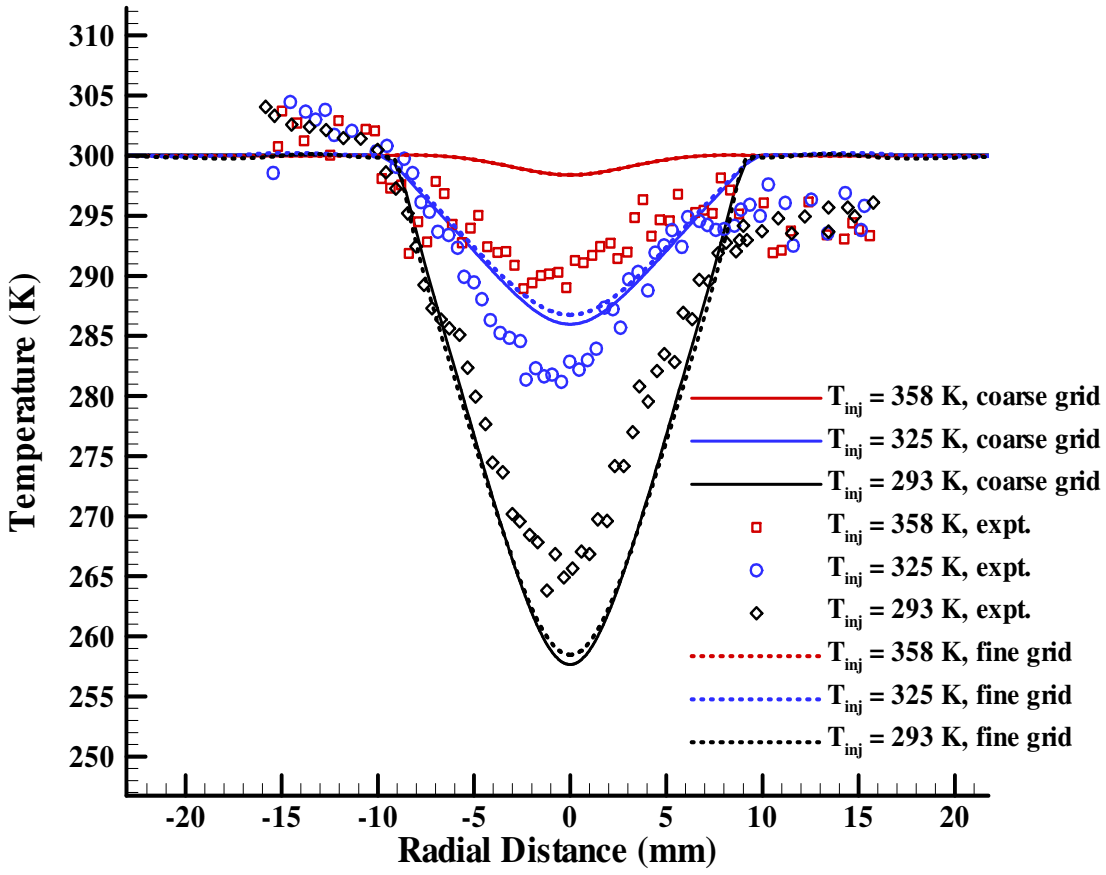

Figure 5.4: Temperature Distributions at X/D = 112

Figure 5.3 and Figure 5.4 show radial ethylene mole fraction and temperature profiles at X/D = 112 for different injection temperatures and grid resolutions for the 0.5 mm nozzle exit diameter geometry. These cases serve to test the ability of the numerical

schemes to predict the far-field mixing of the ethylene jet with entrained nitrogen and as such, are as much of a test of the turbulence model as a test of the thermodynamic state description. Radial profiles of liquid ethylene mole fraction are presented in Figure 5.3. The lateral spreading of the jet at this location is reasonably well-predicted; however the peak (centerline) values of the mole fraction at the lower temperatures are larger than the measured values. Only at the highest injectant temperature of 358 K (a nearly gas-phase expansion) are the predictions in good agreement with the experimental data. The results at lower injectant temperatures seem to imply insufficient mixing of the higher-momentum ethylene jet with the surrounding nitrogen gas. Grid refinement provides some slight improvements at the lowest temperature of 293 K but does not significantly affect predictions at the higher temperatures. In contrast, radial temperature profiles shown in Figure 5.4 indicate reasonably good agreement with experimental data at injectant temperatures of 293 K and 325 K. The experimental results are not symmetric as there is a ten-degree difference between the measured far-field values on either side of the jet. The calculations under-predict the measured temperature at the centerline for the lowest injection temperature, and again, the effects of grid refinement are not significant. The use of a 10 m/s co-flow to model air entrainment probably affects these results to some degree. Lower values for the co-flow velocity led to an unacceptable level of unsteadiness in the jet shear layer, particularly on the fine grid.

5.1.2 Case 2

The subsequent test cases were computed for different injectant temperatures in the vicinity of the critical point and involve the injection of pure ethylene through the

round-hole nozzle configuration with an exit diameter of 1.0 mm. The numerical simulation is based on the homogeneous equilibrium model, and the one-equation turbulence model is again used. The conditions considered in these cases are based on unpublished data generated from the experiments of Lin, et al.

Figure 5.5 and Figure 5.6 compare predictions of the jet structure with shadowgraph images for a selection of injectant temperatures. The injectant pressure varies from 6.19 MPa to 6.25 MPa, and the higher resolution grid was used in these calculations. As in Figure 5.1 and Figure 5.2, Mach number contours and flood contours of liquid ethylene volume fraction are used to provide indications of the Mach-disk structure, the jet spreading rate, and the amount of condensation present. Good visual agreement in the positioning of the Mach disk, the initial spreading rate of the jet, and narrowing of the condensation plume downstream of the Mach disk is indicated for the higher temperatures of 311.3 K and 300.1 K. At the highest temperature of 311.3 K, there is little experimental evidence of the condensed phase persisting beyond the nozzle exit, though some liquid is predicted to be entrained into the shear layer and carried around the Mach disk. As the temperature is lowered, the amount of condensation present increases, leading to the complete masking of the internal jet structure at T = 294.8 degrees. The initial spreading rate is well-predicted at this temperature, though the amount of liquid-droplet entrainment into the outer edges of the shear layer appears to be under-predicted. The trend of increasing amount of liquid in the jet with decreasing injectant temperatures is maintained for the lower injectant temperatures of 284.5 K and 280.6 K. Again, the initial spreading rate appears to be captured reasonably well, but the

calculated extent of condensed-phase penetration towards the outer parts of the shear layer is under-predicted. This effect is particularly noticeable for the lowest temperature, where the calculation predicts a jet that is much less broad in the radial direction than is indicated in the image. As the actual Mach disk structure cannot be seen at this temperature, it is uncertain whether the broadening effect is due to a much larger Mach disk or simply to the entrainment of droplets into the shear layer that separates the free-jet expansion zone from the quiescent gas. Similar to the observations in Refs. [18] and [40], the position of the Mach disk along the centerline is observed to be relatively independent of the injectant temperature; however, the diameter of the Mach disk increases with decreasing injectant temperature.

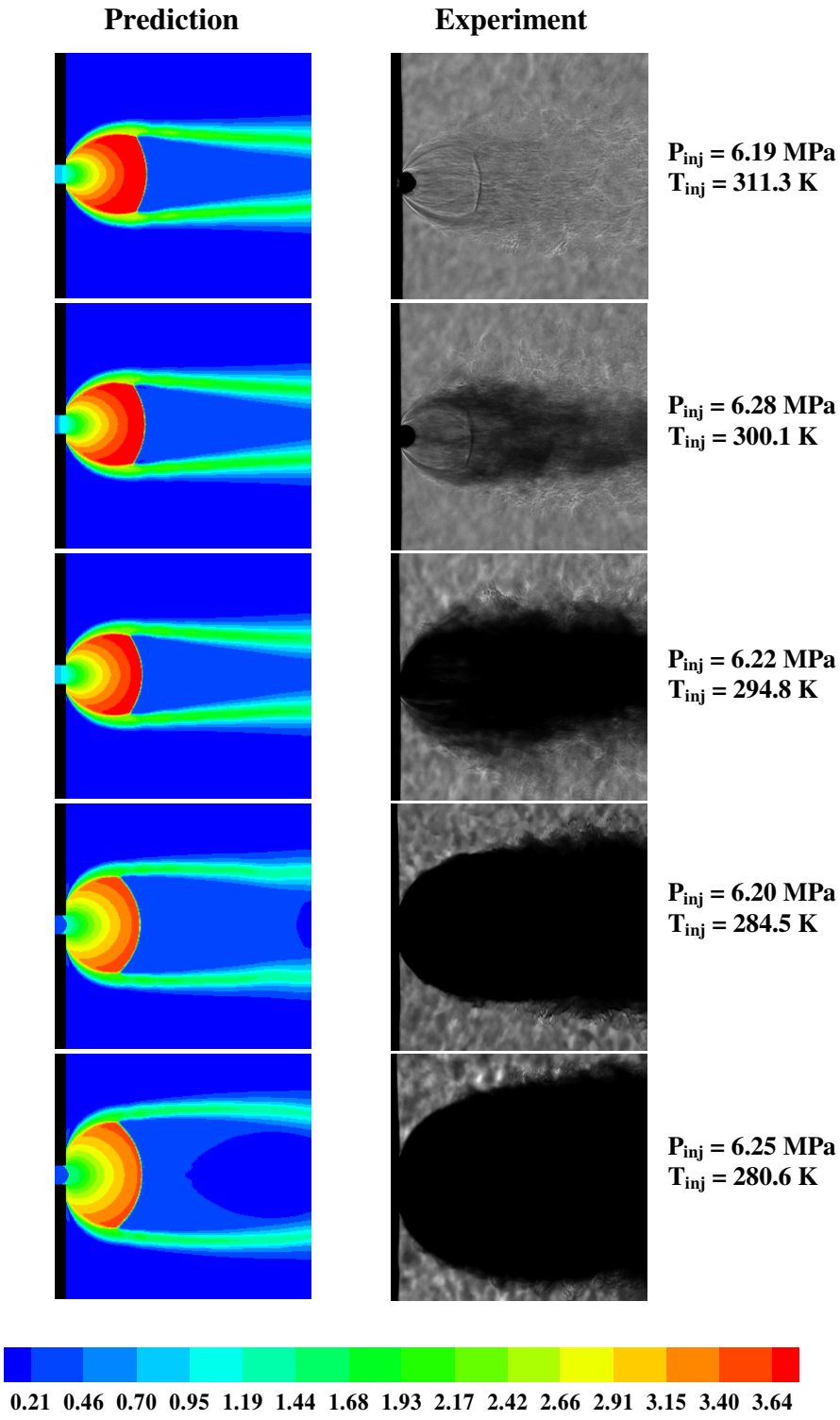

Figure 5.5: Effect of Injectant Temperature on Mach Number

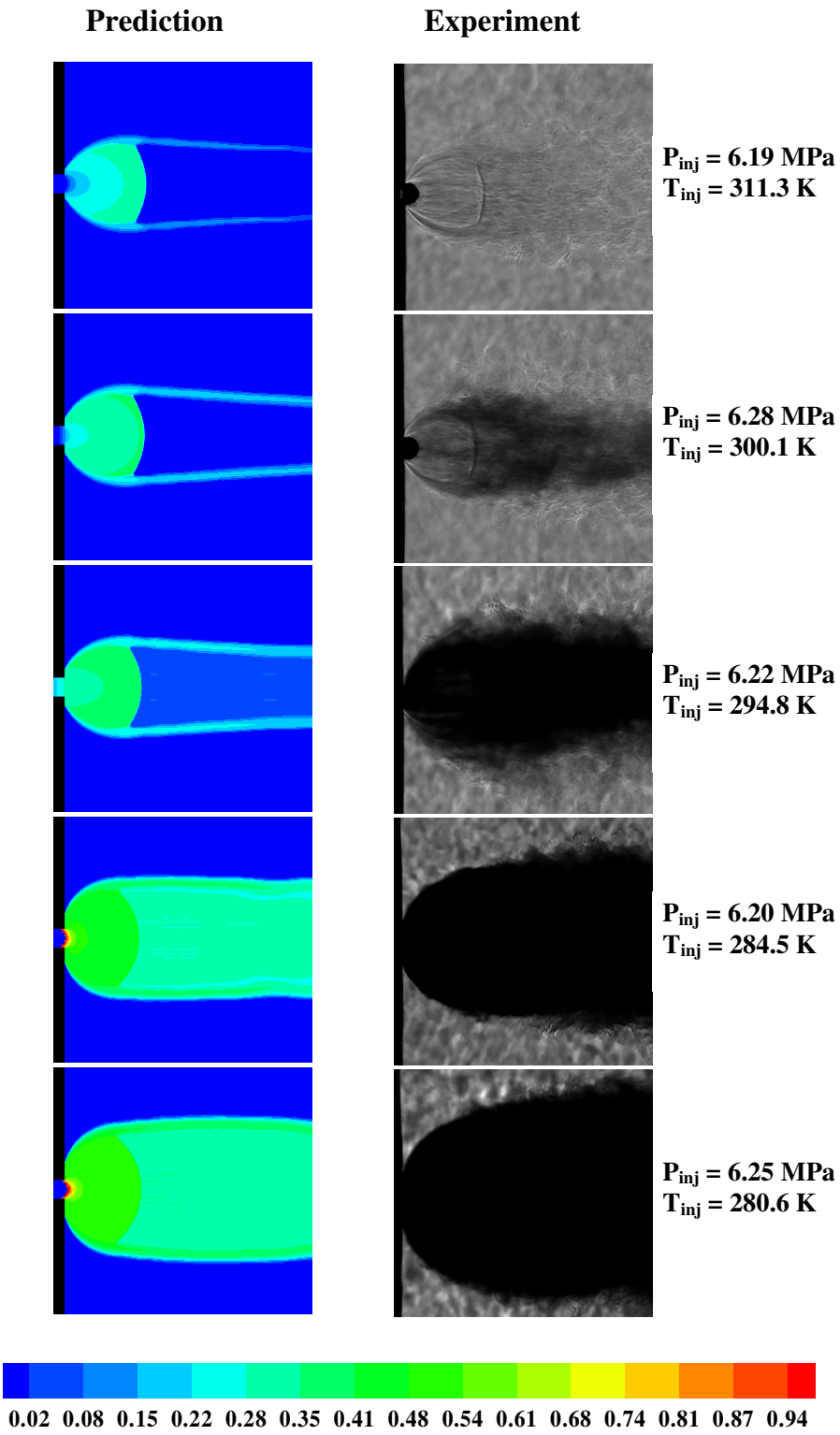

Figure 5.6: Effect of Injectant Temperature on Liquid Mass Fraction

Table 5.3: Predicted and Measured Mass Flow Rates versus Injectant Temperature

P_{inj} (MPa)	T_{inj} (K)	Mass Flow Rate (g/s) (experiment)	Mass Flow Rate (g/s) (coarse grid)	Mass Flow Rate (g/s) (fine grid)
6.19	311.3	13.10	13.04	13.23
6.28	300.1	15.31	14.56	14.76
6.22	294.8	17.88	15.29	15.47
6.20	284.5	23.33	21.8	22.2
6.25	280.6	30.28	25.38	25.86

Table 5.3 presents mass flow rate predictions versus experimental data. Deviations become more significant at the lower temperatures, which are nearer the critical point. The under-prediction of the mass flow rate at the lowest temperature of 280.6 K, as well as the under-prediction of the broadening of the jet in Figure 5.5, would indicate that the actual density of the fluid upstream of the nozzle entrance region is higher than predicted by the Peng-Robinson equation of state. This could imply that the temperature just upstream of the entrance to the nozzle is actually lower than the measured value of 280.6. Doubling the number of mesh points slightly improves agreement with the measured values.

5.1.3 Cases 3 and 4

In Ref. [18], Lin, et al. report initial results for supercritical methane/ethylene jet expansion from a selection of three-dimensional, transparent injector configurations. The use of nominally rectangular, rather than circular, injector cross-sections allows for shadowgraph imaging of the onset of condensation within the nozzle. The numerical simulations for Cases 3 and 4 seek to confirm the onset of condensation of pure ethylene

injection observed in the experiments of Lin, et al. The numerical model uses the homogeneous equilibrium model (Case 3) and the aerosol transport model (Case 4) to account for two-phase flow phenomena. Turbulence closure is achieved by Menter's two-equation turbulence model.

Figure 5.7 (case 3) compares direct-lighting imaging data for pure-ethylene injection with liquid-phase volume fraction predictions for injectant temperatures of 309.2 K, 289.0 K, and 281.5 K and a nominal injectant pressure of around 5.45 MPa. Darker contours indicate the formation of a condensed phase at the entrance to the straight nozzle section for injectant temperatures of 289.0 K, 283.9 K, and 281.5 K. At the injectant temperature of 309.2 K, a condensed phase is not formed within the nozzle, which is in good agreement with imaging results, however, some condensation is evident in the predictions of the flow within the simulated expansion region external to the nozzle. The relative amount of condensation is indicated by an increase in gray-scale contrast, and again, good visual agreement with the direct-lighting images is indicated for all injectant temperatures.

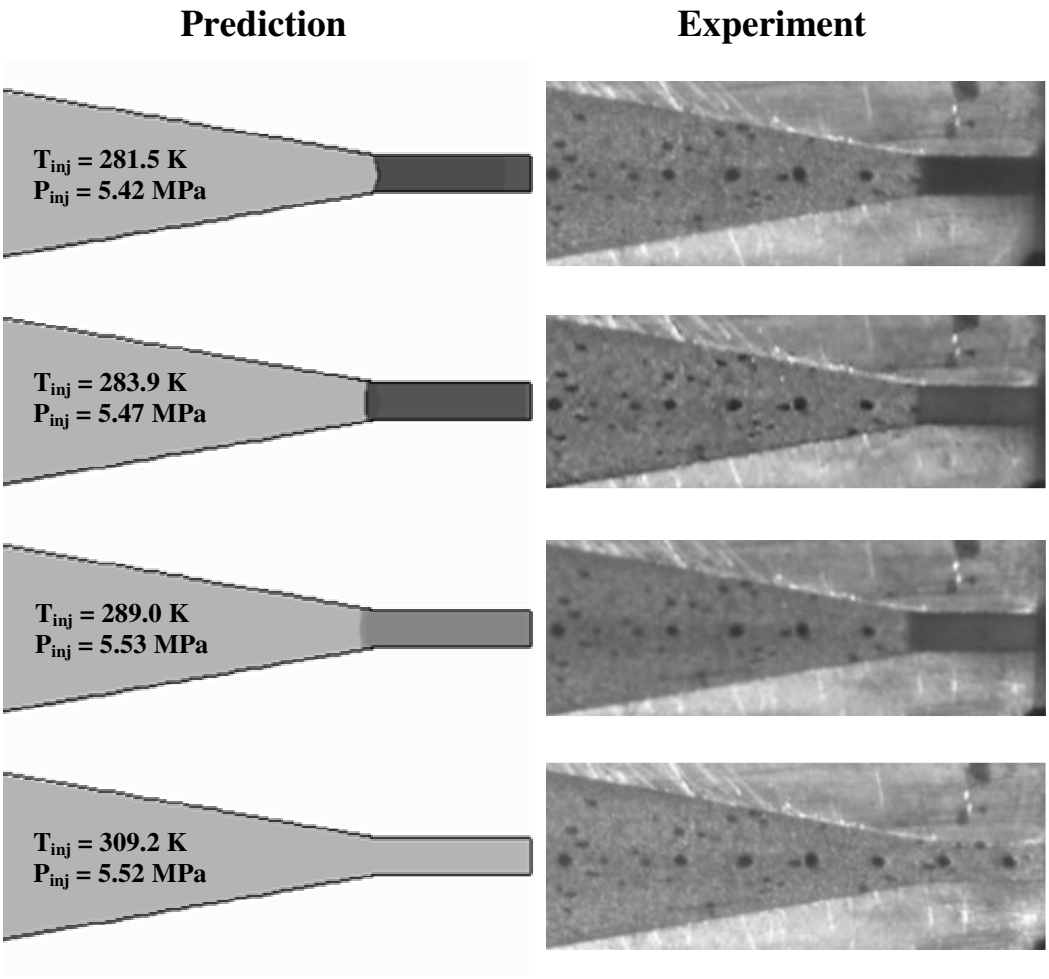

Figure 5.7: Effect of Injectant Temperature on Onset of Condensation in Transparent Injector

In order to gain further insight into the formation of a condensed phase within the nozzle, a plot of pressure versus mixture density along the centerline for the different injectant temperatures was generated (Figure 5.8). These plots illustrate the equilibrium thermodynamic process path followed during a nearly isentropic expansion of the fluid from the nozzle reservoir conditions to the free-jet expansion zone. The vapor dome and spinodal curves provided by the Peng-Robinson equation of state are also shown in

Figure 5.8. The process path indicates that the saturated vapor line is crossed for injectant temperature of 309.2 K and 289.9 K, while the saturated liquid line is crossed for injectant temperatures of 283.9 K and 281.5 K. For the higher temperatures, the process path for the two-phase mixture is contained within the metastable vapor region, implying that the phase transition involves the formation of a dispersed liquid phase from a supersaturated vapor. As the process path does not cross the vapor spinodal curve, it is probable that homogeneous nucleation theory could be used to model this phase transition as a relaxation process through a sequence of metastable states. The situation is different for injectant temperatures of 283.9 K and 281.5 K. Here, the process path enters the metastable liquid region then progresses into the unstable region, where the equation of state (under non-equilibrium conditions) does not give a physical description of the flow. This process could be viewed as the formation of a dispersed vapor (bubble) phase from a supersaturated liquid and could be regarded as a cavitation event rather than a condensation event. Homogeneous nucleation theory could be used to describe the initial stages of the phase transition that occur within the metastable liquid region, but if the rate of vapor mass generation is not fast enough to force the local pressure to equilibrate rapidly to the vapor pressure Figure 2.4, the process path could cross the liquid spinodal curve. When this happens, the solution of the cubic equation of state would result in one vapor density, rather than three. This implies the spontaneous, irreversible formation of a vapor phase, which would act rapidly to break up the liquid media into filaments and droplets. The rate process associated with this transition is not described by homogeneous nucleation theory. The equilibrium approach used in these

calculations implies an infinitely fast phase-transition rate and avoids this difficulty entirely. Details of the transition process itself, such as local droplet size and population, cannot be determined, however.

Figure 5.9 compares pressure distributions at all injectant temperatures with experimental data. Generally good agreement is observed, except for the highest temperature of 309.2 K. Since this case should be the least influenced by real-fluid effects, the discrepancy is somewhat surprising and is yet unexplained.

Figure 5.10 illustrates the effect of mesh refinement on two-dimensional predictions of the centerline pressure within the injector for an injectant temperature of 281.5 K. A two-dimensional mesh refinement study was conducted to reduce computational expense; the validity of this assumption may be assessed by comparing Figure 5.9 and Figure 5.10, which presents three-dimensional predictions on the 205x65x65 mesh. The pressure distributions corresponding to the 205x65 and 405x65 meshes are virtually identical.

The general trend with decreasing injectant temperature is to reduce the amount of expansion that occurs within the nozzle itself. This is consistent with the presence of more liquid content with decreasing injectant temperature, as evidenced in Figure 5.11, which shows a plot of centerline ethylene liquid volume fraction versus distance away from the nozzle exit. Reflecting observations noted above, the reservoir liquid voidage is set to one for the lowest temperatures and zero for the two highest temperatures. The appearance of a liquid phase at the highest temperature of 309.2 K is confined to the external expansion region, while in the other cases, the phase transition is initiated at the

entrance to the straight nozzle section. The decrease in liquid content as the flow proceeds toward the nozzle exit is significant at the lowest two temperatures, while the liquid content stays more constant within the nozzle for the 289.0 K case.

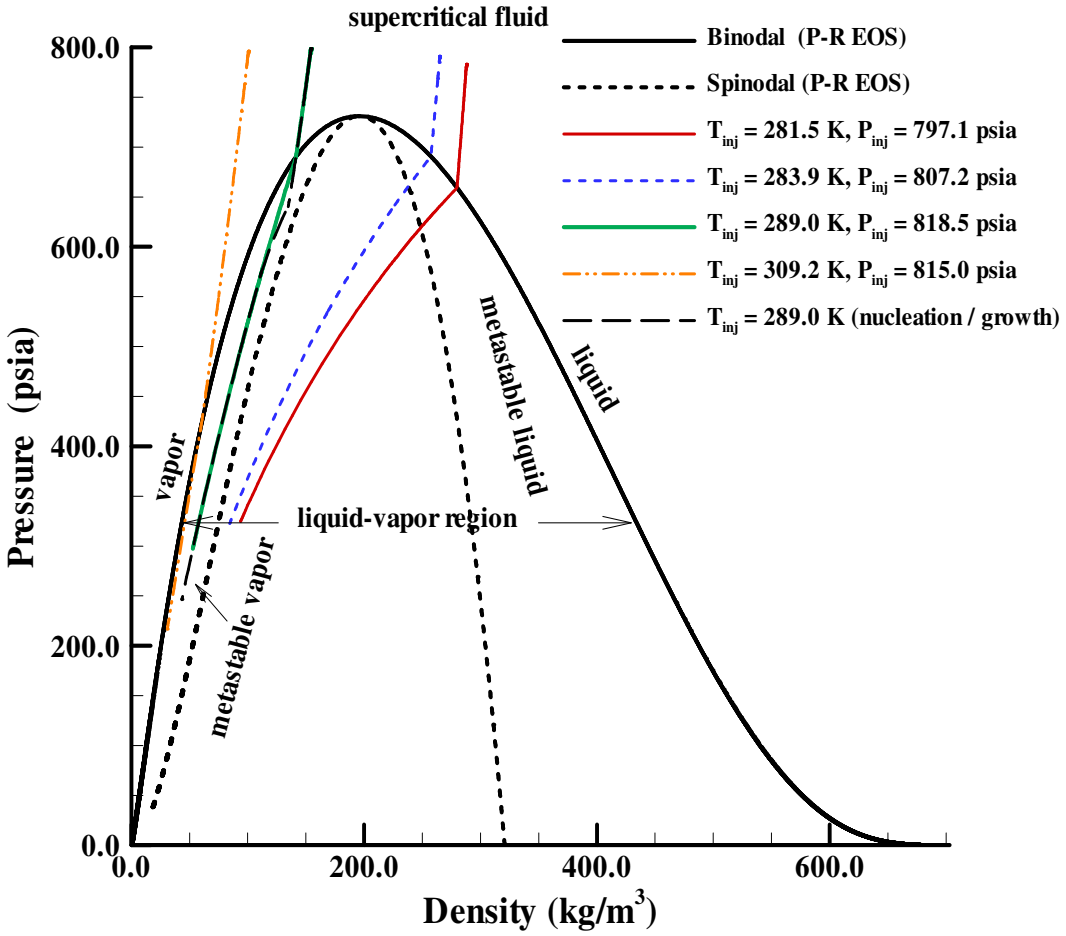

Figure 5.8: Centerline Pressure-Density Process Path for Different Injectant Temperatures

Figure 5.12 through Figure 5.15 correspond to results obtained from the nucleation/growth model (Case 4) as applied to the 289.0 K case. Figure 5.12 and Figure 5.13 compare centerline pressure and volume-fraction distributions as obtained from the

homogeneous equilibrium model and the nucleation/growth model. Pressure distributions are virtually identical except near the condensation onset region, where the nucleation/growth model results in slightly higher pressures and slightly better agreement with the experimental data. The pressure-density process path for the nucleation/growth model is also shown in Figure 5.8, where it can be seen that it follows the equilibrium distribution for much of the expansion but ventures nearer to the spinodal curve after crossing the saturated-vapor curve. Figure 5.13 show that the rate of formation of the liquid phase (in terms of its volume fraction) is less than predicted by the equilibrium model and that the overall amount of liquid produced within the nozzle is also less. Both of these trends are as expected. Figure 5.14 provides contour plots of average droplet diameter and number density within the nozzle. The liquid mass fraction distribution, not shown, is nearly homogeneous in the Y direction of the nozzle. The number density and droplet diameter distributions vary significantly near the wall. Figure 5.15 provides more detail, showing distributions obtained along the centerline and within the sidewall boundary layer. Near the wall, high strain rates result in a decrease in the modeled Kolmogorov time scale (Eq. (2.6.25)), effectively increasing the droplet coagulation rate. This results in a reduction in the droplet number density in this region, and as the volume fraction is nearly constant, the average droplet diameter increases through Eq. (2.6.31). Super-micron-sized (3.5 μm) droplets are eventually formed within the boundary layer; whereas sub-micron sized (0.3 μm) droplets are formed nearer the centerline. Such large droplets would tend to maintain their initial momentum and would vaporize more slowly upon exiting the nozzle, compared with the smaller droplets formed within the core fluid.

This would provide one explanation for the apparent presence of a significant amount of liquid content in the outer edges of the shear layer (Figure 5.2) which is not found in the equilibrium predictions.

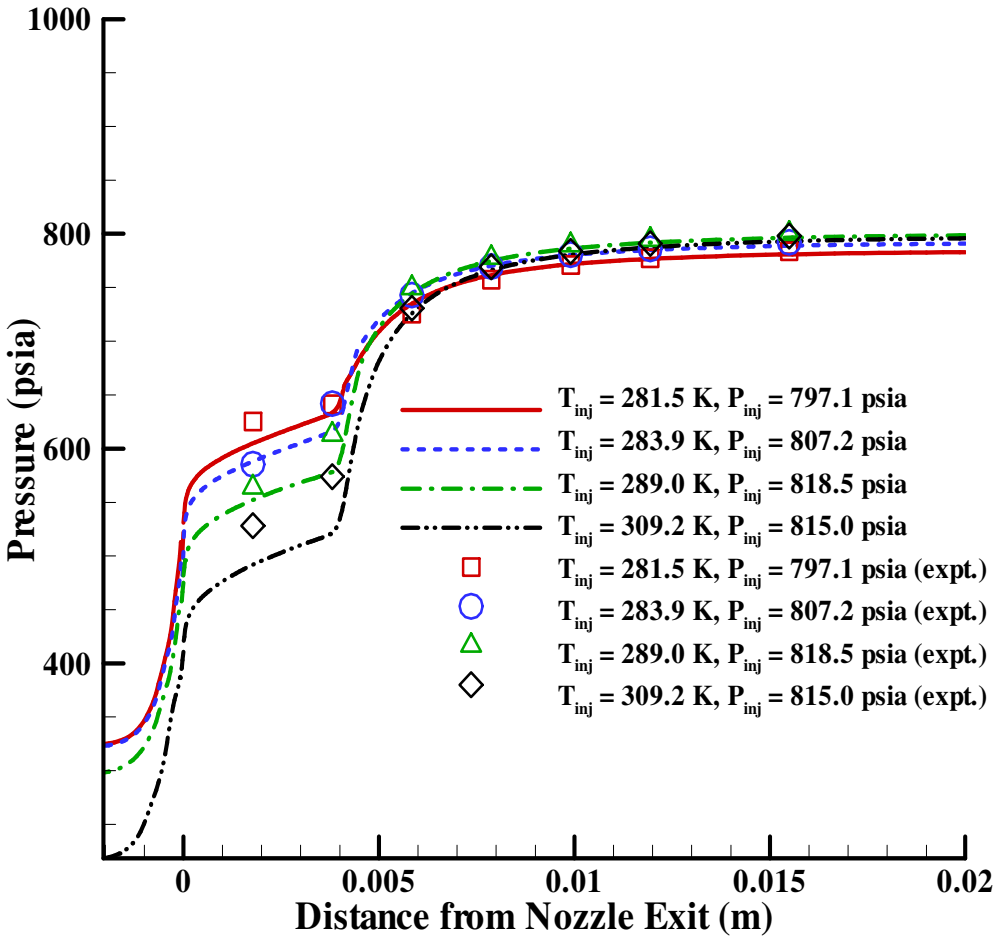

Figure 5.9: Effect of Injectant Temperature on Wall Pressure Distributions

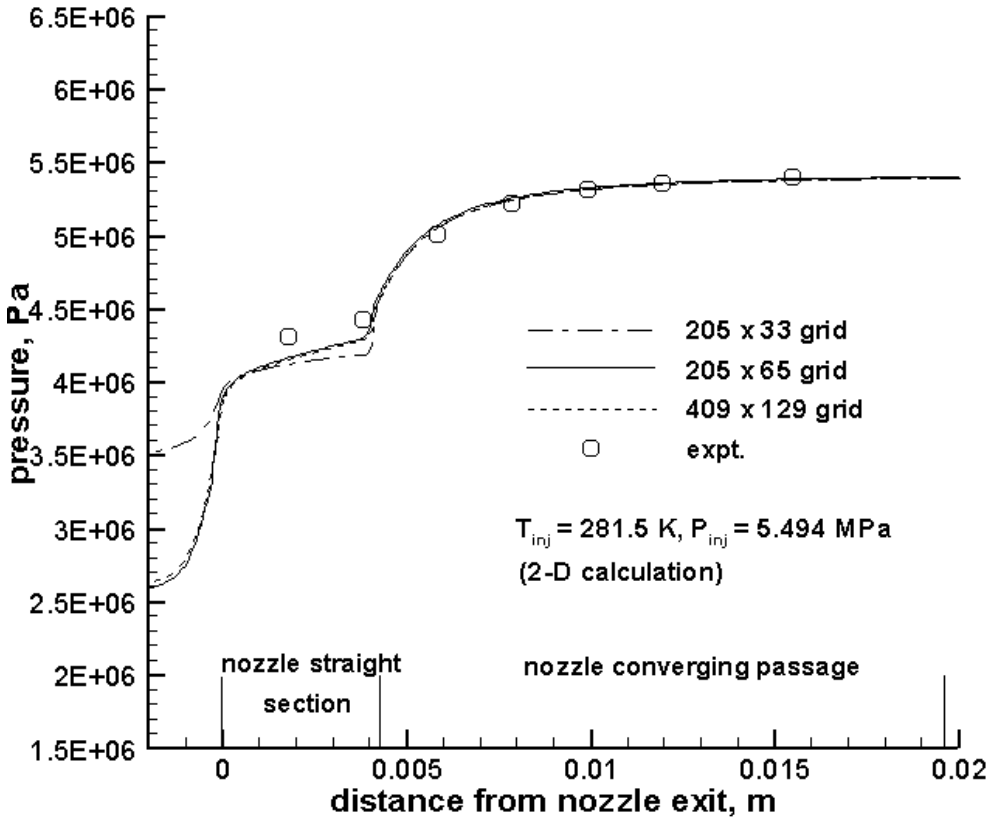

Figure 5.10: Effect of Mesh Refinement on Wall Pressure Distributions at T_{inj}=281.5 K (Two-Dimensional Calculations)

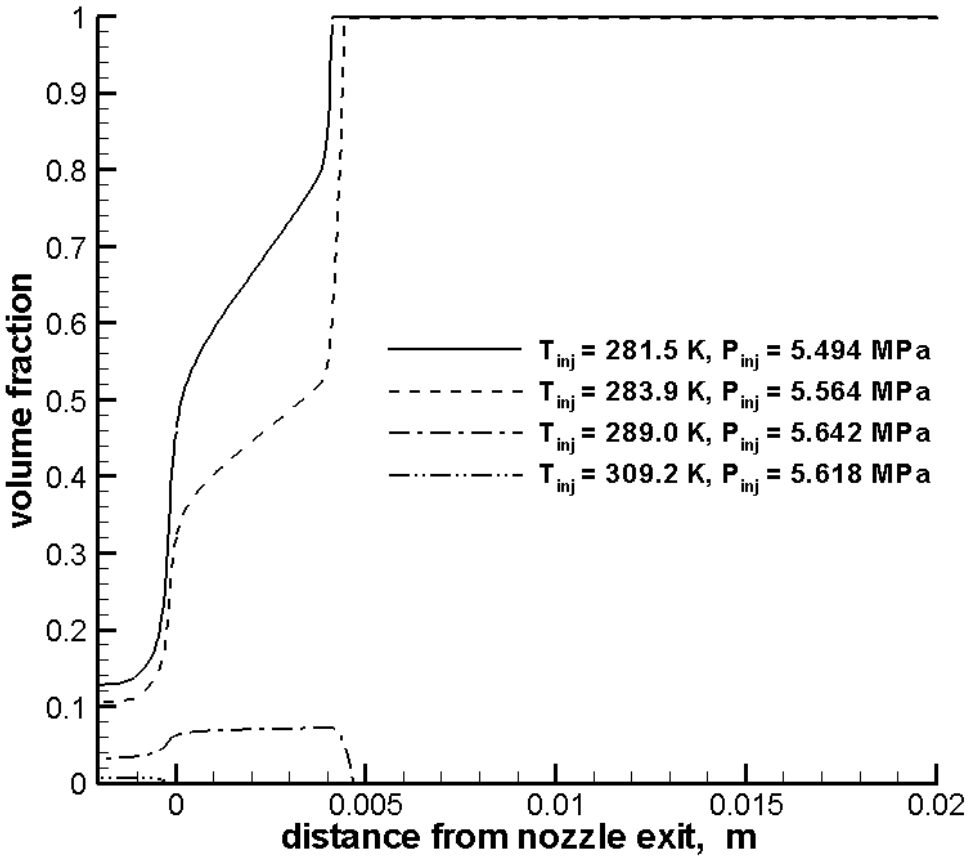

Figure 5.11: Effect of Injectant Temperature on Centerline Liquid Volume Fraction

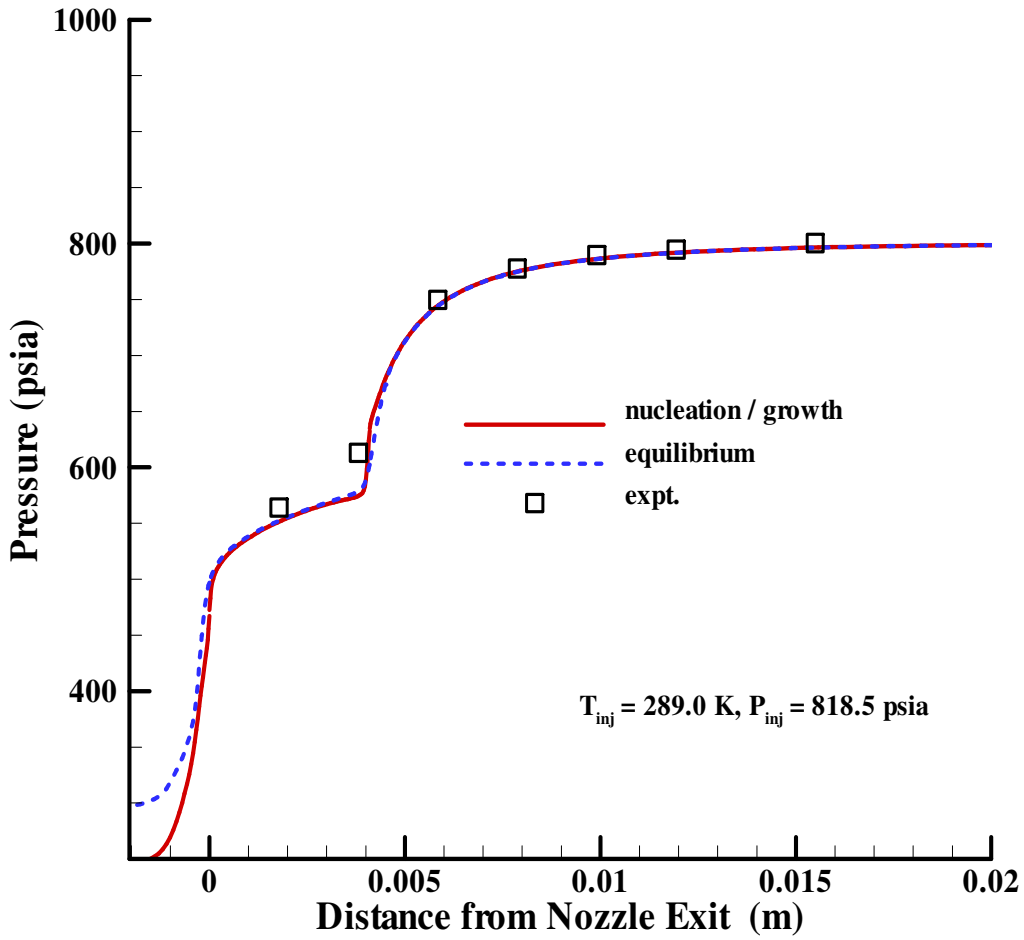

Figure 5.12: Pressure Distributions at T_{inj} = 289.0 K: Homogeneous Equilibrium Model and Nucleation/Growth Model

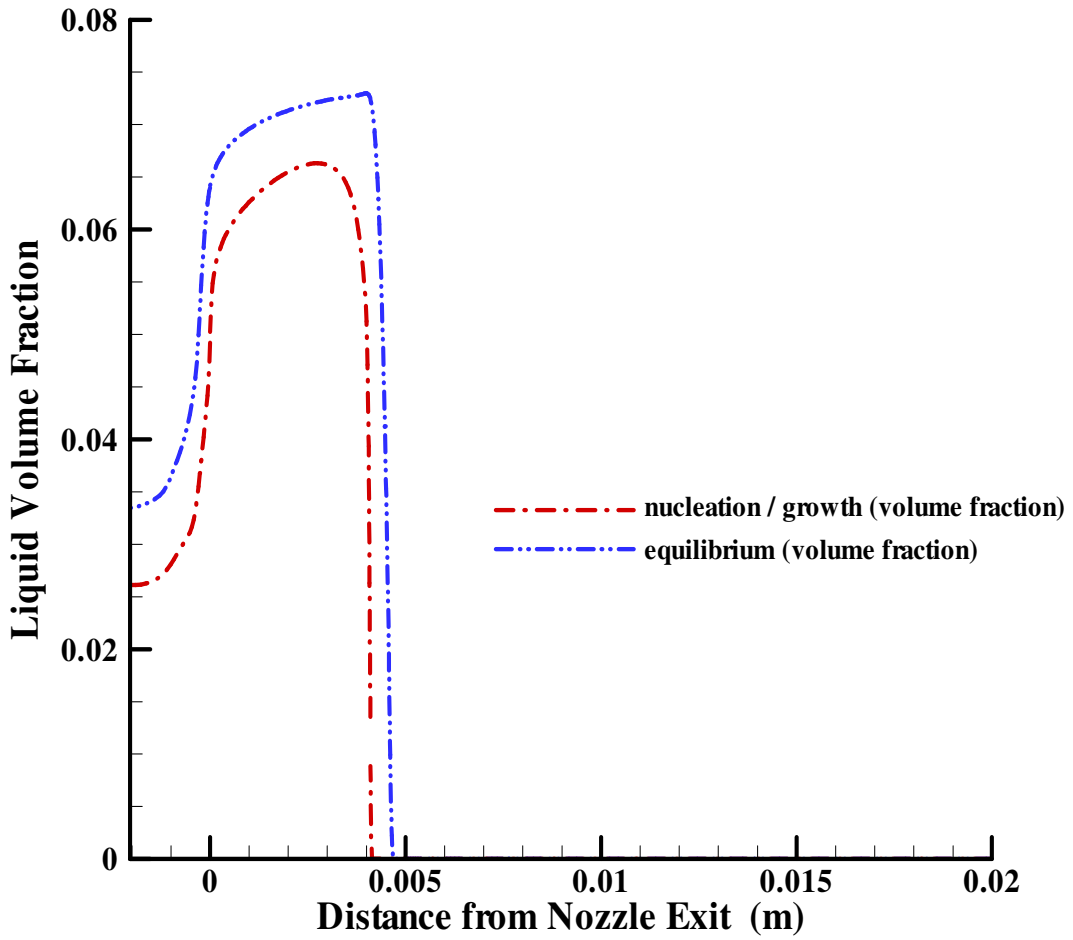

Figure 5.13: Liquid Volume Fraction Distributions at T_{inj} = 289.0 K: Homogeneous Equilibrium Model and Nucleation/Growth Model

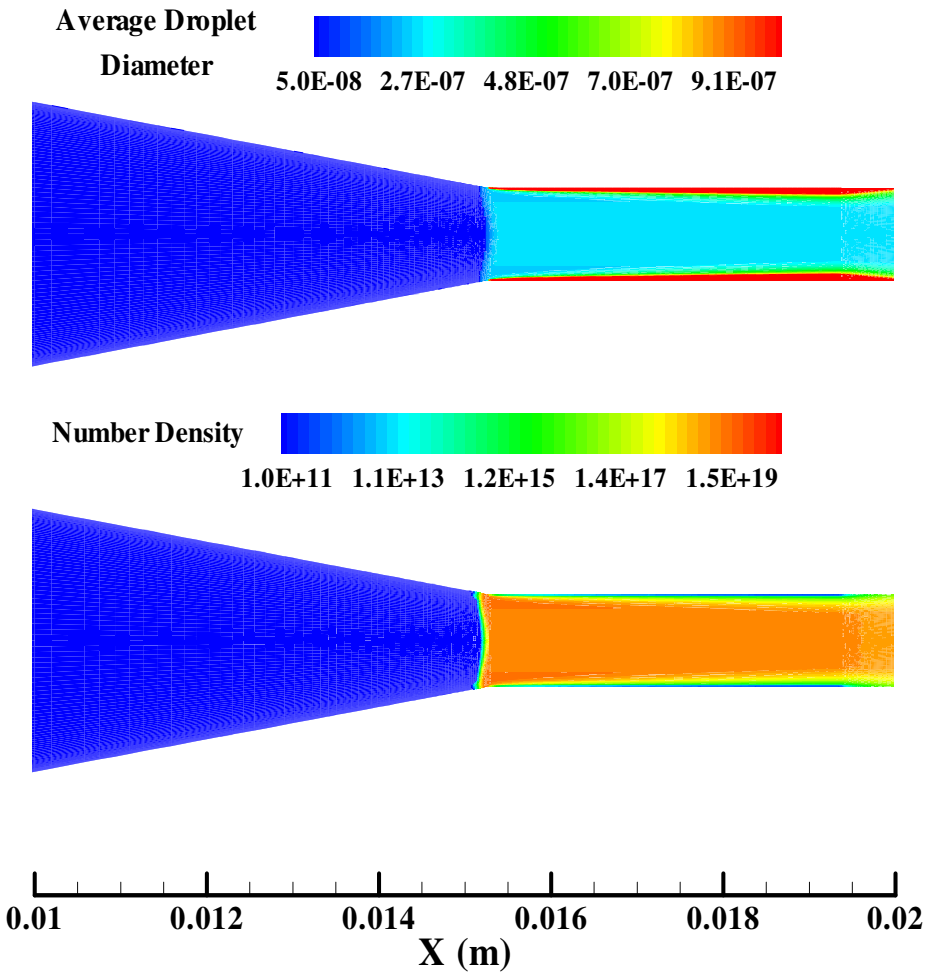

Figure 5.14: Contour Plots of Average Droplet Diameter and Droplet Number Density

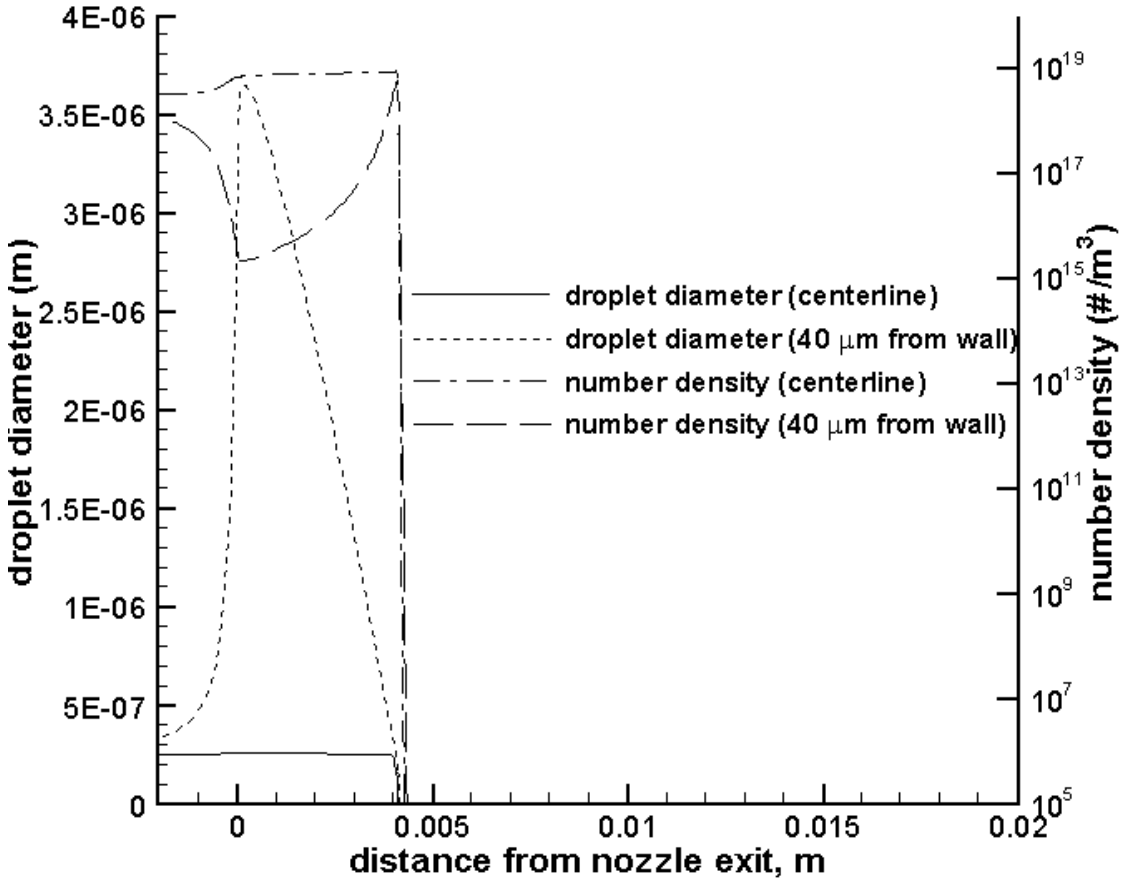

Figure 5.15: Average Droplet Diameter and Number Density Distributions

(Centerline and Near-wall)

5.2 ETHYLENE/METHANE MIXTURE INJECTION

The following cases were computed for different injectant temperatures and involve the injection of a mixture containing 90% ethylene and 10% methane by volume into the rectangular nozzle configuration illustrated in Figure 4.2. These two-dimensional numerical simulations use the aerosol transport model to account for two-phase flow phenomena, as well as Menter's two-equation turbulence model for turbulence closure. The conditions used for these cases (listed on Table 5.4) are based on unpublished imaging data obtained from the experiments of Lin, et al.

Table 5.4: Conditions for Ethylene/Methane Mixture Injection Experiments

Case Number	T_r	P_r	T_{inj} (K)	P_{inj} (MPa)
1	1.02	1.05	282.030	5.65389
2	1.05	1.09	290.325	5.87395
3	1.06	1.09	293.090	5.87395
4	1.08	1.10	298.620	5.92784
5	1.12	1.14	309.680	6.14339

As was discussed previously, the homogeneous nucleation model is only valid for cases where the process path of the mixture first expands the supercritical fluid to the dew-point line. Futher expansion leads to the formation of droplets (condensation). All conditions studied for the ethylene/methane mixture injection (Table 5.4) follow a process path where the homogeneous nucleation model should be valid, as illustrated in Figure 5.16. The dew-point curve shown in Figure 5.16 does not reach the expected peak at the mixture critical point. This is due to the failure of Supertrapp to solve the vapor-liquid equilibrium problem accurately near the critical point.

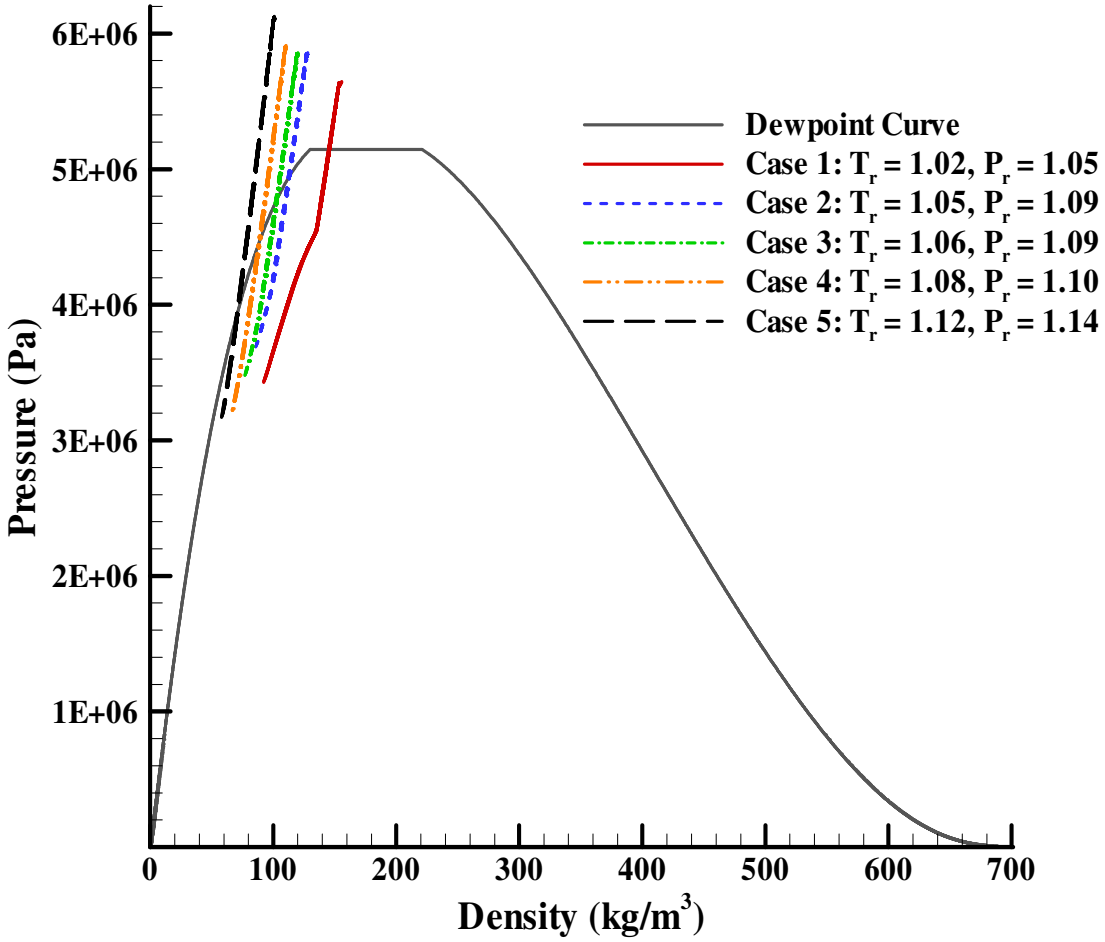

Figure 5.16: Centerline Pressure-Density Process Path for Ethylene/Methane Mixture Injection for Different Injectant Temperatures

Initial calculations for the nucleation/growth model use the pure-ethylene surface tension and the constant Schmidt number form for the diffusion coefficient. Figure 5.17 compares shadowgraph imaging data with liquid-phase volume fraction predictions for the conditions listed on Table 2.1.

The tendency of increasing amount of liquid within the nozzle with decreasing

injectant temperatures is observed for all injectant temperatures, where the onset of condensation is indicated by the darker contours in the solution. However, the predicted location of condensation onset occurs further downstream from the nozzle exit as compared to the experimental results. The onset of condensation is mainly a function of nucleation rate, which is strongly dependent upon the surface tension and solution thermodynamics. This implies that the use of a pure ethylene surface tension curve fit may not be appropriate for the mixture model.

The model was then changed to include the multi-component surface tension expression (Eq. (2.7.19)), as well as a diffusion coefficient modified for high pressures (Eq. (2.7.29)). An improvement in the predicted onset location is observed in Figure 5.18 for all temperatures, especially at the lowest temperatures of 282.03 K, and 290.32 K. However, the exact location of the onset of condensation still does not match the experimental data as well as it did for pure ethylene injection (Figure 5.7).

Figure 5.19 shows ethylene liquid mass fraction distributions along the centerline of the nozzle. The liquid ethylene mass fraction is higher at lower temperatures, as also seen in the pure ethylene injection cases. Figure 5.20 provides centerline pressure distribution for the different injectant conditions. These do not display the trend of a reduced amount of internal expansion with decreasing injectant temperature as observed in the pure ethylene injection cases.

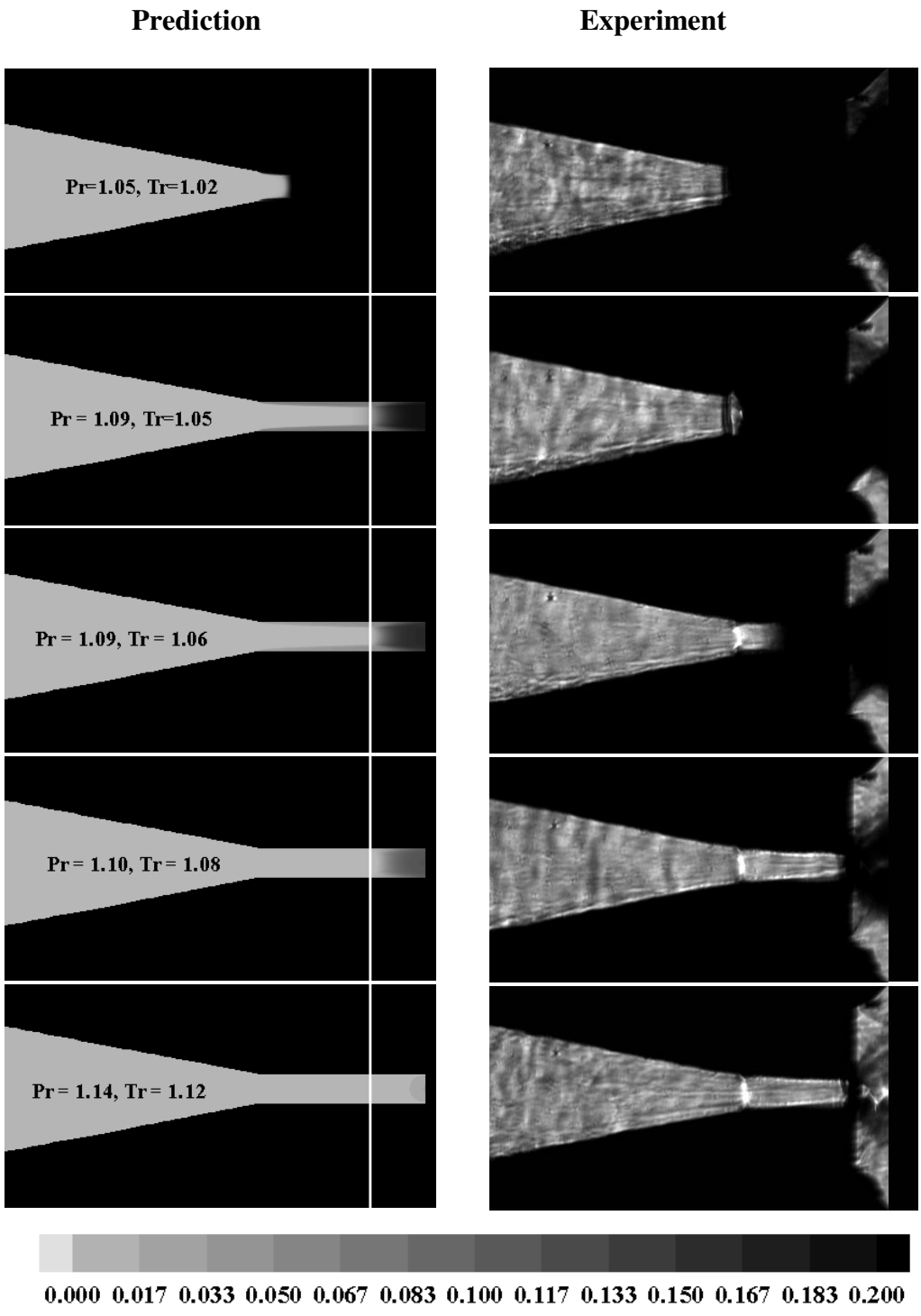

Figure 5.17: Effect of Injectant Temperature on Onset of Condensation (Liquid Ethylene Mass Fraction): Pure Ethylene Phase Surface Tension and Diffusion

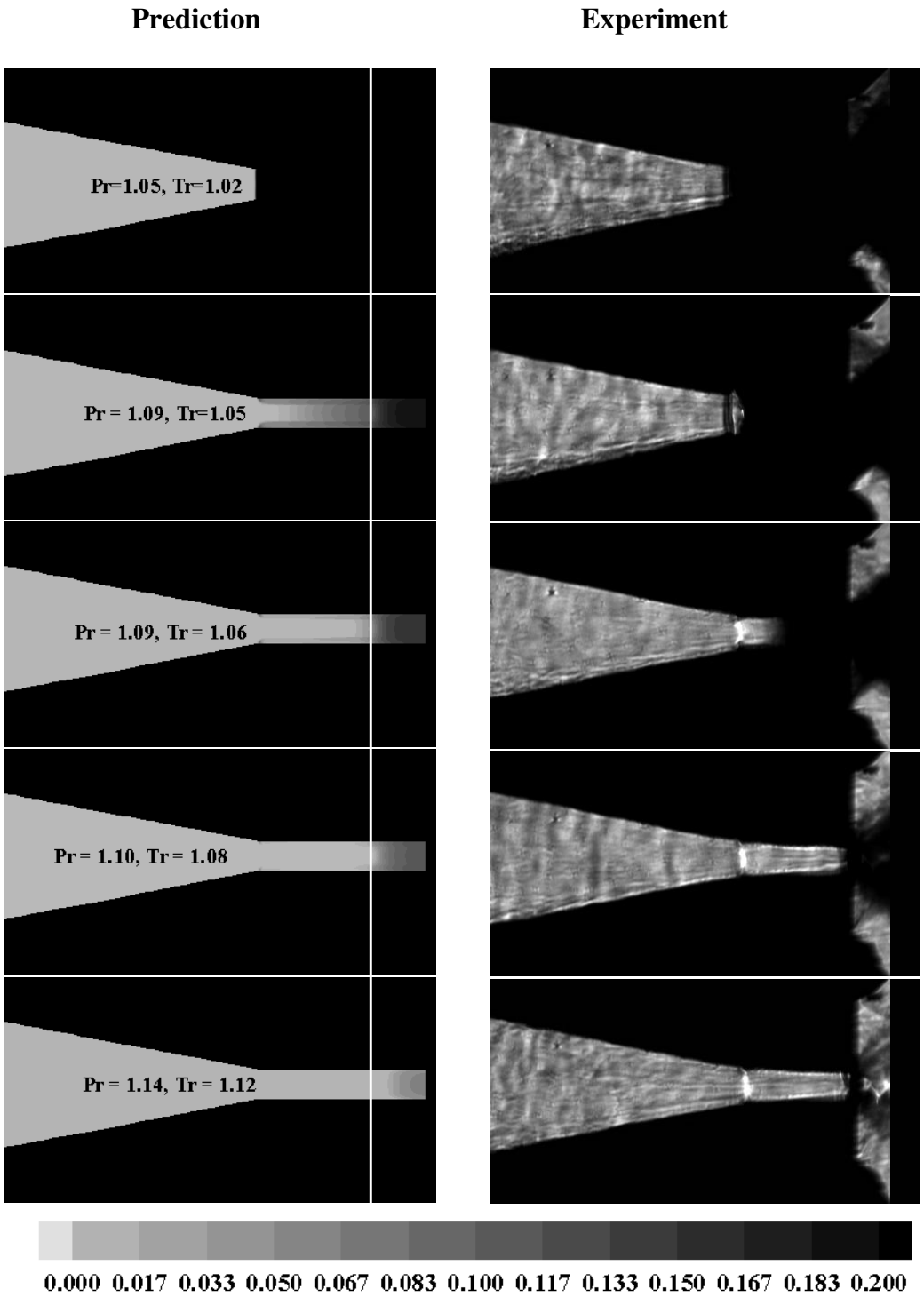

Figure 5.18: Effect of Injectant Temperature on Onset of Condensation (Liquid Ethylene Mass Fraction): Binary-Mixture Surface Tension and Diffusion

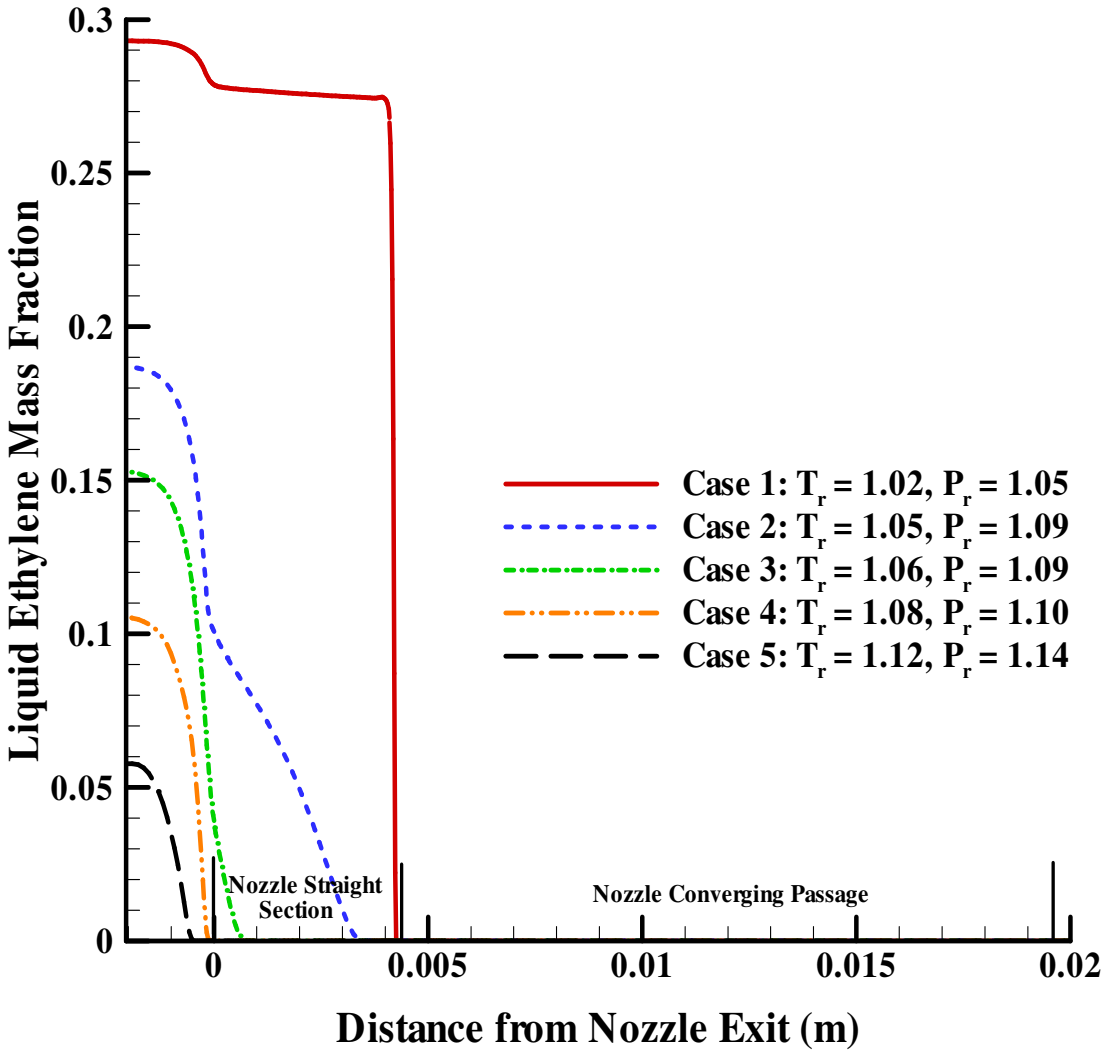

Figure 5.19: Effect of Injectant Temperature on Centerline Liquid Ethylene Mass Fraction Distributions

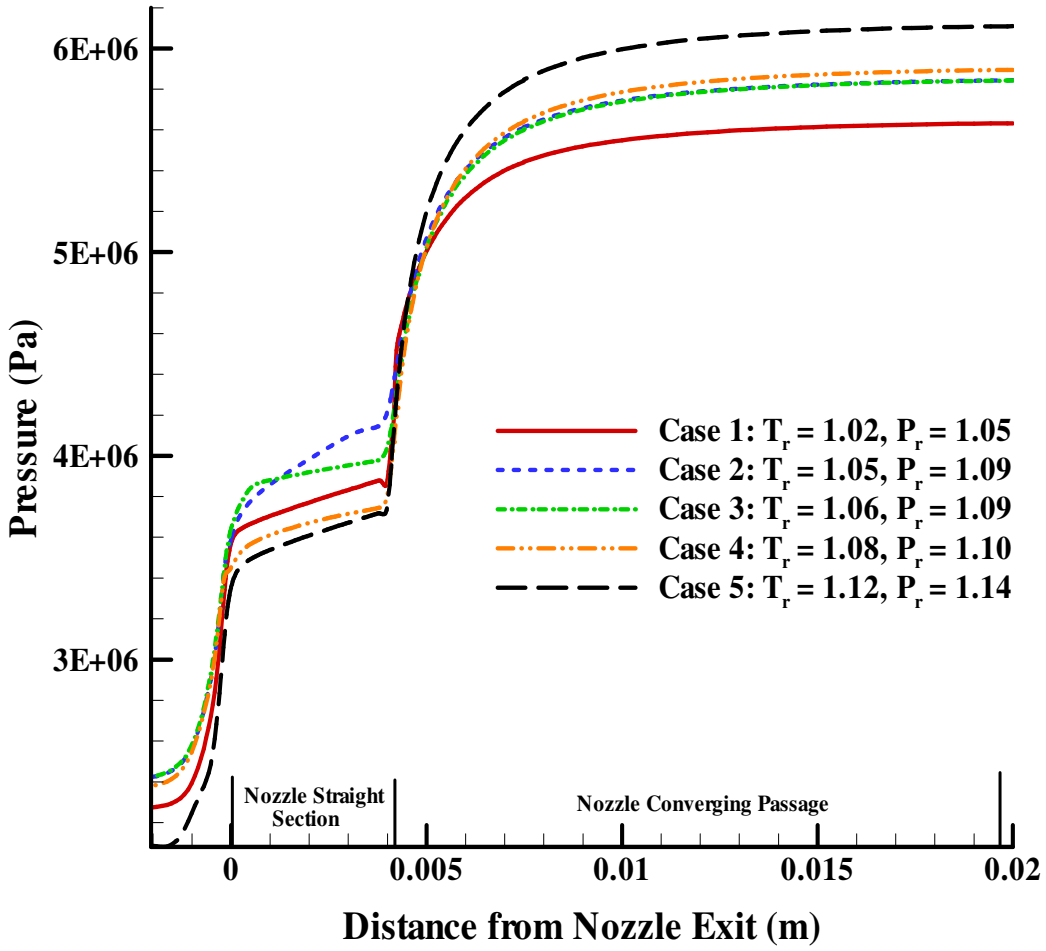

Figure 5.20: Effect of Injectant Temperature on Centerline Pressure Distributions

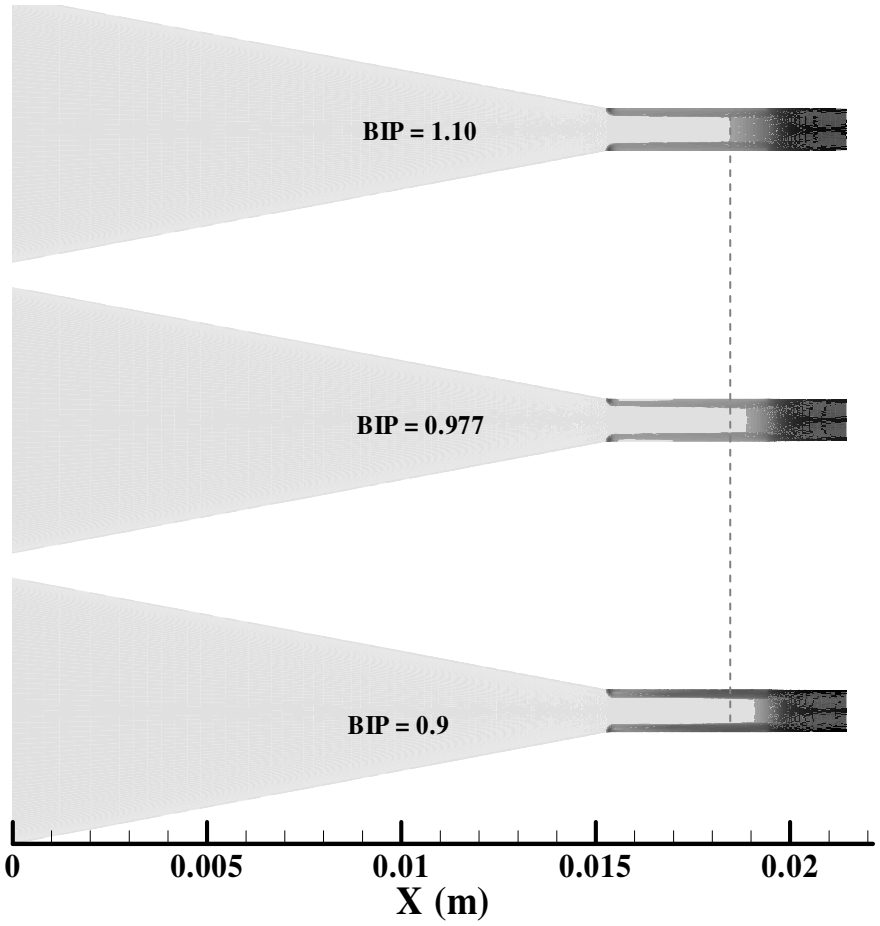

Figure 5.21: Effect of Ethylene/Methane Binary Interaction Parameter on Onset of Condensation within the Nozzle

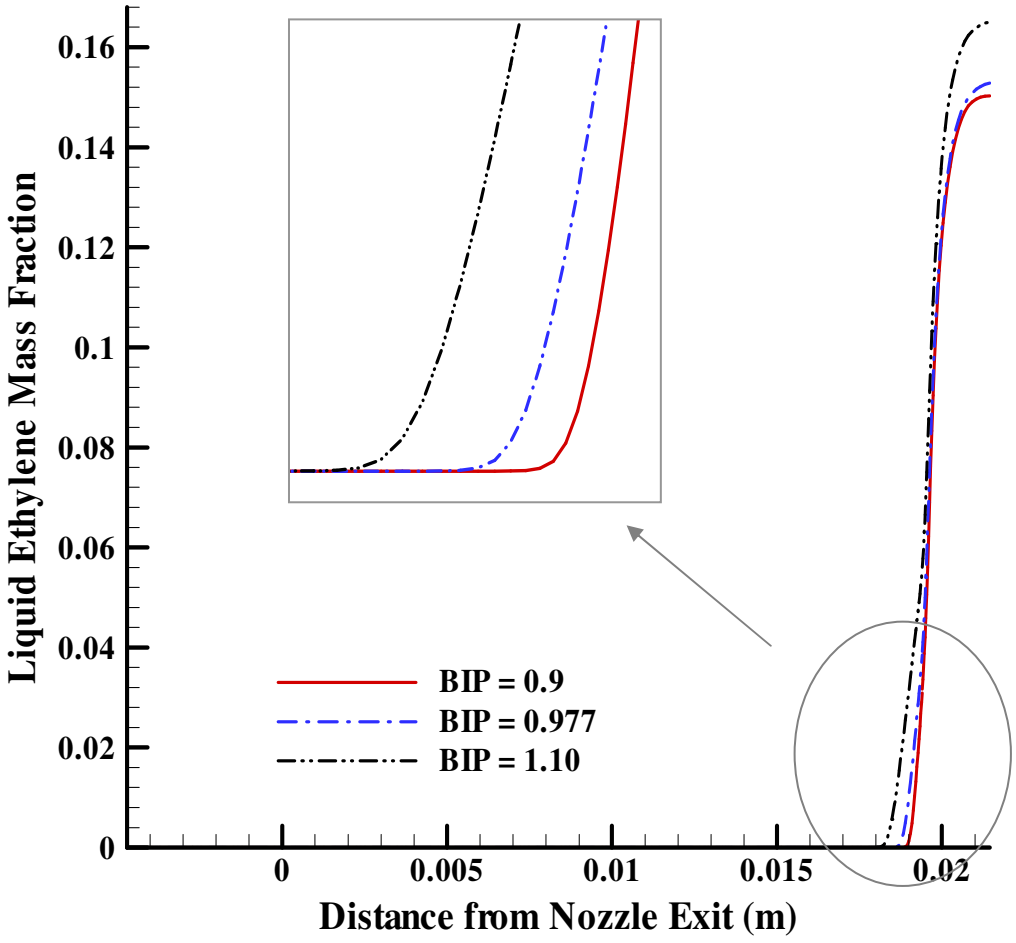

Figure 5.22: Effect of Ethylene/Methane Binary Interaction Parameter on Centerline Onset of Condensation within the Nozzle

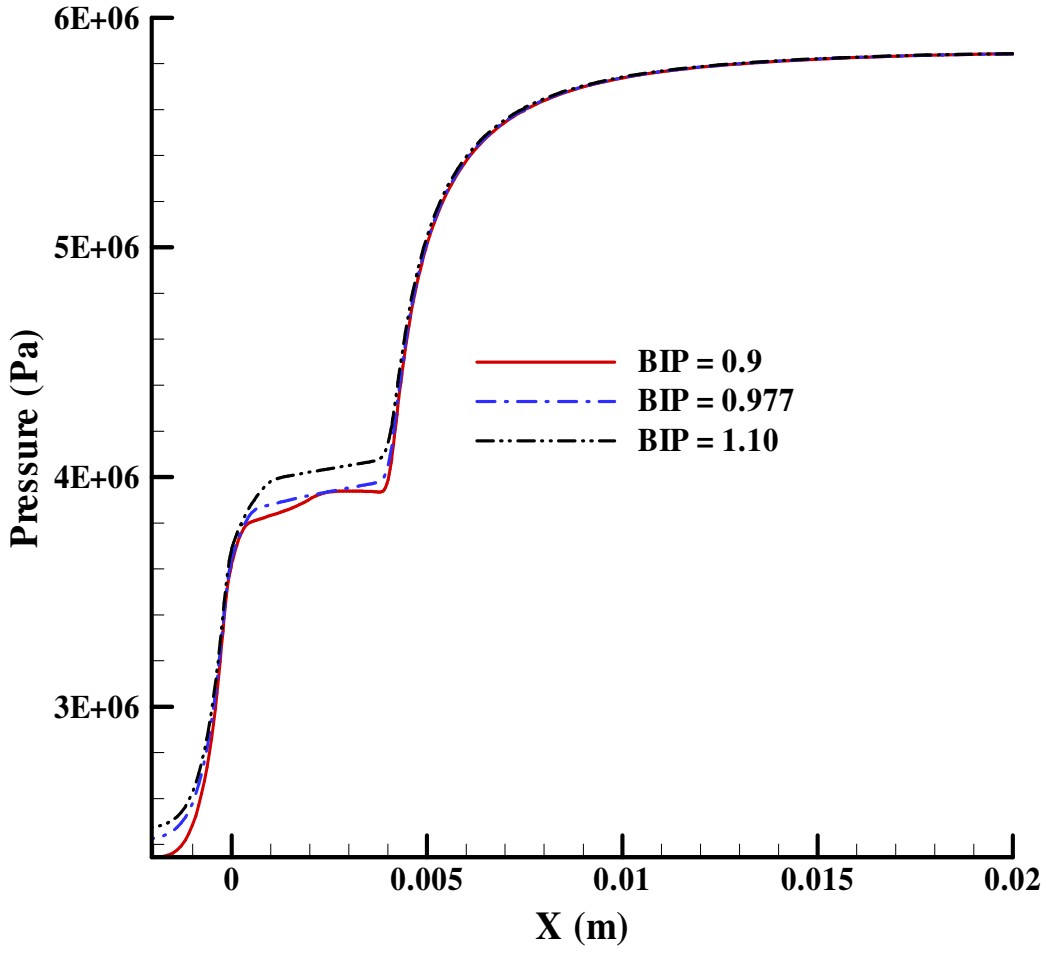

Figure 5.23: Effect of Ethylene/Methane Binary Interaction Parameter on Centerline Onset of Condensation within the Nozzle

Although the injection cases studied for ethylene/methane mixture model utilize the same principles and equations inherent in the pure ethylene injection model (case 4), the mixture model fails to predict the location of the onset of phase transition within the nozzle as well as it did for the pure ethylene cases. This outcome might be attributed to the inability of the mixing rules to correctly model the thermodynamic interactions between ethylene and methane at supercritical and near critical conditions. The binary

interaction parameter in the mixing rules is devoid of physical meaning and is obtained by curve-fitting experimental data using a particular set of mixing rules and an equation of state. To the author's knowledge, most binary interaction parameter studies are carried out for conditions below the critical point. The binary interaction parameter used in this investigation was obtained for such conditions and might not be suitable for conditions near and above the critical point.

Figure 5.21 illustrate the effect of varying the binary interaction parameter on onset of condensation. It is seen that the condensed phase is formed closer to the entrance of the nozzle with increasing interaction parameter. This result is also shown in Figure 5.22, where the ethylene liquid mass fraction distribution is given at the centerline location. Pressure distributions along the centerline is also affected by binary interaction parameter values, as shown in Figure 5.23, where the flow seems to expand further with decreasing interaction parameter value.

6 CONCLUSIONS

A computational fluid dynamics approach for modeling the injection of supercritical ethylene into nitrogen as well as the expansion of ethylene and ethylene/methane mixture within axisymmetric and three-dimensional nozzle configurations has been applied to geometries and test conditions utilized in different experimental investigations. Both a homogeneous equilibrium model and a finite-rate phase transition model based on aerosol dynamics theory were used to account for phase transitions. The computational solutions for pure ethylene injection confirmed many of the qualitative trends noted in the experiments, such as decreased amounts of condensate in the ethylene jets with increasing injectant temperature or decreasing chamber pressure. The computational model also captures the establishment of a choked-flow state at low injectant temperatures and at high chamber pressures. The results also highlight the sensitivity of the position of the Mach disk with changing injectant temperature as well as the decreasing expansion angle of the exiting jet with increasing injectant temperature.

In addition, predictions of the onset of the phase transition of pure ethylene within a transparent injector nozzle are in good agreement with direct-lighting imaging results. Predictions of the pressure distributions within the injectors and mass flow rates are also in good agreement with measured data. Direct comparisons of the extent of condensate penetration into the jet mixing zone indicate that the homogeneous equilibrium model may be inadequate in this region, due to the presence of large droplets that do not vaporize rapidly and may not follow the flow. Quantitative predictions of mole fraction

profiles and temperature profiles exhibit some deviations from the experimental measurements, indicating that further improvements in the characterization of the nozzle flow prior to injection and in modeling turbulence effects in the jet mixing zone are necessary.

Where both are applicable, the nucleation/growth model provides predictions similar to that of the homogeneous equilibrium model but also yields three-dimensional droplet-diameter and number-density distributions. The use of this model appears to be restricted to higher injectant temperatures, where the formation of a disperse liquid phase from a supersaturated vapor is the expected physical response.

The pure ethylene injection model, which implements the aerosol transport model to account for phase transitions, was modified to account for expansion of binary mixtures of ethylene/methane through the three-dimensional nozzle. The mixture model solution showed increasing amount of condensate within the nozzle with decreasing injectant temperatures as described by the experimental data. Unlike the pure ethylene injection model, the mixture model was not very successful at predicting the onset of the phase transition within the nozzle. This result indicates that the mixing rules utilized in the computation may not provide the appropriate thermodynamic behavior of ethylene/methane mixtures at supercritical conditions. More quantitative comparisons were not possible for the ethylene/methane system due to the lack of experimental data. Three-dimensional effects, considered in the pure ethylene calculations but not in the methane/ethylene calculations, may also play a role in the observed discrepancies.

7 REFERENCES

1 Anderson, D. A., Tannehill, J. C., and Pletcher, R. H., Computational Fluid Mechanics and Heat Transfer, Second Edition, Taylor and Francis, 1984.

2 Anderson, J. D., Modern Compressible Flow with Historical Perspective, Third Edition, McGraw Hill Inc., New York, 2003.

3 Aoyama, Y., and Nakano, J., *RS/6000 SP: Practical MPI Programming*, IBM Corporation, 1999.

4 Choi, Y. H. and Merkle, C. L., "The Application of Preconditioning in Viscous Flows," Journal of Computational Physics, Vol. 105, 1993, pp. 207-223.

5 Edwards, T., "USAF Supercritical Hydrocarbon Fuels Interests," AIAA Paper 93-0807, Jan. 1993.

6 Edwards, J.R., Franklin, R.K., and Liou, M.-S., "Low Diffusion Flux-Splitting Methods for Real Fluid Flows with Phase Transitions," *AIAA Journal*, Vol. 38, No. 9, 2000, pp.1624-1634.

7 Edwards, J.R., "Towards Unified CFD Simulations of Real Fluid Flows," (invited), AIAA Paper 2001-2524CP, June, 2001.

8 Edwards, J.R., Pinto, A.M., Lin, K.-C, and Jackson, T.A., "Simulation of Injection of Supercritical Methane/Ethylene Mixtures into Nitrogen," AIAA Paper 2003-4267, June, 2003.

9 Edwards, J. R., "Development of an Upwind Relaxation Multigrid Method for Computing Three-dimensional, Viscous Internal Flows," *AIAA Journal of Propulsion and Power*, Vol. 12, 1996, pp. 146-154.

10 Edwards, J. R., "A Low-Diffusion Flux-Splitting Scheme for Navier-Stokes Calculations," *Computers and Fluids*, Vol. 26, No. 6, 1997, pp. 635-659.

11 Franklin, R.K., Edwards, J.R., Chernyak, Y., Gould, R.D., Henon, F., and Carbonell, R.G., "Formation of Perfluoropolyether Coatings by the Rapid Expansion of Supercritical Solutions (RESS) Process. Part 2: Numerical Modeling," *Industrial and Engineering Chemistry Research*, Vol. 40, No. 23, 2001, pp. 6127-6139.

12 Friedlander, S.K., *Smoke, Dust, and Haze: Fundamentals of Aerosol Behavior*, Wiley Interscience, New York, 1977.

13 Friedlander, S.K., *Smoke, Dust, and Haze: Fundamentals of Aerosol Dynamics*, second edition, Oxford University Press, New York, 2000.

14 Handbook of Chemistry and Physics, 85th edition, D. Lide, Editor in Chief, CRC Press, 2004.

15 Hirsch, C., Numerical Computation of Internal and External Flows, Volume 2, John Wiley and Sons Ltd., 1990.

16 Holland, P.M., Eaton, B.E., and Hanley, H.J.M. "A Correlation of the Viscosity and Thermal Conductivity Data for Gaseous and Liquid Ethylene," *Journal of Physical and Chemical Reference Data*, Vol. 12, No. 3, 1983, pp.917-932.

17 Kwauk, X., Debenedetti, P.G., "Mathematical Modeling of Aerosol Formation by Rapid Expansion of Supercritical Solutions in a Converging Nozzle," *Journal of Aerosol Science*, Vol. 24, No. 4, 1993, pp. 445-469.

18 Lin, K.-C., Cox-Stouffer, S., Kennedy, P.J., and Jackson, T.A., "Expansion of Supercritical Methane/Ethylene Jets in a Quiescent Subcritical Environment," AIAA Paper 2003-0483, Jan. 2003.

19 Lindau, J.W. Venkateswaran, S., Kunz, R.F., and Merkle, C.W., "Development of a Fully Compressible Multi-Phase Reynolds-Averaged Navier-Stokes Model," AIAA Paper 2001-2648, June, 2001.

20 Liou, M.-S. and Steffen, C. J., "A New Flux Splitting Scheme," *Journal of Computational Physics*, Vol. 107, 1993, pp. 23-39.

21 Liou, M.-S., "Ten Years in the Making-AUSM-family," AIAA Paper 2001-2521, June 2001.

22 Liou, M.-S., "Progress Towards an Improved CFD Method: AUSM+," AIAA Paper 95-1701, June 1995.

23 McBride, B.J., Gordon, S., and Reno, M.A., "Coefficient for Calculating Thermodynamic and Transport Properties of Individual Species," NASA TM-4513, Oct. 1993.

24 Menter, F.R., "Eddy Viscosity Transport Equations and Their Relation to the k-epsilon Model," *ASME Journal of Fluids Engineering*, Vol. 119, No. 12, 1997, pp. 876-884.

25 Menter, F.R., "Two Equation Eddy Viscosity Turbulence Models for Engineering Applications," *AIAA Journal*, Vol. 32, No. 8, 1994, pp. 1598-1605.

26 Nishiumi, H. and Arai, T., "Generalization of the Binary Interaction Parameter of the Peng-Robinson Equation of State by Component Family," *Fluid Phase Equilibria*, Vol. 42, 1988, pp. 43-62

27 Peng, D.-Y. and Robinson, D.B., "A New Two-Constant Equation of State," *Industrial and Engineering Chemistry Fundamentals*, Vol.15, No. 1,1976, pp. 59-64.

28 Poling, B. E., Prausnitz, J. M., and O'Connell, J. P., The Properties of Gases and Liquids, Fifth Edition, McGraw-Hill, 2001.

29 Quayle, O. R., "The Parachors of Organic Compounds," *Chemical Review*, Vol. 53, 1953, pp.439.

30 Saffman, P. and Turner, J., "On the Collision of Drops in Turbulent Clouds" *Journal of Fluid Mechanics* Vol. 1, 1956, pp. 16.

31 Smukala, J., Span, R., and Wagner, W. "New Equation of State for Ethylene Covering the Fluid Region for Temperatures From the Melting Line to 450 K at Pressures up to 300 MPa," *Journal of Physical and Chemical Reference Data*, Vol. 29, No. 5, 2000, pp.1053-1119.

32 Snir, M., et. al., MPI: The Complete Reference, The MIT Press, 1996.

33 Suresh, A. and Huynh, H. T., "Numerical Experiments on a New Class of Nonoscillator Schemes," AIAA Paper 92-0421, January 1992.

34 Tian, M., Edwards, J.R., Lin, K.-C., and Jackson, T.A., "Numerical Simulation of Transient Two-Phase Flow within Aerated-Liquid Injectors", AIAA Paper 2003-4226, June, 2003.

35 Tian, M., Xiao, X., Edwards, J.R., Lin, K.-C., and Jackson, T.A., "Numerical Simulation and Experimental Characterization of the Internal Two-Phase Flow within an Aerated Liquid Injector," AIAA Paper 2004-2645, June, 2004.

36 Turkel, E., "Preconditioned Methods for Solving the Incompressible and Low Speed Compressible Equations," Journal of Computational Physics, Vol. 72, 1987, pp. 277-298.

37 Weiss, J.M. and Smith, W.A., "Preconditioning Applied to Variable and Constant Density Flows," *AIAA Journal*, Vol. 33, No. 11, 1995, pp. 2050-2057.

38 Wesseling, P., "Introduction to Multigrid Methods," NASA CR-195045, 1995.

39 Wilcox, D. C., Turbulence Modeling for CFD, Second Edition, DCW Industries, 2002.

40 Wu, P.-K., Chen, T.H., Nejad, A.S., and Carter, C.D., "Injection of Supercritical Ethylene into Nitrogen," *Journal of Propulsion and Power*, Vol. 12, No. 4, 1996, pp. 770-777.

41 Wu, P.-K., Shahnam, M., Kirkendall, K.A., Carter, C.D., and Nejad, A.S., "Expansion and Mixing Process of Underexpanded Supercritical Fuel Jets Injected into Super-heated Conditions," *Journal of Propulsion and Power*, Vol. 15, No. 5, 1999, pp. 642-649.

APPENDIX A: SPECIES DIFFUSION VELOCITIES AND HOW THEY APPLY TO THE GOVERNING EQUATIONS FOR MULTI-COMPONENT, TWO-PHASE MIXTURES

The mass conservation equation of species k in a multi-component, two-phase (vapor and liquid) system is defined as

$$\frac{\partial}{\partial t}\left(\rho Y_v y_k^v\right)+\frac{\partial}{\partial x_j}\left(\rho Y_v y_k^v\left(u_j+u_{d,k,j}^v\right)\right)=\omega_k^v \tag{A.1}$$

$$\frac{\partial}{\partial t}\left(\rho Y_l y_k^l\right)+\frac{\partial}{\partial x_j}\left(\rho Y_l y_k^l\left(u_j+u_{d,k,j}^l\right)\right)=\omega_k^l \tag{A.2}$$

where u_j is the convective speed in the j-direction and $u_{d,k,j}^{v,l}$ is the molecular diffusion velocity for species k in the j-direction in vapor or liquid phase. The molecular diffusion velocities are defined in a form similar to Fick's law

$$u_{d,k,j}^v=-\frac{D}{Y_v y_k^v}\frac{\partial}{\partial x_j}\left(Y_v y_k^v\right) \tag{A.3}$$

$$u_{d,k,j}^l=-\frac{D}{Y_l y_k^l}\frac{\partial}{\partial x_j}\left(Y_l y_k^l\right) \tag{A.4}$$

where D is the diffusion coefficient, which is assumed to be the same for all species, obtained from the definition of the Schmidt number $\left(Sc=\frac{\mu}{\rho Y_v D}\right)$. The Schmidt number is assumed to be 0.5 for all vapor phase species.

The species mass conservation equations are summed in order to obtain the phasic mass conservation equations given as follows

$$\frac{\partial}{\partial t}(\rho Y_v)+\frac{\partial}{\partial x_j}\left(\rho Y_v\left(u_j+\sum_{k=1}^{NV}u_{d,k,j}^{v}\right)\right)=\sum_{k=1}^{NV}\omega_k^v \qquad \textbf{(A.5)}$$

$$\frac{\partial}{\partial t}(\rho Y_l)+\frac{\partial}{\partial x_j}\left(\rho Y_l\left(u_j+\sum_{k=1}^{NL}u_{d,k,j}^{l}\right)\right)=\sum_{k=1}^{NL}\omega_k^l \qquad \textbf{(A.6)}$$

Using the definition for the molecular diffusion velocities, the above equations can be written as

$$\frac{\partial}{\partial t}(\rho Y_v)+\frac{\partial}{\partial x_j}\left(\rho Y_v u_j-\rho D\frac{\partial}{\partial x_j}(Y_v)\right)=\sum_{k=1}^{NV}\omega_k^v \qquad \textbf{(A.7)}$$

$$\frac{\partial}{\partial t}(\rho Y_l)+\frac{\partial}{\partial x_j}\left(\rho Y_l u_j-\rho D\frac{\partial}{\partial x_j}(Y_l)\right)=\sum_{k=1}^{NL}\omega_k^l \qquad \textbf{(A.8)}$$

where the terms $\rho D\frac{\partial}{\partial x_j}(Y_v)$ and $\rho D\frac{\partial}{\partial x_j}(Y_l)$ represent the diffusion of mass between phases (interphase diffusion). The total mass conservation equation is obtained by adding Eqs. A.5 and A.6

$$\frac{\partial}{\partial t}(\rho)+\frac{\partial}{\partial x_j}(\rho u_j)=\sum_{k=1}^{NV}\omega_k^v+\sum_{k=1}^{NL}\omega_k^l=0 \qquad \textbf{(A.9)}$$

The species energy conservation is written using species continuity equation in the following manner

$$\rho Y_v y_k^v \frac{\mathrm{D}}{\mathrm{D}t}\left(h_k^v\right)+h_k^v\left(\frac{\partial}{\partial t}\left(\rho Y_v y_k^v\right)+\frac{\partial}{\partial x_j}\left(\rho Y_v y_k^v\left(u_j+u_{d,k,j}^v\right)\right)-\omega_k^v\right)=Q_k^v-W_k^v \qquad \textbf{(A.10)}$$

$$\rho Y_l y_k^l \frac{\mathrm{D}}{\mathrm{D}t}\left(h_k^l\right)+h_k^l\left(\frac{\partial}{\partial t}\left(\rho Y_l y_k^l\right)+\frac{\partial}{\partial x_j}\left(\rho Y_l y_k^l\left(u_j+u_{d,k,j}^l\right)\right)-\omega_k^l\right)=Q_k^l-W_k^l \qquad \textbf{(A.11)}$$

where h_k^v and h_k^l are the species enthalpy in the vapor and liquid phase respectively. The above equations are simplified by expanding the substantial derivative $\frac{\mathrm{D}}{\mathrm{D}t}(\ )$ and rearranging in the following manner

$$\frac{\partial}{\partial t}\left(\rho Y_v y_k^v h_k^v\right)+\frac{\partial}{\partial x_j}\left(\rho Y_v y_k^v h_k^v\left(u_j+u_{d,k,j}^v\right)\right)-h_k^v\omega_k^v=Q_k^v-W_k^v \qquad \textbf{(A.12)}$$

$$\frac{\partial}{\partial t}\left(\rho Y_l y_k^l h_k^l\right)+\frac{\partial}{\partial x_j}\left(\rho Y_l y_k^l h_k^l\left(u_j+u_{d,k,j}^l\right)\right)-h_k^l\omega_k^l=Q_k^l-W_k^l \qquad \textbf{(A.13)}$$

The phasic energy conservation equations are obtained by summing over all species

$$\frac{\partial}{\partial t}\left(\rho Y_v h_v\right)+\frac{\partial}{\partial x_j}\left(\rho Y_v\left(h_v u_j+\sum_{k=1}^{NV} y_k^v h_k^v u_{d,k,j}^v\right)\right)-\sum_{k=1}^{NV} h_k^v\omega_k^v=\left(\sum_{k=1}^{NV} Q_k^v-W_k^v\right) \qquad \textbf{(A.14)}$$

$$\frac{\partial}{\partial t}\left(\rho Y_l h_l\right)+\frac{\partial}{\partial x_j}\left(\rho Y_l\left(h_l u_j+\sum_{k=1}^{NL} y_k^l h_k^l u_{d,k,j}^l\right)\right)-\sum_{k=1}^{NL} h_k^l\omega_k^l=\sum_{k=1}^{NL}\left(Q_k^l-W_k^l\right) \qquad \textbf{(A.15)}$$

where $h_v=h_v\left(y_k^v,p,T\right)$ and $h_l=h_l\left(y_k^l,p,T\right)$. The phasic enthalpies can be written as a function of the mass fractions $h_v=\sum_{k=1}^{NV} y_k^v h_k^v$ and $h_l=\sum_{k=1}^{NL} y_k^l h_k^l$ by assuming that the following relationships are satisfied in our system

$$h_k^v = \frac{\partial h_v}{\partial y_k^v} \tag{A.16}$$

$$h_k^l = \frac{\partial h_l}{\partial y_k^l} \tag{A.17}$$

The total energy equation is obtained by summing the phasic energy equation and applying the relation of total enthalpy to phasic enthalpies $h = Y_v h_v + Y_l h_l$

$$\begin{aligned} &\frac{\partial}{\partial t}(\rho h) + \frac{\partial}{\partial x_j}\left(\rho h u_j + \rho\left(Y_v \sum_{k=1}^{NV} y_k^v h_k^v u_{d,k,j}^v + Y_l \sum_{k=1}^{NL} y_k^l h_k^l u_{d,k,j}^l \right)\right) \\ &\quad = \sum_{k=1}^{NV} h_k^v \omega_k^v + \sum_{k=1}^{NL} h_k^l \omega_k^l + \sum_{k=1}^{NV}\left(Q_k^v - W_k^v\right) + \sum_{k=1}^{NL}\left(Q_k^l - W_k^l\right) \\ &\quad = Q + W \end{aligned} \tag{A.18}$$

where the terms $Y_v \sum_{k=1}^{NV} y_k^v h_k^v u_{d,k,j}^v$ and $Y_l \sum_{k=1}^{NL} y_k^l h_k^l u_{d,k,j}^l$ can be written in terms of the diffusion coefficient using relations A.3-A.4 and A.16-A.17

$$\frac{\partial}{\partial t}(\rho h) + \frac{\partial}{\partial x_j}\left(\rho h u_j - \rho D\left(\sum_{k=1}^{NV} \frac{\partial h_v}{\partial y_k^v} \frac{\partial\left(Y_v y_k^v\right)}{\partial x_j} + \sum_{k=1}^{NL} \frac{\partial h_l}{\partial y_k^l} \frac{\partial\left(Y_l y_k^l\right)}{\partial x_j} \right)\right) = Q - W \tag{A.19}$$

the above equation can be rewritten as follows

$$\frac{\partial}{\partial t}(\rho h)+\frac{\partial}{\partial x_j}\left(\rho h u_j-\rho D\sum_{k=1}^{NV}\frac{\partial h_v}{\partial y_k^v}\left(Y_v\frac{\partial\left(y_k^v\right)}{\partial x_j}+y_k^v\frac{\partial(Y_v)}{\partial x_j}\right)\right.$$
$$\left.-\rho D\sum_{k=1}^{NL}\frac{\partial h_l}{\partial y_k^l}\left(Y_l\frac{\partial\left(y_k^l\right)}{\partial x_j}+y_k^l\frac{\partial(Y_l)}{\partial x_j}\right)\right)=Q-W \qquad \textbf{(A.20)}$$

Equation A.20 can be further simplified yielding the following relation

$$\frac{\partial}{\partial t}(\rho h)+\frac{\partial}{\partial x_j}\left(\rho h u_j-\rho D\left(\sum_{k=1}^{NV}\frac{\partial h_v}{\partial y_k^v}y_k^v-\sum_{k=1}^{NL}\frac{\partial h_l}{\partial y_k^l}y_k^l\right)\frac{\partial(Y_v)}{\partial x_j}\right.$$
$$\left.-\rho D\left(Y_v\sum_{k=1}^{NV}\frac{\partial h_v}{\partial y_k^v}\frac{\partial\left(y_k^v\right)}{\partial x_j}+Y_l\sum_{k=1}^{NL}\frac{\partial h_l}{\partial y_k^l}\frac{\partial\left(y_k^l\right)}{\partial x_j}\right)\right) \qquad \textbf{(A.21)}$$
$$=\frac{\partial}{\partial t}(\rho h)+\frac{\partial}{\partial x_j}\left(\rho h u_j-\rho D\left((h_v-h_l)\frac{\partial(Y_v)}{\partial x_j}+Y_v\sum_{k=1}^{NV}\frac{\partial h_v}{\partial y_k^v}\frac{\partial\left(y_k^v\right)}{\partial x_j}+Y_l\sum_{k=1}^{NL}\frac{\partial h_l}{\partial y_k^l}\frac{\partial\left(y_k^l\right)}{\partial x_j}\right)\right)$$
$$=Q-W$$

APPENDIX B: REAL FLUID SOUND SPEED

The acoustic speed of the real fluid in the vapor and liquid mixture is obtained by an eigenvalue analysis using a generalized equation of state,

$$\rho = \rho(p,T),\ h = h(p,T) \tag{B.1}$$

For simplicity, a 1-D Euler system is used to determine the eigenvalues,

$$\frac{\partial \mathbf{U}}{\partial t} + \frac{\partial \mathbf{E}}{\partial x} = 0,\ \mathbf{U} = \begin{bmatrix} \rho \\ \rho u \\ \rho H - p \end{bmatrix},\ \mathbf{E} = \begin{bmatrix} \rho u \\ \rho u^2 + p \\ \rho H u \end{bmatrix},\ \mathbf{V} = \begin{bmatrix} \rho \\ u \\ T \end{bmatrix} \tag{B.2}$$

where $\mathbf{U}$ is the conservative variable vector, $\mathbf{E}$ is the flux vector, and $\mathbf{V}$ is the primitive variable vector. H is the total enthalpy, $H = h + \frac{1}{2}u^2$. Then the eigenvalues, $\{\lambda_n\}$, are the roots of the characteristic equation resulting from the determinant,

$$\det\left(\frac{\partial \mathbf{V}}{\partial \mathbf{U}}\frac{\partial \mathbf{E}}{\partial \mathbf{V}} - \lambda \mathbf{I}\right) = 0 \tag{B.3}$$

Since it is difficult to compute $\frac{\partial \mathbf{V}}{\partial \mathbf{U}}$ directly, we compute $\frac{\partial \mathbf{U}}{\partial \mathbf{V}}$ first, then take its inverse. $\frac{\partial \mathbf{V}}{\partial \mathbf{U}}$ and $\frac{\partial \mathbf{E}}{\partial \mathbf{V}}$ are obtained as:

$$\frac{\partial \mathbf{U}}{\partial \mathbf{V}} = \begin{bmatrix} \rho_p & 0 & \rho_T \\ \rho_p u & \rho & \rho_T u \\ \rho_p H + \rho h_p - 1 & \rho u & \rho_T H + \rho h_T \end{bmatrix} \tag{B.4}$$

$$\frac{\partial \mathbf{E}}{\partial \mathbf{V}} = \begin{bmatrix} \rho_p u & \rho & \rho_T u \\ \rho_p u^2 + 1 & 2\rho u & \rho_T u^2 \\ \rho_p H u + \rho h_p u & \rho H + \rho u^2 & \rho_T H u + \rho h_T u \end{bmatrix} \tag{B.5}$$

Taking the inverse of $\frac{\partial \mathbf{U}}{\partial \mathbf{V}}$ we get

$$\frac{\partial \mathbf{V}}{\partial \mathbf{U}} = \begin{bmatrix} \frac{\rho_T H + \rho h_T - \rho_T u^2}{\rho \rho_p h_T - \rho \rho_T h_p + \rho_T} & \frac{\rho_T u}{\rho \rho_p h_T - \rho \rho_T h_p + \rho_T} & \frac{\rho_T}{\rho \rho_p h_T - \rho \rho_T h_p + \rho_T} \\ -\frac{u}{\rho} & \frac{1}{\rho} & 0 \\ \frac{\rho_p u^2 + \rho_p H - \rho h_p + 1}{\rho \rho_p h_T - \rho \rho_T h_p + \rho_T} & \frac{-\rho_p u}{\rho \rho_p h_T - \rho \rho_T h_p + \rho_T} & \frac{\rho_p}{\rho \rho_p h_T - \rho \rho_T h_p + \rho_T} \end{bmatrix} \tag{B.6}$$

Thus $\frac{\partial \mathbf{V}}{\partial \mathbf{U}} \frac{\partial \mathbf{E}}{\partial \mathbf{V}}$ in Eq. B.3 is obtained by multiplying $\frac{\partial \mathbf{V}}{\partial \mathbf{U}}$ by $\frac{\partial \mathbf{E}}{\partial \mathbf{V}}$:

$$\frac{\partial \mathbf{V}}{\partial \mathbf{U}} \frac{\partial \mathbf{E}}{\partial \mathbf{V}} = \begin{bmatrix} u & \frac{\rho^2 h_T}{\rho \rho_p h_T - \rho \rho_T h_p + \rho_T} & 0 \\ \frac{1}{\rho} & u & 0 \\ 0 & \frac{\rho - \rho^2 h_p}{\rho \rho_p h_T - \rho \rho_T h_p + \rho_T} & u \end{bmatrix} \tag{B.7}$$

Then the characteristic equation of the determinant (Eq. B.3) is:

$$(u-\lambda)\left[(u-\lambda)^2-\frac{\rho h_T}{\rho\rho_p h_T-\rho\rho_T h_p+\rho_T}\right]=0 \qquad \textbf{(B.8)}$$

Solving the equation, we get the roots:

$$\lambda_1=u_1,\ \lambda_{2,3}=u\pm\sqrt{\frac{\rho h_T}{\rho\rho_p h_T-\rho\rho_T h_p+\rho_T}} \qquad \textbf{(B.9)}$$

These roots are similar to the results, $(u,u\pm a)$, if the ideal gas equation of state is used. Thus, the sound speed for a generalized equation of state is obtained as:

$$a=\sqrt{\frac{\rho h_T}{\rho\rho_p h_T-\rho\rho_T h_p+\rho_T}} \qquad \textbf{(B.10)}$$

When the ideal gas equation of state is used, the sound speed reverts to $a=\sqrt{\gamma RT}$. If the flow is assumed isothermal, then the sound speed is simplified as:

$$\frac{1}{a^2}=\rho_p \qquad \textbf{(B.11)}$$

APPENDIX C: EIGENVALUES OF THE PRECONDITIONED SYSTEM

The one-dimensional Euler system described in Appendix B can be preconditioned as:

$$\mathbf{P}\frac{\partial \mathbf{V}}{\partial t}+\frac{\partial \mathbf{E}}{\partial x}=0 \tag{C.1}$$

where $\mathbf{P}$ is the preconditioned matrix given as:

$$P=\begin{bmatrix} \rho_p+\Theta & 0 & \rho_T \\ (\rho_p+\Theta)u & \rho & \rho_T u \\ (\rho_p+\Theta)H+\rho h_p-1 & \rho u & \rho_T H+\rho h_T \end{bmatrix} \tag{C.2}$$

$$\Theta=\frac{1}{V_{ref}^2}-\frac{1}{a^2} \tag{C.3}$$

The eigenvalues of the preconditioned system, i.e., $\mathbf{P}^{-1}\frac{\partial \mathbf{E}}{\partial \mathbf{V}}$, are obtained as follows using the same procedure described in Appendix B:

$$\lambda_1=u_1,\ \lambda_{2,3}=u'\pm a'=\frac{1+M_{ref}^2}{2}\left[u\pm a\frac{\sqrt{\left(1-M_{ref}^2\right)^2M^2+4M_{ref}^2}}{1+M_{ref}^2}\right] \tag{C.4}$$

where

$$M_{ref} = \frac{V_{ref}}{a}, \; M = \frac{u}{a} \tag{C.5}$$

are the reference Mach number and the Mach number respectively.